Studies of the anisotropic growth of ZnO synthesized by an organometallic method and kinetic study of the concomitant gelation

Yinping Wang

Yinping Wang. Studies of the anisotropic growth of ZnO synthesized by an organometallic method and kinetic study of the concomitant gelation. Material chemistry. Université Paul Sabatier - Toulouse III, 2022. English. NNT : 2022TOU30101 . tel-03813573

THÈSE

En vue de l'obtention du

DOCTORAT DE L'UNIVERSITÉ DE TOULOUSE

Délivré par l'Université Toulouse 3 - Paul Sabatier

Présentée et soutenue par

Yinping WANG

Le 27 juin 2022

Etudes de la croissance anisotrope de ZnO synthétisés par une méthode organométallique et étude cinétique de la gélification concomitante.

Ecole doctorale : **SDM - SCIENCES DE LA MATIERE - Toulouse**

Spécialité : **Sciences et Génie des Matériaux**

Unité de recherche :
LCC - Laboratoire de Chimie de Coordination

Thèse dirigée par
Myrtil KAHN et Christophe MINGOTAUD

Jury
Mme Fabienne GAUFFRE, Rapporteure
M. Jean-Cyrille HIERSO, Rapporteur
Mme Myrtil KAHN, Directrice de thèse
M. Fabien DELPECH, Président

Acknowledgements

Time flies. The scene of entering the laboratory on the first day seems to have happened yesterday. In the blink of an eye, my doctoral study life is coming to an end.

First and foremost, I’d like to sincerely and deeply appreciate my supervisors Dr. Myrtil Kahn and Dr. Christophe Mingotaud offer me this opportunity to study on such a great platform in France. Thank them give me this chance to broaden the width of my life. Thank them for their patient guidance. Their profound theoretical foundation, rich practical experience, and rigorous and academic attitude have benefited me a lot. Thank them for their encouragement as I always remember their saying “we will succeed”.

I would also like to thank Dr. Pierre Fau who helped me a lot in the daily lab life, especially in my work of sensors’ part where I have zero experience before. And his responsible and careful attitude towards the safety of equipment guarantees the smooth progress of my experiments.

Dr. Yannick Coppel, an excellent expertise in NMR technology, also helped me a lot. I learned a lot from him about how to characterize surface species interacting with surface of nanoparticles and the tracking method of a kinetic study. Thanks very much. I also want to thank Dr. Juliette Fitremann in the measurement of rheological and mechanical properties; Dr. Christine Lepetit in the calculation parts; Vincent Collière in the electronic microscopy characterization; Dr. Jean-Daniel Marty and Dr. Clément Roux in data process part; and all the others who indeed help me finish my PhD work.

All current and former Equipe T members in LCC and Equipe IDeAS members in IMRCP, Kevin CASTELLO LUX, Fang Yin, Qilin Zou, Adele GIRARDEAU, Dimitri ROUBERT, Maxime Puyo, Guillaume Garnide, Ekaterina BELLAN, Zhihua Zhao, Hala Assi, Ségolene Palussière, and Dr. Katia Fajerwerg for their fruitful discussions and friendship.

Thank my friends in Toulouse who have helped me a lot in my life of France. Thank all the LCC and IMRCP employees for their kind-hearted help.

Thank China Scholarship Council (CSC) and CNRS for financial support during my study in France.

Thank my family who are always on my side without asking for anything in return during these PhD years. Their understanding and support are the source of motivation for my hard work. May you be healthy and happy.

May everyone have a peaceful heart, and may tomorrow be better.

In the end, I sincerely thank all the experts and juries who took the time to review this thesis during their busy schedule.

Catalogue

Chapter I. Literature view and project objectives

In this chapter, focusing on the synthesis method and application value, we firstly start by briefly introducing the scientific research value of nanoscience, then the outstanding advantages of metal oxide semiconductor nanomaterials and finally highlighting the properties of ZnO. At the same time, we present a few synthesis methods of nanomaterials and then focus on the characteristic synthesis method that our group uses, i.e., the organometallic method. This method has been used throughout the work of this thesis. In the end, we presented the previous works related to ZnO in our group, which derive and then determine the objective of this thesis.

1.1 Introduction

In the past decades, the scientific field related to nanoscience has been the focus of many researches and studies. This can be easily demonstrated via a literature retrieve on scientific database such as “Web of Science”. Keywords such as “Nanoparticle” are related to more than 173000 publications in the timespan of 1991-2020 (See the bar chart below, analysis made on 06/09/2021). The interest in this field started in the 90’s, burst in the beginning of the 21st century and continues to expand with an annual rate of ca. 17000 papers associated to the subject. This reflects the development and breakthroughs of nanoscience which is still a research hotspot and is attracting researchers’ eyes.

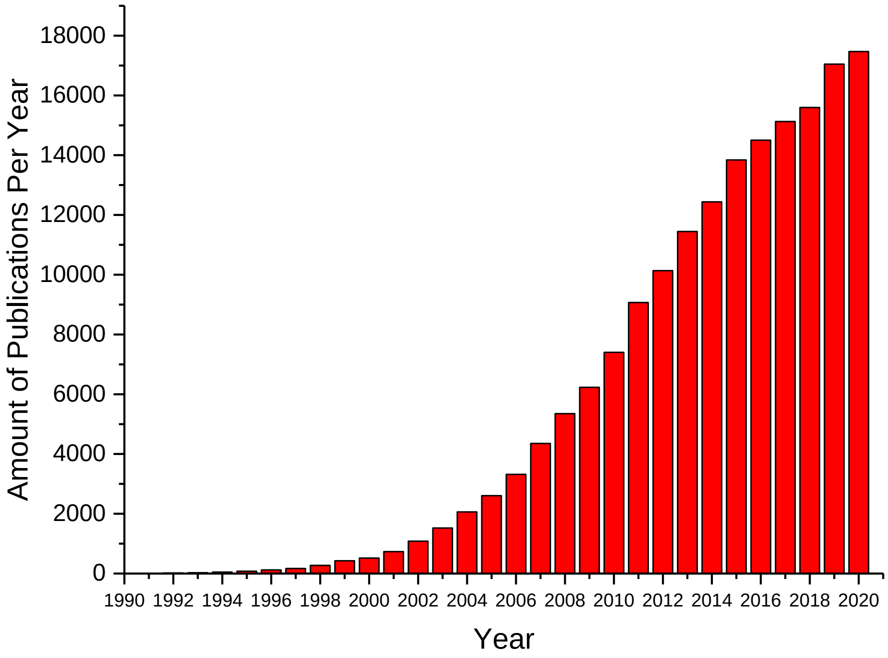

Nowadays, nanoscience is defined as the study of devices, structures or molecular architectures which have at least one characteristic dimension on the scales of nanometers, i.e. ranging between 1 and 100 nm.[1] Many examples can be found in the literature, from nanomedicine, nano catalyst to nanodevice. These nanomaterials acting as a bridge between bulk materials and atomic structures can display huge changes in physical, chemical, and biological properties as they reduce in size and shape. Two main reasons explain why properties of nanomaterials behave differently compared to bulk:[2]

Surface effects: Let's consider a spherical (nano) particle. The surface-to-volume ratio is inversely proportional to the particle size. Therefore, the smaller the particle the larger the fraction of atoms at the surface, and the higher the average binding energy per atom. These naked and coordinately unsaturated atoms signify defects on the surface of the particle. These defect-rich surfaces are highly active and easy to adsorb other atoms or react with other atoms, which finally result in their special physical and chemical properties.

Confinement effect or quantum confinement: Many properties of materials are related to the localization of the electrons within the materials. They can be strongly localized in the large majority of molecules or strongly delocalized in metallic structures. Changing the size of a material will strongly influence such electron delocalization and therefore, the associated properties, like optical, magnetic, and electrical, etc.

Besides nanodevices, nanoscience has been the focus of many studies on nanomaterials having various chemical composition, geometry and size.

Generally, based on the types of material constituent, they can be classified into two categories: carbon- or organic and inorganic based.

Organic-based or carbon-based nanomaterials: They are mainly fullerenes, carbon nanotubes (CNTs) and graphene, but also dendrimers, liposomes, and polymer nanoparticles.[3]-[8] They are mostly made from organic material (e.g. surfactant[9]).

Inorganic-based nanomaterials: They are based on chemical elements different from carbon. This can be for example simple salts such as carbonate,[10] phosphate,[11] etc. Among all these materials, the ones related to metal elements are of particular interest. This is the case of pure Cu, Pd and Au nanoparticles,[12]-[14] but also metal oxide-based nanoparticles like TiO_2, SiO_2, ZnO, V_2O_3,etc.[15]-[19]

Associations between those two types of materials (mentioned above) will lead to multiphase nanostructures (often called hybrid nanomaterials) with one phase (at least) being at the nanoscale dimension. They can be any combination of metal-based, carbon-based, or organic-based nanostructures with any form of ceramic, metal, or polymer bulk materials.[20]-[22] Among all the inorganic nanomaterial, metal oxide semiconductors are highly studied.

1.2 Metal Oxide Semiconductor Nanoparticles

1.2.1 General Introduction of Metal Oxide Semiconductor Nanoparticles

Firstly, many of metal oxides not only have features of forming readily and with high chemical stability but also can display a broad variety of structures and in addition show multiple stable oxidation states of the metal ions.[23]-[25] Secondly, among these oxides, metal oxides with property of semiconductivity are valence compounds with a high degree of ionic bonding. Thirdly, nanosize is closely correlated to the physicochemical properties as we presented in **1.1**. Therefore, nanomaterial of metal oxide semiconductor can represent a class of unique materials due to their electronic charge transport properties, especially when compared to conventional covalent semiconductors such as silicon (Si). This allows them possess unique functionalities and have wide applications in electronics,[26] optics,[27] energy storage[28] and catalysis.[29]

Metal oxide semiconductor nanomaterials can be divided into n-type metal oxide semiconductors and p-type metal oxide semiconductors (n stands for the negative charge on an electron, while p stands for the positive charge).The p-type is one kind of materials in which the adding of a controlled amount of an acceptor impurity to intrinsic semiconductor leads to the result that holes are the majority carriers and electrons are the minority carriers. Whereas, for n-type, the case is the opposite. The adding of a controlled amount of a donor impurity to intrinsic semiconductor leads to the fact that electrons are the majority carriers and the holes are the minority carriers.[30]

In the solid state of oxide semiconductors, the band where valence electrons are confined into a band of energy levels is called valence band. The band occupied by electrons that have acquired enough additional energy to leave the valence shell and become free is called conduction band. The difference in energy between the valence band and the conduction band is called band gap, which equals the amount of energy a valence electron must need to jump from the valence band to the conduction band. Normally, material with around 2.0 to 4.0 eV bandgaps are wide-bandgap semiconductors, with around 1.5 to 2.0 eV bandgaps are narrow-bandgap semiconductors, while with large bandgaps (> 4 eV) are insulators and with about zero eV are metals (see the band model below).[31]-[34] The commonly researched n-type of wide-bandgap oxide semiconductors, for instance, are WO_3 (band gap ca. 3.0 eV),[35]-[37] SnO_2 (band gap ca. 3.5 eV),[38] [39] Fe_2O_3 (band gap ca. 2.1 eV),[40] [41] ZnO (band gap ca. 3.4 eV), [39] [42] etc. For p-type, such as Co_3O_4 (band gap ca. 2.0 eV),[43] [44] NiO (band gap ca. 4.3 eV), [45] [46] CuO (band gap ca. 2.2 eV),[47] [48] are of interest to researchers as well.

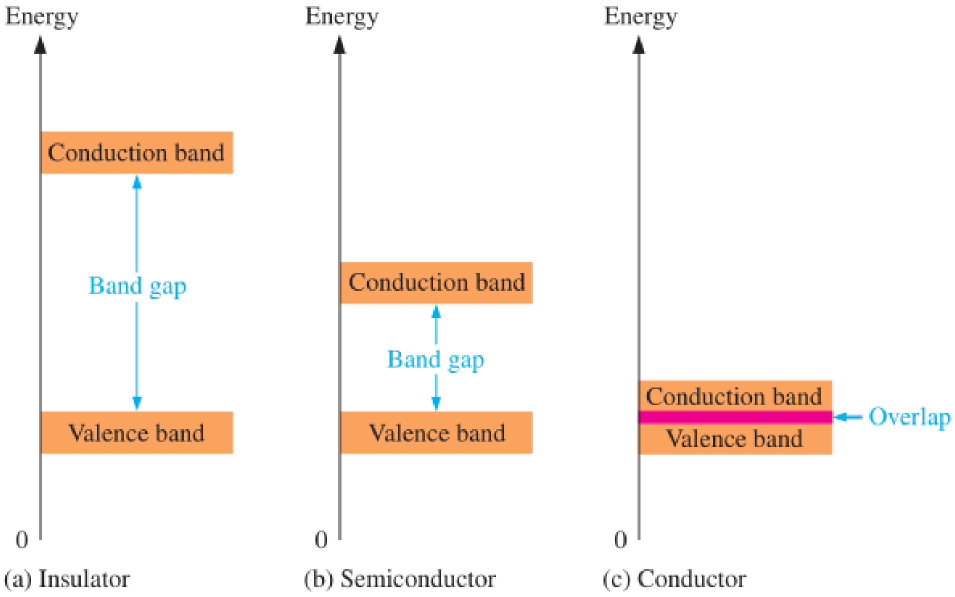

For some of oxide semiconductors, their chemical ratios tend to show a lack of oxygen.[49] [50] These oxygen vacancies can play a role of the electron donor, giving rise to n-type semiconductors. The treatment of vacuum heating can further strengthen the degree of oxygen vacancies, which enhances its electronic conductivity.[49] ZnO is one such kind of oxide semiconductors. It is a wide band gap (ca. 3.4eV) semiconductor having a high electron–hole binding energy (60 meV), high electron mobility, and luminescent in visible and near ultraviolet range.[51]-[54] It has the advantages of biocompatibility, chemical stability, environmental friendliness, low synthesis cost, etc. Its electronic features (large band gaps, crystal defects and high exciton binding energy) make it a good candidate to satisfy the needs of using ultraviolet (UV)/blue light emitting properties to design solid state light sources and detectors.[55]-[56] In some published work, the optical properties of ZnO depend strongly on the preparation conditions,[57]-[59] such as it can show emissions band in ultraviolet, violet, and green regions, yellow and red regions.[60] [61]

1.2.2 General properties of ZnO

Structure properties of ZnO:

Under usual condition, ZnO mainly has two forms of crystalline structures: hexagonal wurtzite and zinc blende. Among them, hexagonal wurtzite is the most abundant and has the highest thermodynamic stability. While zinc blende form is stabilized, for example, by growing ZnO on substrates with cubic lattice structure.[62] In the nanomaterial field, work related to blende type is less than that of wurtzite type. This is not only because at the nanoscale, only wurtzite type exists, and at higher temperature the blende type turns bulk blende ZnO,[63] but also due to a lack of suitable substrates for the zinc blende ZnO epitaxy.[62]

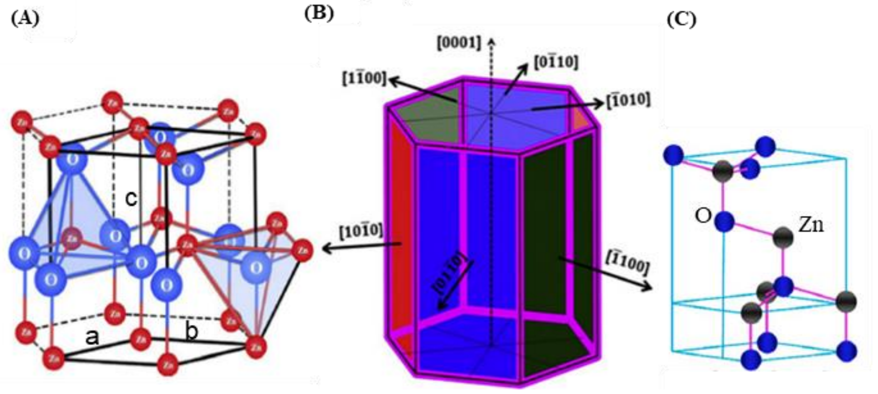

Figure 1. (A) Hexagonal wurtzite crystal structure of ZnO,[64] (B) Hexagonal prism of ZnO crystal showing different crystallographic faces,[64] (C) cubic zinc blende crystal structure of ZnO.[62]

At ambient conditions, hexagonal wurtzite consists of packing of –Zn-O-Zn-O- layers along the c axis with a = 3.25 Å and c = 5.12 Å (see Fig 1A). The hexagonal structure is of space group P_{63mc} and has no inversion symmetry. Each anion is surrounded by four cations at the corners of a tetrahedron, and vice versa. Zinc or oxygen atoms on planes of $(10\bar{1}0)$ and $(11\bar{2}0)$ are stoichiometrically equal (see Fig 1B). Therefore, planes of $(10\bar{1}0)$ and $(11\bar{2}0)$ are regard as nonpolar plans. Whereas the basal planes, (0001) and (000$\bar{1}$), the pyramidal planes (10$\bar{1}$1), are comprised of sheets of zinc or oxygen and consequently are strongly polar.[65] The polar planes (0001) and (000$\bar{1}$) are usually appointed as zinc-terminated surface and oxygen-terminated surface, respectively. These polar planes possess high surface energy.

While in zinc blend structure, the atomic arrangement is quite similar to that of the wurtzite structure—only the angle of adjacent tetrahedral units is different, having values of 60° for zinc blende and 0° for wurtzite structure (see Fig. 1, C). The symmetry is given by space group F$_{4\bar{3}\mathrm{m}}$.[62]

Optical properties

Due to the fact that high exciton binding energy of ZnO is 2.4 times higher than value of KT (ca. 25 meV), ZnO can show behaviors of exciton transitions and luminescence at room temperature. The characteristics of having many intrinsic defects, either interstitial atoms or atomic vacancies,[66] and the tunability of binding energy make ZnO have more accessibilities to high radiative recombination efficiency for various spontaneous emission and a lower threshold voltage for various laser emission.[67] However, importantly, related to its photoluminescent (PL) properties, some factors like temperature, the perfection of the particles size, morphology, crystal structure and in particular of its content of defects play important roles:

Yi's work reported that at low temperature, such as at 10k, ZnO nanorods can show not only free excitonic emissions but also defect-mediated excitonic emissions.[68] The former is attributed to defect free ZnO while the latter is ascribed to neutral donor bound exciton.[68] In Zeng's work[60], with increasing temperature from 10 K to 300 K, the PL properties of prepared ZnO nanoneedle arrays which exists in three emission bands in ultraviolet, violet, and green regions show different temperature dependences: A normal red shift for the ultraviolet emission, S-shaped shift for the violet emission, and blue shift for the green one (see Figure 2). It's said their temperature dependent shifts are related to the zinc interstitial and oxygen vacancy levels and carrier localization effect at the defect levels in addition to band-gap shrinkage.

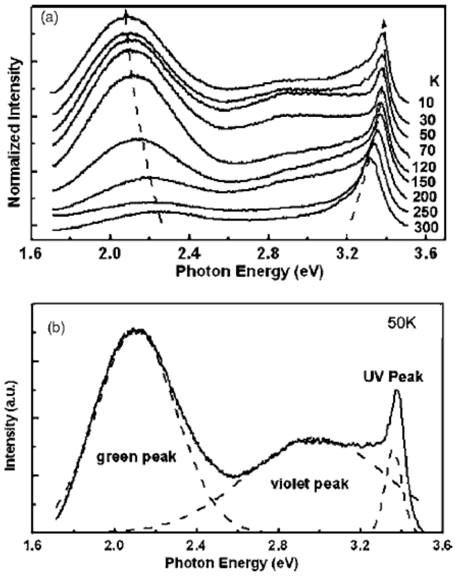

Figure 2. Photoluminescence (PL) spectra of the as-prepared sample. (a) PL spectra

at different temperatures (all spectra are normalized by the UV peak intensity and shifted in the vertical direction for clarity). (b) Typical Gaussian-fitting analysis of the PL spectrum at 50 K (correlation coefficients: 0.99).[60]

Of course, ZnO nano particle also embody size quantization. It' said that as the particle sizes are reduced to dimensions (<5 nm) comparable with an exciton diameter, the energy gap between the valence and the conduction band increases.[69] As a consequence, the optical absorption shows a blue shift when size decreases.[70] Besides, Brus's work reported that smaller particles have bigger intensities for the UV peak.[71] This may be related to concentration of surface defects.

The ZnO optical properties are also connected with morphologies of ZnO nanostructures. For example, Awasthi's work show that for three different morphologies of nanoparticles (NP), nanosheets (NS) and nanorods (NR), their corresponding optical band gap is 3.26, 3.24 and 3.10 eV, respectively.[72] In the UV region, NP shows maximum luminescence intensity. While, in the visible region, NS shows maximum luminescence intensity. Here, notice that the band gap of the three kinds of morphologies is relatively smaller than 3.37 ev. Thus, it's worth recall that the changes in the optical band gaps with respect to the ZnO nanostructure morphology suggest that nanostructure crystallinity, crystal growth facets, and crystal grain size lead to the effective band gap of nanostructured ZnO smaller than its bulk value of ca. 3.4 eV.[57]

In addition, the doping process with various transition metals thanks to its crystalline structure can also tune its band gap and finally influence its optical properties.[73]-[77] Therefore, synthesis of well-controlled ZnO nanoparticles with appropriate methods is very important in the study of optical properties of ZnO.

1.3 Synthesis methods of nanomaterials

Two main strategies to control over the size and morphology of nanomaterials are used for the synthesis of nanomaterials and the fabrication of nanostructures: top-down approach and bottom-up approach (see Figure 3).[78] Top-down approach generally refers to the mechanical synthesis way. Its general principle is processing solid bulky material to get nanosize material. Bottom-up approach involves the coalescence or assembling of atoms and molecules to generate diverse range of nanoparticles. Though the fact that top-down approach allows to have large scale production and no need chemical purification, it produce nanomaterial with broad size distribution (10-1000 nm), varied particle shapes or geometry. And the control over deposition parameters is difficult to achieve. Besides, the relevant instruments and techniques are expensive. Therefore, researchers are much more interested in using bottom-up approach to synthesize nanomaterials, including physical processing and chemical processing. Whatever the method may be, one important point related to various morphologies during the synthesis process is the "nucleation, growth, and aging" steps.[79]

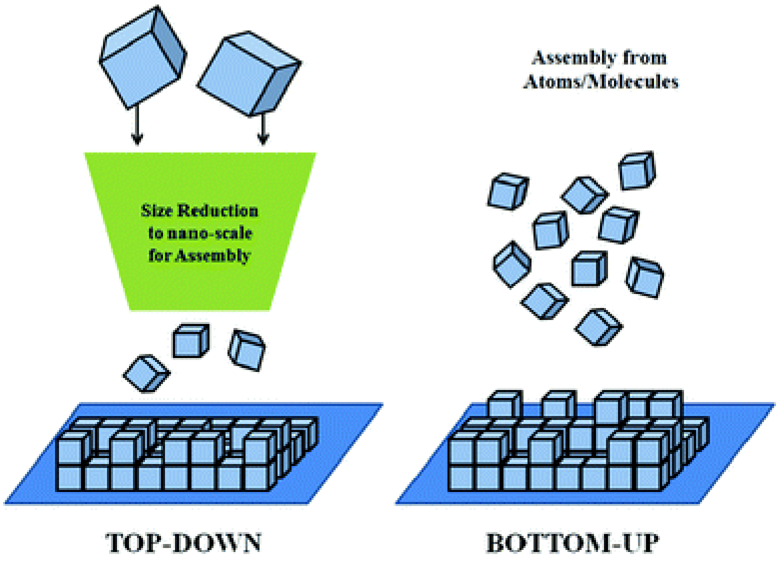

Figure 3. Bottom-up and top-down synthesis methods.[78]

Here, under strategy of bottom-up approach, we mainly introduce a few interesting methods: chemical vapor deposition (CVD), sol-gel method, precipitation method and organometallic method.

1. Chemical vapor deposition (CVD)

CVD is a process using the deposition of solid films or producing powders or composite materials from vapor phase via chemical reactions occurring at very high temperature condition.[80] The main characteristic of CVD method is the synthesis of nano-objects with a low dimensionality, such as ultrafine particles, nanowires, nanotube and thin films.[81]-[83] For example, Polarz et al. synthesized size selected ZnO NPs (6–30 nm) by using the tetrameric alkyl-alkoxy zinc compound $[CH_3ZnOCH(CH_3)_2]_4$ as the precursor, which was chemically transformed into ZnO through gas-phase reactions.[83] There are also a variety of enhanced CVD processes, which involve the use of plasmas,[84] lasers,[85] or combustion reactions[86] to increase deposition rates and/or lower deposition temperatures.

CVD method own some advantages in aspect of depositing thin films: 1. CVD films are generally quite conformal, i.e., that the film thickness on the sidewalls of features is comparable to the thickness on the top. 2. Materials can be obtained with relatively high deposition rates and high purity. However, the disadvantage is the safety issues of the materials used for the deposition, such as the use of some precursors and some by-products are toxic, pyrophoric, or corrosive.

2. Sol-gel method

The sol-gel method[87] is one of the most common chemical solution methods. Generally speaking, the procedures are using organometallic alkoxides or inorganic salt as raw materials, through processes such as hydrolysis, condensation, and drying, and finally obtaining nanomaterials by appropriate heat treatment.

In fact, the “sol” refers to a colloidal suspension of solid particles in a liquid and ‘gel’ are polymers containing liquid. Hydrolysis and condensation chemical reactions are two typical steps of the sol–gel process. Firstly, the former normally uses water to break the bonds of the precursor which is also the first step in the formation of the gel phase. After that via the following condensation process, a stable transparent sol system in solution is formed. Then the sol slowly polymerizes between the aged colloidal particles to form a gel with a three-dimensional network structure. Finally, the gel is dried, sintered and solidified to prepare nano-substructure materials. For instance, ZnO NPs can be synthesized with this method using zinc acetate as the precursor and triethanolamine (TEA) or polymers like polyvinylpyrrolidone (PVP) or derivatives of polyethylene glycol (PEG) as surfactants.[88]-[90] By varying experimental parameters, such as capping ligands, calcination temperature, sol drying method for the fabrication of ZnO NPs, one can get ZnO nanostructure with different morphology and size, examples like rods, spherical particles, cylinder, nanotubes, etc.[91]-[94]

This method has many advantages: 1. It is easy to uniformly and quantitatively incorporate some trace elements, to realize homogenous doping at the molecular level due to the solution reaction step. 2. It only requires mild conditions: low gel heat treatment temperature, good sintering performance, high powder purity, fine particles, easy control of the reaction process, simple equipments, and convenience manipulation. However, there are also disadvantages such as large drying shrinkage, high price of metal alkoxides, damage to health by organic matter, and difficulty in industrial production.

3. Controlled precipitation method

This method consist in by adding a suitable precipitant to a salt solution containing metal ions to promote sufficient precipitation and crystallization, and a heat treatment to remove the organic part or the chemical bonded water to form the ultimate product. During the precipitation process, when the solution reaches a critical supersaturation of the species forming particles, it bursts to form the nuclei. Its kinetics of nucleation and particle growth in homogeneous solutions can be adjusted by the controlled release of anions and cations through adding organic molecules or controlling parameters such as pH, temperature and time of precipitation.[95]-[105]

For instance, in the work of Krysztafkiewicz *et al.*[96] ZnO was synthesized by precipitation from water solutions of KOH and $Zn(CH_3COO)_2$. It was found the particle size and its morphology are related to the excessive reactants, the dosing rate of KOH into $Zn(CH_3COO)_2$ solution and the prepared temperature. The excess of one of the reactants significantly influence its size. When 20% excess of zinc acetate solution was used, the smallest particles close to 50 nm in diameter can be obtained. The dosing rate can also influence its dispersibility. When the rate of dosing of KOH to $Zn(CH_3COOH)_2$ is 11 cm^3/min, the spherical particles with little tendency to agglomerate were formed. While, at the higher or lower rates of dosing show a considerable tendency to agglomerate (see Figure 4). In addition, diameter of micrometric ZnO particles obtained at different temperatures is positively correlated with temperature: increasing the temperature of precipitation increases the diameters of the ZnO particles.

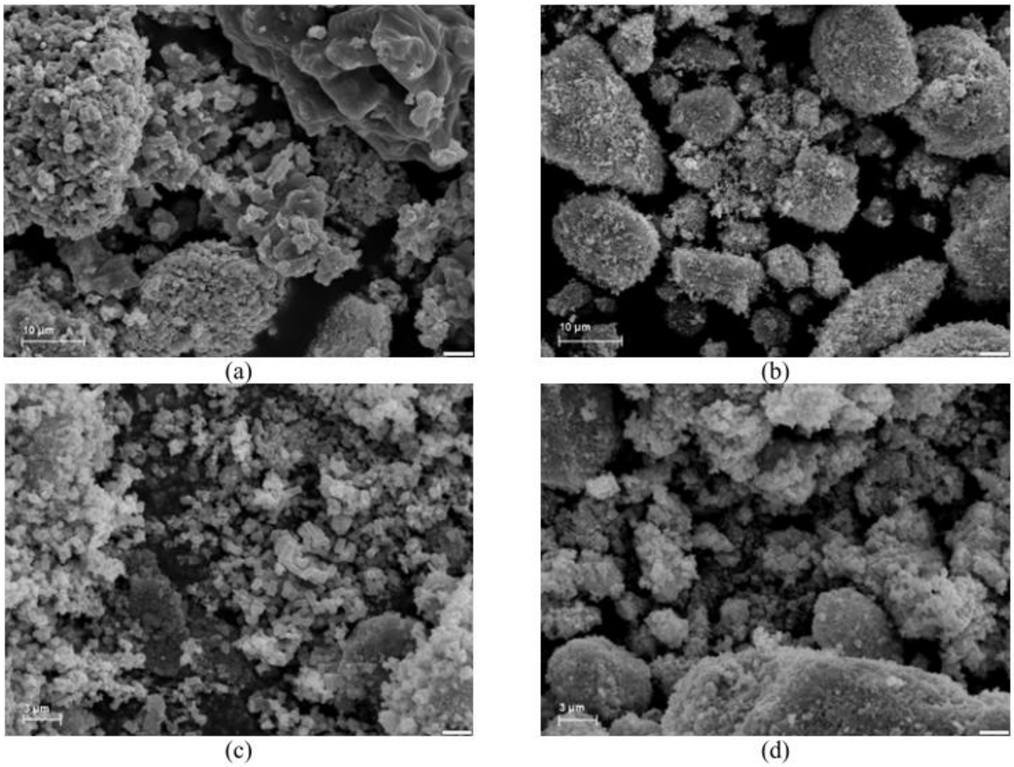

(a) (b)

(c) (d)

Figure 4. SEM images of ZnO samples precipitated at different rates of dosing of KOH solution to $Zn(CH_3COO)_2$ solution of (a) 1.1 cm^3/min, (b) 3.0 cm^3/min, (c) 11 cm^3/min, (d) 15 cm^3/min, at 20 ^oC, at the stoichiometric ratio of the reagents.

Controlled precipitation method has some advantages: facile manipulation, less expensive of raw materials of precursors, access to acquire nanomaterials of different size and morphology via changes of preparation conditions. However, the disadvantage is heat treatment.

4. Organometallic method

Organometallic procedures are based on the use of precursors, in which metal-carbon bonding is presented. During the preparation process, firstly, the metal precursor may react with the surfactant that can be also a ligand, forming complexes. Secondly, in a controllable way, the introduced oxidative agent (O_2, H_2O; etc.) decomposes the previous formed complexes, and form crystalline “nuclei” of nanoparticles at relative low temperature (typically at room temperature). Thirdly, these “nuclei” will evolve into mature particles under the influence of the surfactant / ligand via certain interacting forces (for example, electrostatic, hydrogen, or van der waals forces). Finally, after the aging process, the generated nanoparticles could be quantitatively obtained.

The whole process is a highly exothermic reaction process and undergoing under mild conditions (pressure and temperature). Compared with the sol-gel method, due to the metal precursor’s richness in the number of metal source with low prices, plus some metal ions can’t be hydrolyzed and polymerized under sol-gel reaction condition, organometallic method has much more advantages. However, the general drawback of the organometallic procedures is that the precursors are sensitive to air, and they yield hydrophobic NCs coated with a layer of alkyl ligands.

Our group has gained rich knowledge in the synthesis of metal and metal oxide nanoparticles with organometallic method. Some metallic nanoparticles are obtained by reduction of organometallic precursors in an organic solvent and in the presence of stabilizers. For example, metallic particles like Fe,[106] Co,[107] Pd[108] or metal alloys such as Fe-Co[109] have been successfully synthesized. These particles are normally stabilized by polymers or organic ligands like fatty amines or fatty carboxylic acids.

Metal oxide NPs such as SnO_2,[110] In_2O_3[111] and Co_2O_3[112] were obtained by controlled oxidation of the pristine metal precursors. Herein, one efficient strategy to obtain ZnO nanoparticles is based on the controlled hydrolysis of the organometallic precursor bis(cyclohexyl) zinc [$Zn(Cy)_2$] in the presence or absence of solvent.[113]-[115] Much more related group work is presented in the following paragraphs.

1.4 Group work in LCC

1.4.1 Synthesis of ZnO nanoparticles,

In 2003, our group published the first work using organometallic method to synthesize ZnO nanoparticles.[113] Since then, 100 more research work based on organometallic method have been published successively.

Our developed efficient ZnO synthetic route with organometallic method is briefly described in scheme 1.

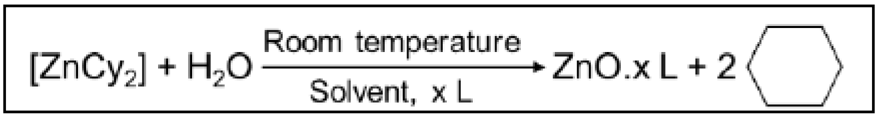

Scheme 1. Synthesis method of ZnO nanoparticles

Firstly, the zinc precursor used in my thesis work is [$Zn(Cy)_2$] compounds. They are very sensitive to water and air. Consequently, exothermic decomposition reaction and generating ZnO nanoparticles will happen when the complexes are exposed to air. Therefore, for reactions carried out in solvent, the organic solvents should be water-free and not be protic solvents. Secondly, in the hydrolysis process, the hydrolysis rate is related to the addition of oxidative agent. By adjusting the adding rate of the oxidative agent, it is possible to adjust the released local heat, which allows to control growth rate of the crystal seeds and decide its final morphology. Thirdly, the fatty amine, fatty acid or surfactant are served as the stabilizer to prevent metal oxide particles from aggregating, influence the seeds growth direction, and form a homogeneous colloid solution. For the stabilizers, the most commonly used fatty amines are hexadecylamine (HDA), dodecylamine (DDA), octylamine (OA), heptylamine (HPA), hexylamine (HA), pentylamine(PA), butylamine(BA), etc. And the most commonly used fatty acids are dodecanoic acid (DDAc), oleic acid (OlAc), etc. As for the stabilizers, their specific roles played will be introduced in the next section.

By carefully optimizing reaction parameters, such as types of stabilizers, reaction ratio, reaction time, concentration, etc., it can be possible to control or even adjust such as hydrolysis objects, hydrolysis rate and crystal seeds growth direction, thereby realizing the target of obtaining the expected ZnO nanomaterials.

The state-of-the-art of our strategy can be reflected from these four aspects: 1)

With the sufficient released heat to drive hydrolysis process, the preparations are conducted at room temperature and normal atmospheric pressure. 2) The obtained ZnO nano-objects can be dissolved in the common organic solvent.[114] Thus, the colloid solution can easily be deposited on various surfaces as monolayers or thick layers, and may thus be applied as photoluminescent probes or paints. 3) Due to the released heat in the hydrolysis process, the produced volatile products, like cyclohexane, methane and ethane, are evaporated during the synthesis and no side products are retained. 4) The metal precursor could be the single component metal precursor or different multi-component metal precursors. Thanks to this feature, it allows us have accesses to obtain multi-component metal hybrid materials.

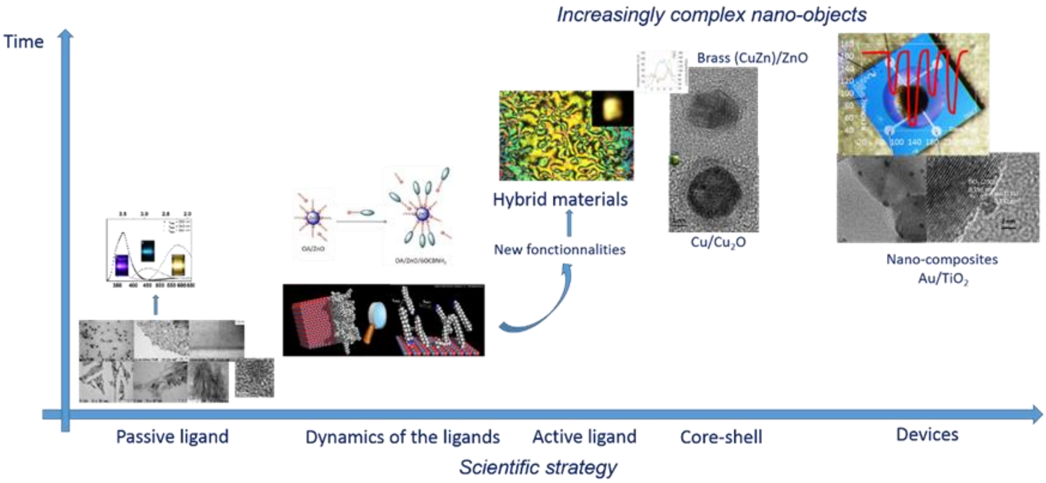

Figure 5. Schematic illustration for the research strategy in the LCC's group.

Last but not least, concerning the general research activity in our team, it is mainly centered on the design and elaboration of nano-objects and hybrid nanomaterials: from the synthesis of the metal-organic precursor to the devices (see Figure 5). As presented in **1.2**, the final properties of optical, sensing, catalysis for the nanomaterials are strongly related to the morphology, size and shape, once again optimizing the synthesis condition with various parameters is of great importance.

1.4.2 The role of stabilizing ligands on the prepared NPs

The ligands used in the synthesis are normally for limiting crystal growth, preventing aggregation, and in some cases passivating the surface of the material.[117]

First, the roles of ligands in aspects of solubility, morphology of ZnO.

We know that the obtained ZnO nano-objects can be dissolved in the common organic solvents. However, in our earlier group synthesis work, when [$Zn(Cy)_2$] and octylamine was used as Zn precursor and stabilizer, respectively, the addition of the family of glycolic acid ethoxylate ethers surfactant helps the NCs get water soluble.[118] This is because the formed organic layer comprising the pristine ligand (octylamine) and the glycolic acid based surfactants stabilize the ZnO NCs. There exists a subtle interplay of interactions between the added surfactant, the ligand and the surface of the ZnO nanocrystals. This work shows that ligands can change ZnO solubility from organic phase to water phase.

In other earlier work, when primary amines are used as the ligands to react with Zn precursor under various conditions, it was found the critical role of different parameters (composition of the pristine reaction mixture, amount of water, kinetics parameters of the reaction, temperature…) can be used to achieve a good control over the final morphology.[114] [119]] Specially, in the organic solvent reaction medium at a relatively low overall concentration or better controlled mixing time in absence of solvent medium or higher reaction temperature, normally isotropic particles were obtained.[114] While, in absence of any solvent or relatively high overall concentration or shorter mixing time or lower reaction temperature, normally anisotropic nanoparticles were obtained.[119] The representative TEM images are shown below in Figure 6.

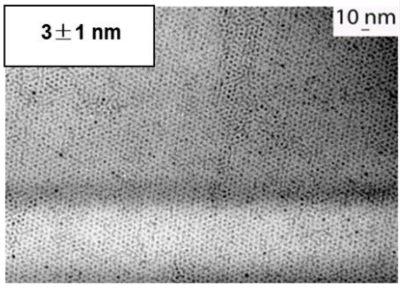

ZnO NPs@HDA/OlAc in THF[3]

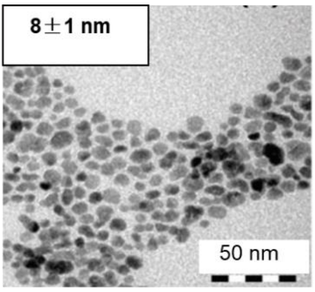

ZnO NPs@DDA in THF[4]

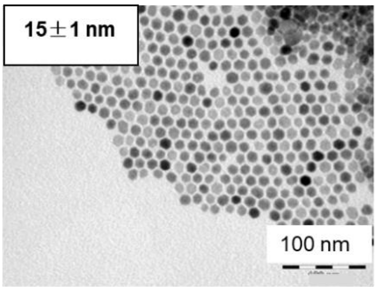

ZnO NPs@DDA/0.5OlAc in THF[5]

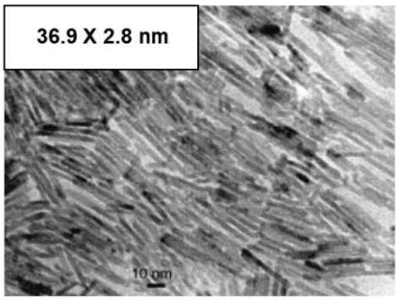

ZnO NRs@2OA in air[6]

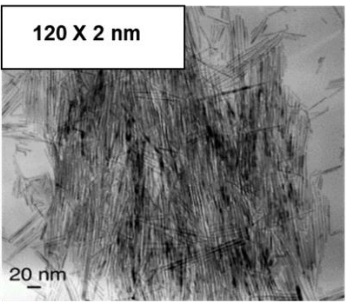

ZnO NRs@OA in air (after 24h of oxidation)[7]

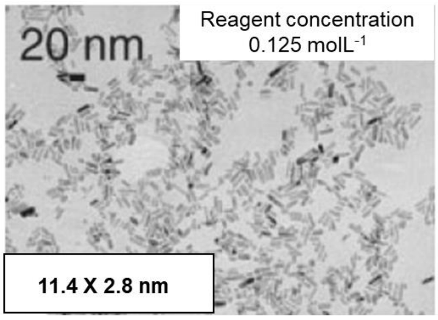

ZnO NRs@HDA in THF[7]

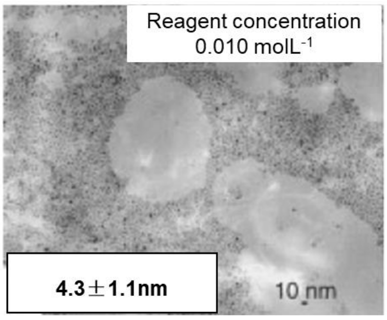

ZnO NPs@HDA in THF[7]

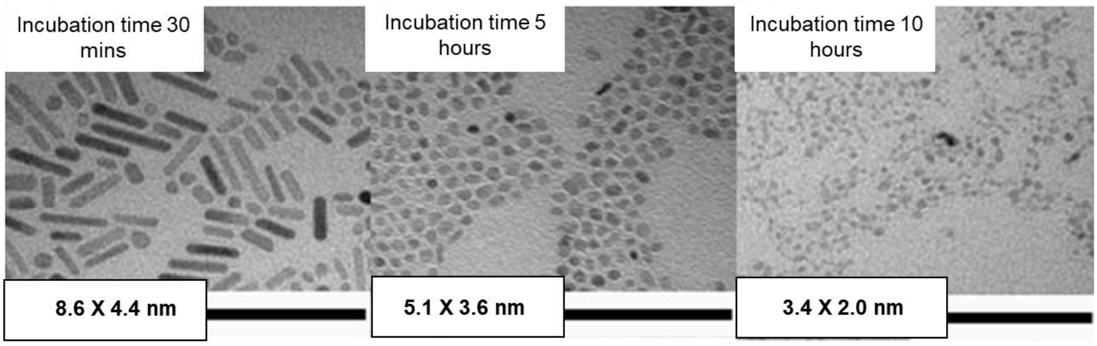

ZnO NRs@DDA in air[8] ZnO NPs@DDA in air[8] ZnO NPs@DDA in air[8]

Figure 6. ZnO isotropic or anisotropic particles are obtained through reactions of Zn precursor and primary amines under various conditions.[119]

It’s worth noting that the mixing time is very important to control the morphology of ZnO when the primary amine was used as ligand (see TEM images at the bottom in Figure 6). The reason why under shorter mixing time it formed nanorods is because it goes with an oriented attachment growth. The earlier formed single crystal nano particles with inconsistent orientations go through orientation rotation, making their crystal lattice orientation consistent, and then these small nano crystals grow into a large nano crystal through oriented attachment, that is to say, the initial formed isotropic nanoparticles are consumed to proceed the growth of the former nucleated particles to form rods finally. However, the reason why under longer mixing time it formed NPs is because when the viscosity of the mixture increases, the water diffusion speed and orientation rotation of the earlier formed single crystal nano particles are limited. As a result, growth process with oriented attachment is limited, leading to the obtaining of shorter NPs.[119]

Second, the roles of ligands in aspects of interaction with ZnO surface.

In the point above, the undeniable fact that the stabilizing ligands and synthesis conditions play important roles in controlling the final state and morphology of ZnO is presented. However, it can’t be stressed enough to understand the interaction forces between stabilizers and ZnO surface during the development synthesis strategy of ZnO nanomaterial. Here, in the second point, we focus on introducing the surface state and surface interactions of ZnO when only primary amine or binary stabilizers were used in the synthesis system.

In our previous work,[121] it was found that there exists a dynamic behavior between the ligands and ZnO particles in solution. In the system of ZnO colloidal solutions where long alkyl chain stabilized ZnO nanoparticles, there are three different modes of interaction of the amines at the surface of the NPs. The first mode corresponded to a strong interaction between a small amount of amine and the ZnO. The second mode corresponded to a weak interaction between the amines and the surface of the ZnO NPs. The third, which is the weakest, mode of interaction, corresponded to the formation of a second ligand shell by the amine around the NPs that was held together through van der waals interactions. The second and third modes were in fast exchange on the NMR timescales with the free amines. The strongly interacting amines at the NPs surface (first mode) were in slow exchange with the other modes. Figure 7 shows except these interactions, there exists also complex hydrogen-bonding network at the NPs surface, which not only involve the coordinated amine but also THF and water molecules that remained from the synthesis.[121] The three modes are in thermodynamic equilibrium with the free amines and the relative populations varied with their concentration.

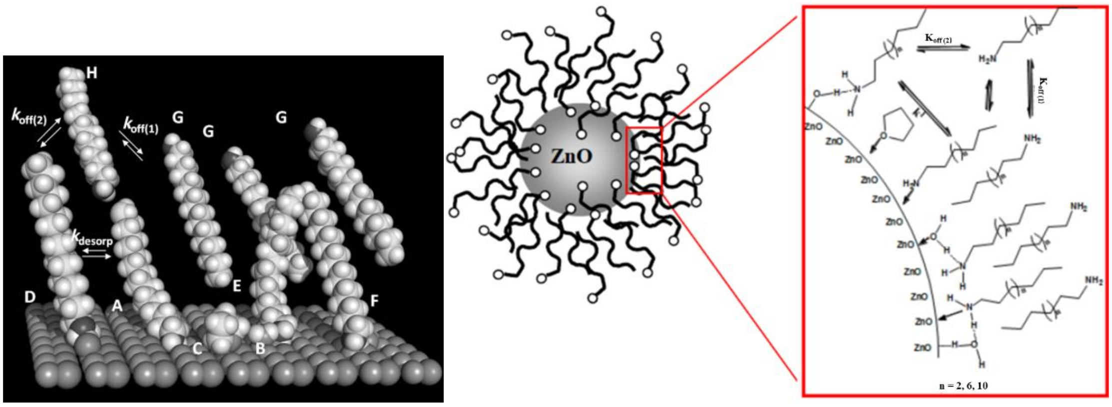

Figure 7. Illustration of the various interactions at the surfaces of the ZnO NPs. Amine (A), H_2O (B), and THF (C) molecules coordinate to Zn^{2+} ions; amine groups hydrogen bond to a hydroxy group (D) and to a H_2O molecule at the surface (E); amine groups coordinate to Zn^{2+} ions and hydrogen bond to a H_2O molecule at surface (F); second-shell ligands (G); free amine in solution (H).[121]

While, in the system of ZnO nanoparticle superlattice structures (NSS),[120] primary amine ligands and acids were both used to stabilize nanoparticles. The interaction force with ZnO surface was found mainly in the form of ion-paired ammonium carboxylate which is built through the hydrogen bond between amine and acid (see the scheme in Figure 8). With an increasing concentration of ZnO NPs, it can form superlattice structures with a size of approximately 90–100 nm. Several ligand shells which are composed of a lot of ion-paired ammonium carboxylate and inclusion of amine contribute to form NSS (see Figure 8, the right). At low concentration, de-association of the NSS occurs to form independent isotropic nanoparticles and the ion-paired ammonium carboxylate shells are replaced by amine shells (see Figure 9, the left). For example, ZnO obtained from a ZnO/HDA/0.5OlAc/THF colloidal solution show both the independent and organized nanoparticles (see Figure 9, the right). This suggests that the driving force of NSS formation is the existence of ion-paired ammonium carboxylate shells around the nanoparticle.[120]

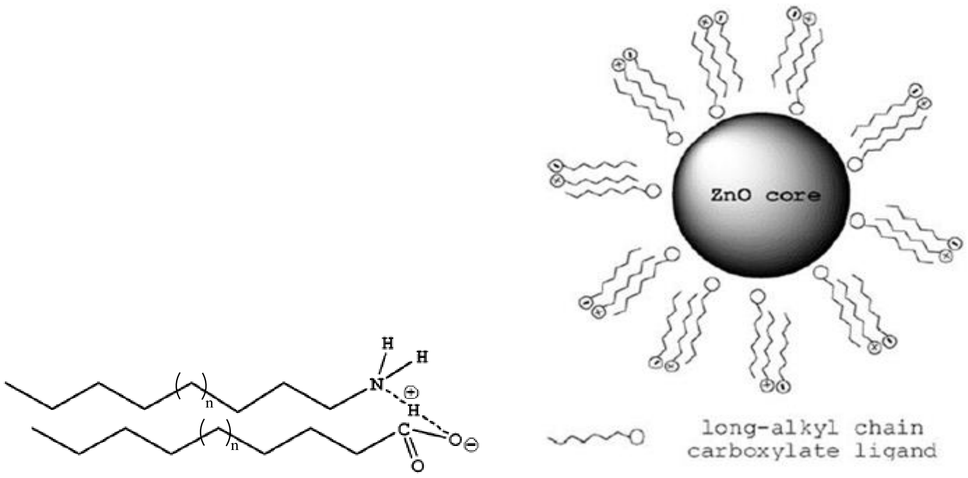

Figure 8. Scheme of Ion-paired ammonium and carboxylate moieties in nondissociating solvents (left); “Bilayer” model for the stabilization of ZnO nanocrystals with ammonium carboxylate ion pairs and an equivalent amount of long-alkyl-chain carboxylate ligand (right).[120]

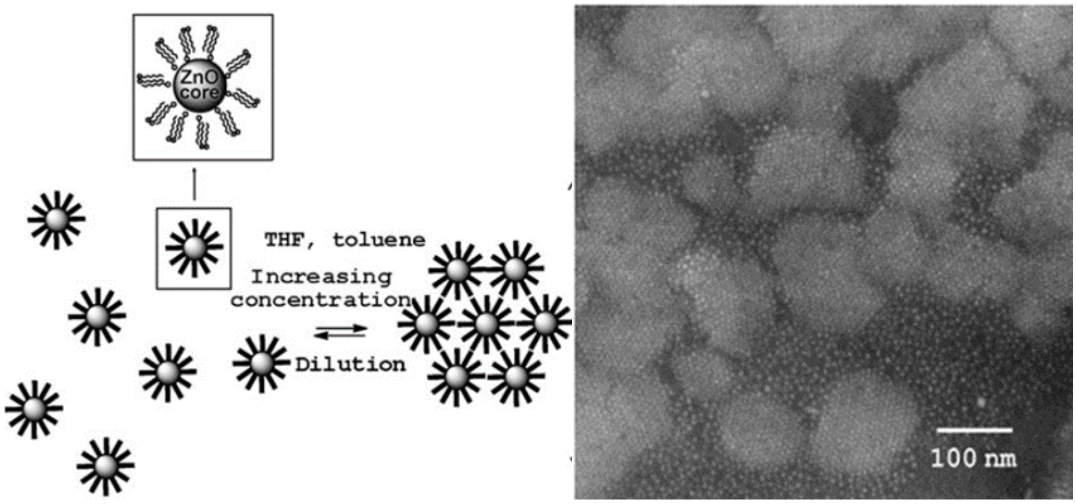

Figure 9. The concentration related reversible organization behavior of ZnO nanoparticles into superstructures (left); FEG-SEM image of the independent and organized ZnO nanoparticles obtained from a ZnO/HDA/0.5OlAc/THF colloidal solution (right).[120]

Third, the roles of ligands in aspects of luminescence properties.

In **1.2.2**, we briefly introduce that the luminescent (PL) properties of ZnO significantly depend on particles size, morphology, crystal structure and defects. Apart from these, it was also found that the emitting site can’t be altered by the environment (the medium or the type of ligand at the surface of the nanocrystals) but the composition of the ligand shell can influence the yellow emission intensity of ZnO nanocrystals.[122] In the system of ZnO/OA or ZnO/DDA NCs, the ligand shell is the primary alkylamine ligand.[114] When thiol ligands were added to ZnO/OA or ZnO/DDA NCs, the yellow emission was reduced significantly but the emission wavelength didn’t change.[122] It’s explained by the composition change of the ligand shell resulting from higher affinity of thiol ligands to the surface than alkylamines.

Besides the familiar observation of yellow emission, a new luminescent phenomenon-blue emission was also observed from the obtained ZnO nanoparticles in a recent work.[123] It was found the ratio between the blue and the yellow emissions is a function of mainly the alkyl chain length of the amine and the shape of the particles. The longer of the alkyl chain, the stronger intensity of the blue emission for nanoparticles. The longer of the rods, the stronger intensity of the blue emission. The origin of the blue emission was attributed to the presence of the amine at the surface and may be the consequence of the recombination of the photogenerated electron located in a shallow electron trapped level and the photogenerated hole located in the valence band or in a shallow hole level close to the valence band.

1.4.3 An interesting discovery: the gelification phenomenon

In **1.4.2**, we briefly mentioned the role of primary amine in controlling ZnO morphology: nanorods is obtained for short mixing time before hydrolysis while isotropic NPs is obtained for longer ones.[119] However, it's still worth recall that there exists an interesting reaction phenomenon involving Zn precursor (dicyclohexane zinc, [$Zn(Cy)_2$]) and dodecylamine (DDA). When mixing these two reactants together, a phase change form liquid to solid happens. After this phase change, a polymerization process occurs in three steps to form oligomeric species and cyclohexane as a side product (see scheme 2).

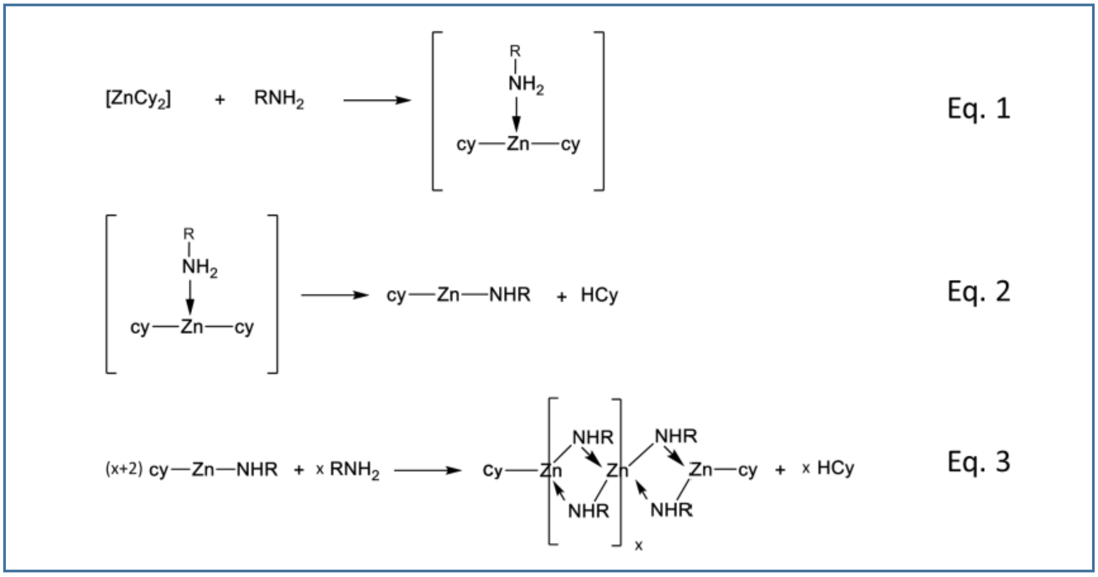

Scheme 2. Reaction path to form oligomer[119]

This oligomerization induces changes in the viscoelastic behavior of the solutions which behaves like a gel. Based on these interesting results, taking advantage of the formation of a gel with adjustable rheological properties to design processable hybrid materials for gas sensing property investigation is undoubtedly worth a try. This point will be discussed in the later sections.

1.5 The application of the as-prepared NPs in gas sensors

Properties determine applications. The feature of oxygen defect in ZnO determines it can not only be used in optical device but also as sensing materials in gas sensors.[124] The relation between ZnO morphology and its optical properties is briefly presented in **1.2.2**. Here the sensing properties of the as-prepared ZnO NPs is presented in this section as a further study direction in our group.

When talking about sensing properties, it mainly refers to response level and selectivity to the detected gases. It's believed that the morphology of ZnO nanostructures significantly influences its sensing properties.[125] For example, in our published work,[42] three kinds of ZnO nanoparticles: cloud-like nanoparticles, isotropic nanoparticles and nanorods synthesized by one-pot organometallic method were used to study their responses to CO, C_3H_8, and NH_3 at different operating temperatures (340–500 °C) and relative humidity of 50%. It was found sensors prepared with nanorods show the highest response to both CO and C_3H_8. Sensors made of isotropic nanoparticles and cloud-like structures show a lower but similar response to CO. Sensors made of CL structures show the weakest response to C_3H_8. This is due to the facts that: 1) the lateral faces of ZnO present a higher ratio of chemisorbed oxygen than the basal surfaces; 2) both basal and especially lateral faces are involved in the reactivity of ZnO to C_3H_8; 3) CL ZnO has poor crystallinity.

Thus, it's feasible to obtain the enhanced ZnO-based sensing materials via the controllable synthesis method.

1.6 Nuclear magnetic resonance (NMR) spectroscopy

To characterize previous species and follow chemical process, NMR characterization is one of the most frequently used techniques.

The NMR spectrum is normally classified into two types depending on the state of the sample: solution and solid-state NMR (SSNMR). Solution NMR normally has higher spectrum resolution, and is for samples which are diamagnetic, have low-viscosity and good solubility in the deuterium solvent. Whereas, due to the slow motion of the molecules in solid samples, spectrum of SSNMR normally has lower resolution with the presence of relative broader peaks.[126]

In solution NMR, Diffusion-Ordered Spectroscopy (DOSY) is an important method for measuring diffusion coefficient (D) of chemical specie in a liquid sample. This technique encodes translational motion in NMR data sets through the use of pulsed magnetic field gradient NMR (PFG-NMR) and an explicit mathematical relationship is built between the molecules diffusion coefficient (D) and the gradient field strength g.[127]

$$I = I_0 \mathrm{e}^{-D\gamma^2 g^2 \delta^2 (\Delta - \frac{\delta}{3})}$$

I_0 and I are the signal intensity before and after the introducing the pulse, respectively. γ is gyromagnetic ratio of the observed nucleus, δ is the pulse width. *Δ* is the time interval between two pulses, the diffusion time. D is the molecular diffusion coefficient, g is the field gradient strength.

The translational diffusion coefficients (D) of molecular species reflect their effective sizes and shapes. Each molecule has its own characteristic D when the variables of the experiment are controlled. For instance, if molecules of a certain surfactant are bonded to the surface or well organized in the solution, its D value is smaller than that of the free molecules.[128] Therefore, DOSY NMR allows the distinction of the chemical species in a complex systems and provides information about their intermolecular interactions.[127] [129] Using reverse laplace transformations 2D NMR DOSY spectra can be directly plotted. The x axis stands for the proton spectra while the y axis displays the diffusion coefficients of the molecule.

For samples that are insoluble or poorly soluble in the deuterated solvents or for samples like viscous liquid, gel and/or, large molecules (such as protein), etc…, the use of SSNMR technique complements DOSY NMR.

The SSNMR technique uses Magic-angle spinning (MAS): the sample spins rapidly at the magic angle (54.74°) with respect to the external magnetic field. MAS could suppress the anisotropic dipolar interactions. The combination of cross polarization and MAS allows one to obtain high resolution spectra for rigid solids because polarization from abundant nuclei ^{1}H can be transferred to rare nuclei ^{13}C, enhancing signal to noise and reducing waiting time between successive experiment.[127] Cross polarization magic angle spinning (CP-MAS) ^{13}C NMR spectroscopy is a very powerful tool for analyzing the structures and interactions of materials. Insensitive nuclei enhanced by polarization transfer (INEPT) MAS is through bond transfers between weakly coupled nuclei.[127] [130] Normally, the ^{13}C CP-MAS shows the information of the rigid segment, while ^{13}C INEPT-MAS shows the mobile segment. For example, in a dynamic study system which even involves in a phase transition, by the combination of signal intensities obtained with CP, and INEPT, site-specific qualitative information about molecular mobility can be obtained.[131] [132] In this process, motional amplitudes S are generally expressed in terms of a single order parameter. The correlation time τ_c is the average time it takes for a molecule to rotate one radian. Segment reorientation in an anisotropic system can be characterized with the correlation time τ_c and the order parameter S.[133] Solid state NMR which doesn't require crystalline materials like diffraction techniques, but can still determine local molecular environments, is clearly a very powerful technique capable of looking at a variety of materials.

In this thesis, these advance NMR technique methods are mainly used in the characterization of the synthesized ZnO hybrid material and the study of kinetic gelification. These aspects will be detailed introduced in the later sections.

1.7 Topic of Gelification

In **1.4.4,** in regard to the gelification phenomenon, the reaction path to form oligomer is briefly described. Herein, the followings are the general introductions of its conception, applications, rheology properties, together with strategies of leveraging gelification process to synthesize nanomaterials.

Gel can be described as a state of matter intermediate between solid and liquid. It is a diluted matrix of cross-linked system which contains fluids and shows no flow at its steady-state condition.[134] It possesses characteristics of both liquid and solid; high diffusion coefficients for small molecules; and mechanical properties of soft solids.[135]

A general liquid-solid gelification process is about a system with polymers in a sol or solution, a process of phase change from liquid to solid-state.[136] [137] In this process, liquid substances can be converted into solids with or without the help of a gelling agent. This process normally involves a rearrangement or self-assembly of the molecules via a certain force to form cross-links and entanglements and to build a network finally.[138]-[140] Along the evolution of the process, the fluidity and viscosity change accordingly.[141]

Polymer gels is one of the gels consisting of a polymer-solvent system in which a three-dimensional network composed of polymers or their associates (aggregates) hold a large amount of the solvent. It can be classified into two types: chemical and physical gels. Chemical gels involves covalent bonding (e.g., epoxy thermosets,[142] Figure 10), and are generally thermally irreversible. They can be prepared by the swelling of a preliminarily crosslinked polymer and network polymerization or polycondensation, as well as by the crosslinking of oligomers at the reactive terminal groups in a solvent medium. Physical gel involves multiple, weak non-covalent interactions (e.g., H-bonding, ionic bond, coordination bonding, π−π and van der waals interactions, and hydrophobic effects, Figure 11),[143]-[145] and are thermally reversible. Its formation can be induced by temperature, pH and salt concentration.

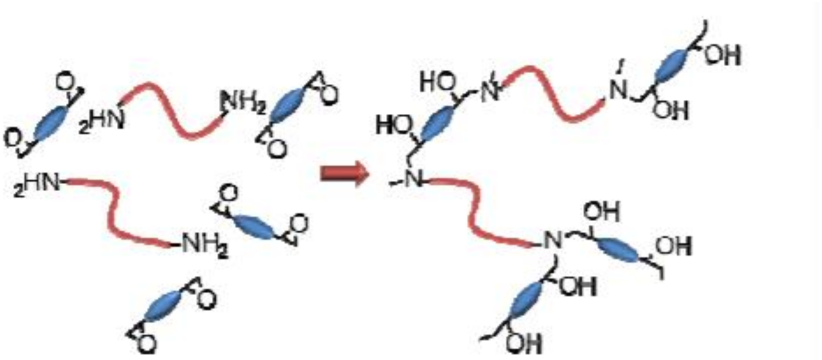

Figure 10: Growing of a three dimensional network from the reaction of a di-epoxide with a diamine.[142]

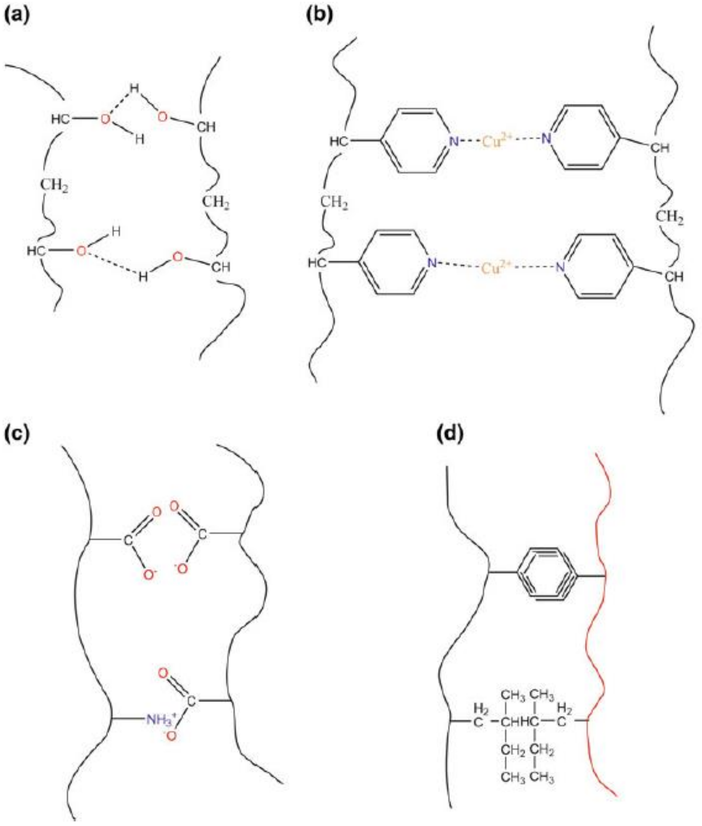

Figure 11. Forces controlling gel behavior; **a** hydrogen bonding; **b** coordination bonding; **c** ionic interactions; **d** hydrophobic interactions.

Gels have features of large swelling ability and medium absorption (reach as much as 10–20 times its molecular weight[146]) and resistance to dissolution. Its ability of swelling arises from hydrophilic functional groups attached to the polymeric chains, while the resistance of dissolution is attributed to the cross-links between polymer chains. This promotes gel to be considered as an ideal substance for absorbing materials employed in numerous applications like baby diaper and plant soil.[146]-[147] Gels can also be applied in foods,[148] [149] drug delivery[150] and adhesives.[151] Generally speaking, gel properties and its applications depend on its constituents, cross-links in terms of cross-linking mechanisms and density, and interactions between the molecular and solvent.[152]

1.7.1 Rheology properties of gel

Concepts and working principles.

Usually, an object or medium under external force will undergo deformation and flow change. The involved relationship between stress and deformation during the change is called rheology properties of the matter.[153][154] The gel is one kind of such material with viscoelastic behavior. It can show a mixture of viscous and elastic behavior when sheared. Conventionally, the way to study and evaluate its viscoelastic properties is through dynamic oscillatory shear experiment.[154] [155]

Herein, for better understanding how to use metrics to quantify the rheology properties of gel and the approaches to measure viscoelasticity with oscillatory shear method, a few physical terms and their conceptions related to deformation behavior are introduced firstly.[153] [154] [156]

Note that stress and strain are two key concepts in rheology research. Here a two-plates model is used to define various parameters (see Figure 12). The stress τ is the force per unit area of an object, which arises from externally applied forces F. The derived variable shear strain γ is the quantity that describes this deformation, and it's defined as the deflection path S divided by the distance h between the two parallel plates. The derived variable shear rate $\dot{\gamma}$ is the rate of change in velocity at which one layer of fluid passes over an adjacent layer. It's defined as the velocity of the moving plate divided by the gap distance h. The derived variable η is the viscosity of the studied materials. It's defined as shear stress τ divided by shear rate $\dot{\gamma}$. The derived variable G modulus is defined as the stress/strain ratio and refers the metric of materials overall resistance to deformation. For viscoelastic materials, in the oscillatory measurement, it's presented as G* and named complex shear modulus. It's defined as shear-stress amplitude τ_A divided by strain amplitude γ_A. The δ is the phase shift which refers the time lag between the shear stress and the strain. Their corresponding equations are as follows (Figure 13).

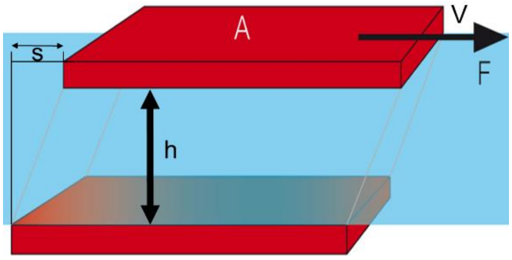

Figure 12: Two-plates model is used to define various parameters (the upper one is movable; the bottom one is stationary).

$$\tau = \frac{F}{A} \quad \gamma = \frac{s}{h} \quad \dot{\gamma} = \frac{v}{h} \quad \eta = \frac{\tau}{\dot{\gamma}} \quad G = \frac{\tau}{\gamma} \quad G^* = \frac{\tau_A}{\gamma_A}$$

Figure 13. The corresponding equations, where τ = the shear stress, *F* = the force applied, *A* = the cross-sectional area of material with area parallel to the applied force vector, γ = the shear strain, s = the deflection path, h = the distance between the two parallel plates, $\dot{\gamma}$ = the shear rate, υ = the velocity of the moving plate, η = the viscosity, G = the modulus, G* = the complex shear modulus, τ_A = the shear-stress amplitude, γ_A = the strain amplitude.

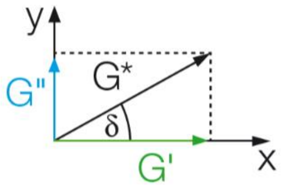

$$G' = \frac{\tau_A}{\gamma_A} \cos \delta \qquad G'' = \frac{\tau_A}{\gamma_A} \sin \delta$$

Figure 14. Vector diagram illustrating the relationship between complex shear modulus G*, storage modulus G' and loss modulus G" using the phase-shift angle δ. The elastic

portion of the viscoelastic behavior is presented on the x-axis and the viscous portion on the y-axis.

Secondly, in the dynamic oscillatory measurement, as a vector, the complex shear modulus G* can be a presentation of G* and δ (phase shift), as well as of G' (elastic modulus) and G'' (viscous modulus) (see Figure 14).[153] [154] They are corresponding to the storage modulus (G′) and loss modulus (G″). G′ represents a measure of the energy stored in the material per cycle of sinusoidal deformation. It is taken as an indication of the solid or elastic character of the material under test. Therefore, G’ = 0 for ideal viscous liquid. G″ represents a measure of the energy dissipated or lost (as heat) per cycle of sinusoidal deformation. The loss modulus G″ is taken as an indication of liquid or viscous behavior. The viscoelastic properties of the materials are usually characterized and evaluated by these two derived physical quantities.[157] For a viscoelastic material, G'' > G' indicates behavior of a viscoelastic liquid, and there are no such strong bonds between the individual molecules, for example, polymers without entanglements. G' > G'' suggests it shows behavior of a viscoelastic gel or solid, and there exists the cross links inside the material, for example, chemical bonds or structures with other strong interaction forces.[154]

Thirdly, for the test of gels, pastes, soft solids and polymer melts, parallel-plate measuring system (Figure 15) is usually used.[154] [158] [159] It’s one geometry type of rotational shearing rheometer. Other geometry types, such as type of cone and plate, type of concentric cylinders are not introduced here. A rotational rheometer fundamentally can provide the measure of torque (force), angular displacement, angular velocity. Concerning the measure options, it basically has two alternatives: controlled-stress and controlled-strain.[154] [158] In the controlled-stress rheometer, the upper plate is rotational, while the bottom one is static (Figure 15). The material is placed between the two plate. When the known stress is applied, the material responds by deforming (strain) and the displacement is carefully measured. After that, with the resulting shear strain and the known applied stress, the modulus can be calculated. Similarly, in the controlled-strain rheometer, the modulus can be obtained by commanding angular displacement (strain) and measuring torque (stress).

Figure 15. The parallel-plate type rotational shearing rheometer

In the oscillation experiment, apart from the option of stress and strain sweep, parameters such as time sweep, frequency sweep, temperature ramp and temperature sweep can also be changed to get extra information of the material.

It's worth mention that concerning the gel system part, in this thesis work, the time sweep method under the applied sinusoidal stress is adopted to conduct rheology study of gelification process and investigate evolutions, such as degradation, structure development and crosslinking during gelation process. This will be discussed in the later sections.

1.8 Project objectives

Generally speaking, project objectives are made based on the context of previous work. The context of this thesis work is described in the section of **1.4.2**.

The mature synthetic route, namely the organometallic method, of ZnO nanomaterials was developed first in our previous work. Then the well-defined ZnO nano-objects with different size, shape and morphology (isotropic and anisotropic ZnO) can be achieved through varying different parameters. Whereas, when primary amine was used as the ligand, it's still unclear about the mechanism of the anisotropic growth, and the factors that govern this anisotropic growth. In addition, the primary amines have being always used as the stabilizer in our research work. We never tried with secondary and tertiary amines. It's worth to try with secondary and tertiary amine and through comparison with the case of primary amine to figure out what and how their influences on ZnO morphology are.

Above are mainly more of studies on the synthesis or growth mechanism of ZnO nano-object. This thesis work also includes the study of the derived gel topic which is under the context of the involved gelification phenomenon found during the ZnO synthesis process. The discovered gel formation has been demonstrated to be related to the formation of the oligomers. Its kinetic studies via NMR characterization techniques and rheology properties study of the formed gel have been carried out in the case of DDA. However, other primary amines with different length of aliphatic chain or amines with steric hindrance haven't been done to investigate their influence on the kinetic of gelification and the rheology properties. Will the length of aliphatic chain have an effect of slowing down or accelerating its kinetic process? What's the leading role in the gelification process?

To answer these questions, in this thesis work, the project objectives can be summarized as below:

1. Leverage the 2-D plot analysis method and statistical analysis method, to control and understand the ZnO NPs anisotropic growth process through the simple organometallic pathway developed in our group, especially in the absence of solvent.
2. Introduce the factor of steric hindrance of amine functional group. In the case of secondary and tertiary amine, find out and understand the effect of the amine structure on the size/shape of ZnO NPs; figure out the key factor allowing the control of the anisotropic growth of ZnO and the role of surface dynamics in nanocrystal growth.
3. Figure out the driving force of gelification and investigate the evolution of rheology properties of the formed gel over time.

References

[1] G. A. Mansoori, T. F. Soelaiman, “Nanotechnology—an introduction for the standards community”, *J. ASTM Int.*, **2005**, *2*, 1-22.

[2] R. EMIL, “Nanoscopic Materials: Size Dependent Phenomena”, *The Royal Society of Chemical,* First Edition, United Kingdom, **2006**.

[3] S. Bhaviripudi, E. Mile, S. A. Steiner, A. T. Zare, M. S. Dresselhaus, A. M. Belcher, J. Kong, “CVD synthesis of single-walled carbon nanotubes from gold nanoparticle catalysts”, *J Am Chem Soc*, **2007**; 129,1516–1517.

[4] F. Chai, R. Tan, F. Cao, F. Zhai, X. Wang, C. Shao, Y. Liu, “Dendritic and tubular tungsten oxide by surface sol-gel mineralisation of cellulosic substance”, *Mater. Lett.* **2007**, *61*, 3939–41.

[5] N. Bi, X. Liu, N. Wu, C. Cui, Y. Sun, “Improved electrochemical performance of onion-like carbon coated magnetite nanocapsules as electromagnetic absorptive anode materials for lithium-ion batteries”, *RSC Adv.* **2015**, *5*, 32452–32459.

[6] P. S. Chaves, A. F Ourique, L. A. Frank, A. R. Pohlmann, S. S. Guterres, R.C.R. Beck, “Carvedilol loaded nanocapsules: mucoadhesive properties and permeability across the sublingual mucosa”, *Eur J Pharm Biopharm* **2017**; *114*, 88–95.

[7] L. S, Chin, M. Lim, T. T. Hung, C. P. Marquisc, R. Amala, “Perfluorodecalin nanocapsule as an oxygen carrier and contrast agent for ultrasound imaging”, *RSC Adv.*, **2014**; *4*, 13052–13060.

[8] B. Hu, L. P. Zhang, X. W. Chen, J. H. Wang, “Gold nanorod-covered kanamycin-loaded hollow SiO_2 (HSKAu rod) nanocapsules for drug delivery and photothermal therapy on bacteria”, *Nanoscale*, **2013**; *5*, 246–252.

[9] M. S. Bakshi, “How surfactants control crystal growth of nanomaterials”, *Cryst. Growth Des.* **2016**, *16*, 1104-1133.

[10] S. Wickramasinghe, J. Wang, B. Morsi, B. Li, “Carbon Dioxide Conversion to Nanomaterials: Methods, Applications, and Challenges”, *Energy Fuels*, **2021**, *35*, 11820-11834.

[11] Z. M. Tang, N. Kong, Q. Y. Jiang, Feng, F. Chan., N. Y. Kim, X. Y. Ji, C. Wang, C. O. Farokhzad, H. Zhang, W. Tao, “Phosphorus science-oriented design and synthesis of multifunctional nanomaterials for biomedical applications”, *Matter*, **2020**, *2*, 297-322.

[12] M, Nasrollahzadeh, S. M. Sajadi, M. Khalaj, “Green synthesis of copper nanoparticles using aqueous extract of the leaves of Euphorbia esula L and their catalytic activity for ligand-free Ullmann-coupling reaction and reduction of 4-nitropheno”, *RSC Adv.* **2014**, *4*, 47313–47318.

[13] M. Nasrollahzadeh, S. M. Sajadi, M. Maham, “Green synthesis of palladium nanoparticles using Hippophae rhamnoides Linn leaf extract and their catalytic activity for the Suzuki Miyaura coupling in water”, *J Mol Catal A: Chem* **2015**, *396*, 297–303.

[14] X. Yan, H. Li, T. Hu, X. Su, “A novel fluorimetric sensing platform for highly sensitive detection of organophosphorus pesticides by using egg white-encapsulated gold nanoclusters”, *Biosens Bioelectron*, **2017**; *91*, 232–7.

[15] Q. Li, R. Liu, B. Liu, L. Wang, K. Wang, D. Li, B. Zou, T. Cui, J. Liu, Z. Chenc, K. Yang, “Stability and phase transition of nanoporous rutile TiO_2 under high pressure”, *RSC Adv.*, **2012**, *2*, 9052–9057.

[16] W. H. Fissell, A. Dubnisheva, A. N. Eldridge, A. J. Fleischman, A. L. Zydney, S. Roy, “High performance silicon nanopore hemofiltration membranes”, *J. Membrane Sci.* **2009**; *326*, 58–63.

[17] S. B. Hu, L. Li, M. Y. Luo, Y. F. Yun, C. T. Chang, “Aqueous norfloxacin sonocatalytic degradation with multilayer flower-like ZnO in the presence of peroxydisulfate”, *Ultrason Sonochem*., **2017**; *38*, 446–454.

[18] G, Xu, X. Wang, X. Chen, L. Jiao, “Facile synthesis and phase transition of V_2O_3 nanobelts”, RSC Adv., **2015**; *5*, 17782–17785.

[19] Y. Huang, H. Li, M.S. Balogun, H. Yang, Y. Tong, X. Lu, H. Ji, “Three-dimensional TiO2/CeO2 nanowire composite for efficient formaldehyde oxidation at low temperature”, *RSC Adv.* **2015**; *5*, 7729–33.

[20] A. Mehdi, C. Reye, R. Corriu, “From molecular chemistry to hybrid nanomaterials. Design and functionalization”, *Chem. Soc. Rev.*, **2011**, *40*, 563-574.

[21] S. Zhang, C. I. Pelligra, X. Feng, C. O. Osuji, “Directed assembly of hybrid nanomaterials and nanocomposites”, *Adv. Mater.*,**2018**, *30*, 1705794.

[22] J. Yuan, A. H. Müller, “One-dimensional organic–inorganic hybrid nanomaterials”, *Polymer*, **2010**, *51*, 4015-4036.

[23] J. B. Goodenough, H. F. Barry, P.C.H. Mitchell (Eds.), Climax Comp., Proceedings of the 4th International Conference on the Chemistry and Uses of, Ann Arbor, MI, **1982**, 1.

[24] H. Gruber, E. Krautz,.”Untersuchungen der elektrischen Leitfähigkeit und des Magnetowiderstandes im System Molybdän-Sauerstoff”, *Phys. Status Solidi A* **1980**, *62*, 615-624.

[25] E. Canadell, M.-H. Wangbo, “Conceptual aspects of structure-property correlations and electronic instabilities, with applications to low-dimensional transition-metal oxides”, *Chem. Rev.*, **1991**, *91*, 965-1034.

[26] M. E. Franke, T. J. Koplin, U. Simon, “Metal and metal oxide nanoparticles in chemiresistors: does the nanoscale matter?”, *Small*, **2006**, *2*, 36–50.

[27] S. Brovelli, N. Chiodini, R. Lorenzi, A. Lauria, M. Romagnoli and A. Paleari, “Fully inorganic oxide-in-oxide ultraviolet nanocrystal light emitting devices”, *Nat. Commun.*, **2012**, *3*, 1-9.

[28] J. Mei, T. Liao, L. Kou, Z. Sun, “Two‐dimensional metal oxide nanomaterials for next‐generation rechargeable batteries”, *Adv. Mater.*, **2017**, *29*, 1700176.

[29] A. Akbari, M. Amini, A. Tarassoli, B. Eftekhari-Sis, N. Ghasemian, E. Jabbari, “Transition metal oxide nanoparticles as efficient catalysts in oxidation reactions”, *Nano-Structures & Nano-Objects*, **2018**, *14*, 19-48.

[30] P., Laube, “Fundamentals: Doping: n-and p-semiconductors. Semiconductor Technology from A to Z”, halbleiter. org, online. 2018. https://www.halbleiter.org/en/fundamentals/doping/.

[31] A. Yoshikawa, H. Matsunami, Y. Nanishi, “Development and applications of wide bandgap semiconductors”, Springer, Berlin, Heidelberg, In Wide Bandgap Semiconductors, **2017**, 1-24.

[32] R. Chidthong, “Theoretical Investigation on Structural and Electronic Properties of Fluorene-Pyridine Copolymer”, Kasetsart University, **2007**.

[33] J. H. Hou, M. H. Park, S. Q. Zhang, Y. Yao, L. M. Chen, J. H. Li, Y. Yang, “Bandgap

and Molecular Energy Level Control of Conjugated Polymer Photovoltaic Materials Based on Benzo1,2-b:4,5-b')dithiophene", *Macromolecules*, **2008**, *41l*, 2008 American Chemical Society.

[34] Y. Li, "Organic Optoelectronic Materials", Springer International Publishing Switzerland, **2015**.

[35] J. Tamaki, T. Hashishin, Y. Uno, D. V. Dao, S. Sugiyama, "Ultrahigh-sensitive WO_3 nanosensor with interdigitated Au nano-electrode for NO_2 detection", *Sens. Actuator B-Chem.*, **2008**, *132*, 234-238.

[36] C. G..Granqvist, "Electrochromic tungsten oxide films: review of progress 1993–1998", *Sol. Energy Mater Sol. Cells*, **2000**, *60*, 201-262.

[37] G. R. Bamwenda, K. Sayama, H. Arakawa, "The effect of selected reaction parameters on the photoproduction of oxygen and hydrogen from a WO_3–Fe^{2+}–Fe^{3+} aqueous suspension", *J. Photochem. Photobiol. A*, **1999**, *122*, 175-183.

[38] S.-W. Choi, A. Katoch, J.-H. Kim, S. S. Kim, "Prominent reducing gas-sensing performances of n-SnO_2 nanowires by local creation of p–n heterojunctions by functionalization with p-Cr_2O_3 nanoparticles", *ACS Appl. Mater. Interfaces*, **2014**, *6*, 17723-17729.

[39] J. Shi, J. Zhang, L. Yang, M. Qu, D. C. Qi, K. H. Zhang, "Wide bandgap oxide semiconductors: from materials physics to optoelectronic devices", *Adv. Mater.*, **2021**, 2006230.

[40] J. Chen, L. Xu, W. Li, X. Gou," Alpha-Fe_2O_3 nanotubes in gas sensor and lithium-ion battery applications", *Adv. Mater.*, **2005**, *17*, 582-586.

[41] C. Xia, Y. Jia, M. Tao, Q. Zhang, "Tuning the band gap of hematite α-Fe_2O_3 by sulfur doping", *Phys. Lett. A*, **2013**, *377*, 1943-1947.

[42] A. Ryzhikov, J. Jońca, M. Kahn, K. Fajerwerg, B. Chaudret, A. Chapelle, P. Ménini, C. H. Shim, A. Gaudon, P. Fau, "Organometallic synthesis of ZnO nanoparticles for gas sensing: towards selectivity through nanoparticles morphology", *J. Nanopart. Res.*, **2015**, *17*, 280.

[43] T. Zhou, T. Zhang, J. Deng, R. Zhang, Z. Lou, L. Wang, "P-type Co3O4 nanomaterials-based gas sensor: Preparation and acetone sensing performance", *Sens. Actuator B-Chem.*, **2017**, *242*, 369-377.

[44] J. Chen, A. Selloni, "Electronic states and magnetic structure at the Co_3O_4 (110) surface: A first-principles study", *Phys. Rev. B*, **2021**, *85*, 085306.

[45] V. Aravindan, P. Suresh Kumar, J. Sundaramurthy, W. C. Ling, S. Ramakrishna, S. Madhavi, "Electrospun NiO nanofibers as high performance anode material for Li-ion batteries", *J. Power Sources*, **2013**, *227*, 284-290.

[46] S. Thota, J. H. Shim, M. S. Seehra, "Size-dependent shifts of the Néel temperature and optical band-gap in NiO nanoparticles", *J Appl Phys.*, **2013**, *114*, 214307.

[47] P. W. Baumeister, "Optical Absorption of Cuprous Oxide", *Physical Review.*, **1961**, *121*, 359.

[48] W. Wang, L. Zhang, S. Tong, X. Li, W. Song, "Three-dimensional network films of electrospun copper oxide nanofibers for glucose determinatio", *Biosens. Bioelectron.*, **2009**, *25*, 708-714.

[49] Künneth, C., Batra, R., Rossetti Jr, G. A., Ramprasad, R., Kersch, A.

“Thermodynamics of Phase Stability and Ferroelectricity From First Principles”, In Ferroelectricity in Doped Hafnium Oxide”, Materials, Properties and Devices, Woodhead Publishing, 2019, 245-289.

[50] R. Fernández-Climent, S. Giménez, M. García-Tecedor, “The role of oxygen vacancies in water splitting photoanodes”, *Sustain. Energy Fuels*, **2020**, *4*, 5916-5926.

[51] Y. C. Kong, D. P. Yu, B. Zhang, W. Fang, S. Q. Feng, “Ultraviolet-emitting ZnO nanowires synthesized by a physical vapor deposition approach”, *Appl. Phys. Lett.*, **2001**, *78*, 407–409.

[52] P. S. Venkatesh, K. Jeganthan, “Investigations on the growth and characterization of vertically aligned zinc oxide nanowires by radio frequency magnetron sputtering”, *J. Solid State Chem.*, **2013**, *200*, 84–89.

[53] C. -L. Hsu, L. -F. Chang, T. -J. Hsueh, “Light-activated humidity and gas sensing by ZnO nanowires grown on LED at room temperature”, *Sens. Actuators, B*, **2017**, *249*, 265–277.

[54] A.R. Hutson, “Hall effect studies of doped zinc oxide single crystals”, *Phys. Rev.*, **1957**, *108*, 222.

[55] N. H. Nickel, E. Terukov, “Zinc Oxide—A Material for Micro- and Optoelectronic Applications”, Springer, Dordrecht, **2005**.

[56] E. K. Ellmer, A. Klein, B. Rech, “Transparent Conductive Zinc Oxide”, Springer, Berlin, **2008**.

[57] K. Davis, R. Yarbrough, M. Froeschle, J. White, H. Rathnayake, “Band gap engineered zinc oxide nanostructures via a sol–gel synthesis of solvent driven shape-controlled crystal growth”, *RSC advances*, **2019**, *9*, 14638-14648.

[58] S. Arya, P. Mahajan, S. Mahajan, A. Khosla, R. Datt, V. Gupta, S. K. Oruganti, “Influence of processing parameters to control morphology and optical properties of Sol-Gel synthesized ZnO nanoparticles”, *ECS J Solid State Sci Technol.*, **2021**, *10*, 023002.

[59] N. Kamarulzaman, M. F. Kasim, R. Rusdi, “Band gap narrowing and widening of ZnO nanostructures and doped materials”, *Nanoscale Res. Lett.*, **2015**, *10*, 1-12.

[60] B. Cao, W. Cai, H. Zeng, “Temperature-dependent shifts of three emission bands for ZnO nanoneedle arrays”, *Appl. Phys. Lett.*, **2006**, *88*, 161101.

[61] A. B. DJURIŠIĆ, Y. H. LEUNG, K. H. TAM, Y F Hsu, L Ding, W K Ge, Y C Zhong, K S Wong, W K Chan, H L Tam, K W Cheah, W M Kwok and D L Phillips, “Defect emissions in ZnO nanostructures”, *Nanotechnology*, **2007**, *18*, 095702.

[62] A. B. M. A Ashrafi, C. Jagadish, “Review of zinc blende ZnO: Stability of metastable ZnO phases”, *J Appl Phys.*, **2007**, *102*, 4.

[63] H. Morkoç, Ü. Özgür, “Zinc oxide: fundamentals”, materials and device technology. John Wiley & Sons, **2008**.

[64] A. S. KAMBLE, B. B. SINHA, K. CHUNG, M. G. Gil, V. Burungale, C. J. Park, J. H. Kim, P. S. Patil, “Effect of hydroxide anion generating agents on growth and properties of ZnO nanorod arrays”, *Electrochim. Acta*, **2014**, *149*, 386-393.

[65] C. Wöll, “The chemistry and physics of zinc oxide surfaces”, *Prog. Surf. Sci.*, **2007**, *82*, 55-120.

[66] Y. Zhang, “ZnO Nanostructures: Fabrication and Applications”, *Royal Society of*

Chemistry, **2017**, *43*.

[67] B. G. Shohany, A. K. Zak, “Doped ZnO nanostructures with selected elements-Structural, morphology and optical properties: A review”, *Ceram.Int.*, **2020**, *46*, 5507-5520.

[68] W. I. Park, Y. H. Jun, S. W. Jung, G. C. Yi, “Excitonic emissions observed in ZnO single crystal nanorods”, *Appl. Phys. Lett.*, **2003**, 82, 964-966.

[69] K. P. Jayadevan, T. Y. Tseng, “Oxide nanoparticles’’, *ChemInform*, **2005**, 36.

[70] S. Li, S. J. Silvers, M. S. El-Shall, “Preparation, characterization and optical properties of zinc oxide nanoparticles”, *Mater. Res. Symp. Proc.* **1997**, 452, 389.

[71] L. E. Brus, “Electron–electron and electron‐hole interactions in small semiconductor crystallites: The size dependence of the lowest excited electronic state”, *J. Chem. Phys.*, **1984**, *80*, 4403-4409.

[72] S. Agarwal, L. K. Jangir, K. S. Rathore, M. Kumar, K. Awasthi, “Morphology-dependent structural and optical properties of ZnO nanostructures”, *Applied Physics A*, **2019**, *125*, 1-7.

[73] K. Ueda, H.Tabata, T. Kawai, “Magnetic and electric properties of transition-metal-doped ZnO films”, *Appl. Phys. Lett.*, **2001**, *79*, 988-990.

[74] A. C.Tuan, J. D. Bryan, A. B. Pakhomov, V. Shutthanandan, S. Thevuthasan, D. E. McCready, D. Gaspar, M. H. Engelhard, J. W. Rogers, Jr., K. Krishnan, D. R. Gamelin, S. A. Chambers, “Epitaxial growth and properties of cobalt-doped ZnO on alpha-Al_2O_3 single-crystal substrates”, *Phys. Rev. B*, **2004**, *70*, 054424.

[75] N. S. Norberg, K. R. Kittilstved, J. E. Amonette, R. K. Kukkadapu, D. A. Schwartz, D. R. Gamelin, “Synthesis of colloidal Mn^{2+}: ZnO quantum dots and high-Tc ferromagnetic nanocrystalline thin films”, *J. Am. Chem. Soc.*, **2004**, *126*, 9387-9398.

[76] A. S. Pereira, M. Peres, M. J. Soares, E. Alves, A. Neves, T. Monteiro, T. Trindade, “Synthesis, surface modification and optical properties of Tb^{3+}-doped ZnO nanocrystals”, *Nanotechnology*, **2006**, *17*, 834-839.

[77] C. Messaoudi, S. Abd-lefdil, D. Sayah, M. Cadene, “ZnO layers prepared by spray pyrolysis”, *Eur. Phys. J. Appl. Phys.*, **1998**, *1*, 181-184.

[78] S. Barbhuiya, M. Qureshi. “Applications of Nanotechnology in Cement and Concrete Science”, **2014**, doi: 10.4018/978-1-4666-6363-3.ch029.

[79] G. Oskam, “Metal oxide nanoparticles: synthesis, characterization and application”, *J Solgel Sci Technol.*, **2006**, *37*, 161-164.

[80] D. Dobkin, M. K. Zuraw, “Principles of Chemical Vapor Deposition”, Springer Science & Business Media, **2003**.

[81] W. I. Park, D. H. Kim, S. W. Jung, G. C. Yi, “Metalorganic vapor-phase epitaxial growth of vertically well-aligned ZnO nanorods”, *Appl. Phys. Lett.,* **2002**, *80*, 4232-4234,.

[82] W. I. Park, G. C. Yi, M. Y. Kim, S. J. Pennycook, “ZnO nanoneedles grown vertically on Si substrates by non‐catalytic vapor‐phase epitaxy”, *Adv. Mater.*, **2002**, *14*, 1841-1843.

[83] S. Polarz, A. Roy, M. Merz, S. Halm, D. Schroder, L. Schneider, G. Bacher, F. E. Kruis, M. Driess, “Chemical vapor synthesis of size‐selected zinc oxide nanoparticles”, *Small*, **2005**, *1*, 540–552.

[84] M. D. Barankin, Ii, E. Gonzalez, A. M. Ladwig, R. F. Hicks, “Plasma-enhanced chemical vapor deposition of zinc oxide at atmospheric pressure and low temperature”, *Sol. Energy Mater Sol. Cells*, **2007**, *91*, 924-930.

[85] S. Suehiro, T. Kimura, D. Yokoe, S., Takahashi, “Synthesis of highly c-axis-oriented ZnO thin films using novel laser-enhanced electrospray CVD under atmospheric pressure”, *CrystEngComm*, **2017**, *19*, 5995-6001.

[86] T. A. Polley, W. B. Carter, “Zone model for zinc oxide deposited by combustion chemical vapor deposition”, *Thin Solid Films*, **2001**, *384*, 177-184.

[87] C. J. Brinker, G. W. Scherer, “Sol-gel science: the physics and chemistry of sol-gel processing*”*. Academic press, 2013.

[88] A. Shokuhfar, J. Samei, A. E. Kandjani, M. R. Vaezi, “Synthesis of ZnO Nanoparticles via Sol-Gel Process Using Triethanolamine as a Novel Surfactant”, *In Defect and Diffusion Forum, Trans Tech Publications Ltd*, **2008**, *273*, 626-631.

[89] L. Guo, S. Yang, Ch. L. Yang, P. Yu, J. N. Wang, W. K. Ge, G. K. L. Wong “Synthesis and characterization of poly(vinylpyrrolidone)-modified zinc oxide nanoparticles”, *Chem. Mater.*, **2000**, *12*, 2268-2274.

[90] M., Abdullah, I. W. Lenggoro, K. Shi, F. G. Okuyama, “In situ synthesis of polymer nanocomposite electrolytes emitting a high luminescence with a tunable wavelength”, *J Phys Chem B.* **2003**, *107*, 1957-1961.

[91] T. H. Mahato, G. K. Prasad, B.S.J. Acharya, A.R. Srivastava, R. Vijayaraghavan, “Nanocrystalline zinc oxide for the decontamination of sarin”, *J. Hazard. Mater.,* **2009**, *165*, 928–932.

[92] H. Benhebal, M. Chaib, T. Salomon, J. Geens, A. Leonard, S.D. Lambert, M. Crine, B. Heinrichs, “Photocatalytic degradation of phenol and benzoic acid using zinc oxide powders prepared by sol-gel process”, *Alex. Eng. J.* **2013**, *52*, 517–523.

[93] M. Ristić, S. Musić, M. Ivanda, S. Popović, “Sol–gel synthesis and characterization of nanocrystalline ZnO powders”, *J. Alloy. Compd.* **2005**, *39*, L1–L4.

[94] S. Yue, Z. Yan, Y. Shi, G. Ran, “Synthesis of zinc oxide nanotubes within ultrathin anodic aluminum oxide membrane by sol-gel method”, *Mater. Lett.,* **2013**, *98*, 246–249.

[95] R. Hong, T. Pan, J. Qian, H. Li, “Synthesis and surface modification of ZnO nanoparticles”, *Chem. Eng. J.* **2006**, *119*, 71–81.

[96]. A. Kołodziejczak-Radzimska, T. Jesionowski, A. Krysztafkiewicz, “Obtaining zinc oxide from aqueous solutions of KOH and $Zn(CH_3COO)_2$”, *Physicochem. Probl. Miner. Process.* **2010**, *44*, 93–102.

[97]. J. Xu, Q. Pan, Y. Shun, Z. Tian, “Grain size control and gas sensing properties of ZnO gas sensor”, *Sens. Actuators B Chem.* **2000**, *66*, 277–279.

[98] A.S. Lanje, S. J. Sharma, R. S. Ningthoujam, J. S. Ahn, R. B. Pode, “Low temperature dielectric studies of zinc oxide (ZnO) nanoparticles prepared by precipitation method”, *Adv. Powder Technol.*, **2013**, *24*, 331–335.

[99]. Y. Wang, C. Zhang, S. Bi, G. Luo, “Preparation of ZnO nanoparticles using the direct precipitation method in a membrane dispersion micro-structured reactor”, *Powder Technol.* **2010**, *202*, 130–136.

[100] W. Jia, S. Dang, H. Liu, Z. Zhang, Ch. Yu, X. Liu, B. Xu, “Evidence of the formation mechanism of ZnO in aqueous solution”, *Mater. Lett.*, **2012**, *82*, 99–101.

[101] Z. Cao, Z. Zhang, F. Wang, G. Wang, “Synthesis and UV shielding properties of zinc oxide ultrafine particles modified with silica and trimethyl siloxane”, *Colloids Surf. A Physicochem. Eng. Asp.* **2009**, *340*, 161–167.

[102] Z. M. Khoshhesab, M. Sarfaraz, Z. Houshyar, “Influence of urea on precipitation of zinc oxide nanostructures through chemical precipitation in ammonium hydrogen carbonate solution”, *Synth. React. Inorg. Met. Org. Nano Met. Chem.* **2012**, *42*, 1363–1368.

[103] K. M. Kumra, B. K. Mandal, E. A. Naidu, M. Sinha, K.S. Kumar, P. S. Reddy, “Synthesis and characterization of flower shaped zinc oxide nanostructures and its antimicrobial activity”, *Spectrochim. Acta Part A Mol. Biomol. Spectrosc*. **2013**, *104*, 171–174.

[104] Y. Wang, C. Ma, S. Xun, H. Li, “Preparation of nanocrystalline metal oxide powders with the surfactant-mediated method”, *Inorg. Chem. Commun.* **2002**, *5*, 751–755.

[105] P. Li, Y. Wei, H. Liu, X. K. Wang, “Growth of well-defined ZnO microparticles with additives from aqueous solution”, *J. Solid State Chem.* **2005**, *178*, 855–860.

[106] F. Dumestre, B. Chaudret, C.,Amiens, P. Renaud, P. Fejes, “Superlattices of iron nanocubes synthesized from $Fe[N(SiMe_3)_2]_2$”, *Sci.*, **2004**, *303*, 821-823

[107] F. Dumestre, B. Chaudret,C. Amien ,M. C. Fromen, M. J. Casanove, P. Renaud, P. Zurcher, “Shape control of thermodynamically stable cobalt nanorods through organometallic chemistry”, *Angew. Chem. Int. Ed.*, **2002**, *41*, 4286-4289.

[108] S. Jansat, M. Gómez, K. Philippot, G. Muller, E. Guiu, C. Claver, S. Castillón, B. Chaudret, “A case for enantioselective allylic alkylation catalyzed by palladium nanoparticles”, *J. Am. Chem. Soc.*, **2004**, *126*, 1592-1593,

[109] C. Desvaux, C. Amiens, P. Fejes, P. Renaud, M. Respaud, P. Lecante, E. Snoeck, B. Chaudre, “Multimillimetre-large superlattices of air-stable iron-cobalt nanoparticles”, *Nat. Mater.*, **2005**, *4*, 750-753.

[110] K. Soulantica, A. Maisonnat, M. C. Fromen, M. J., Casanove, B. Chaudret, “Spontaneous formation of ordered 3D superlattices of nanocrystals from polydisperse colloidal solutions”, *Angew. Chem. Int. Ed.*, **2003**, *42*, 1945-1949.

[111] K. Soulantica, L. Erades, M. Sauvan, F. Senocq, A. Maisonnat, B. Chaudret, “Synthesis of indium and indium oxide nanoparticles from indium cyclopentadienyl precursor and their application for gas sensing”, *Adv. Funct. Mater.*, **2003**, *13*, 553-557.

[112] M. Verelst, T. O. Ely, C. Amiens, E. Snoeck, P. Lecante, A. Mosset, M. Respaud, J. M. Broto, B. Chaudret, “Synthesis and characterization of CoO, Co_3O_4, and mixed Co/CoO nanoparticules”, *Chem. Mater.*, **1999**, *11*, 2702-2708.

[113] M. Monge, M. L. Kahn, A. Maisonnat, B. Chaudret, “Room-temperature organometallic synthesis of soluble and crystalline ZnO nanoparticles of controlled size and shape”, *Angew. Chem. Int. Ed.*, **2003**, *42*, 5321-5324,

[114] M. L. Kahn, M. Monge, V. Colliere, F. Senocq, A. Maisonnat, B. Chaudret, “Size- and shape‐control of crystalline zinc oxide nanoparticles: a new organometallic synthetic method”, *Adv. Funct. Mater.,* **2005**, *15*, 458-468.

[115] M. L. Kahn, M. Monge, E. Snoeck, A. Maisonnat, B. Chaudret, “Spontaneous formation of ordered 2D and 3D superlattices of ZnO nanocrystals”, *Small*, **2005**, *1*,

221-224.

[116] Spataro, G., Champouret, Y., Florian, P., Coppel, Y., Kahn, M. L., “Multinuclear solid-state NMR study: a powerful tool for understanding the structure of ZnO hybrid nanoparticles”, *Phys. Chem. Chem. Phys.*, **2018**, 12413-12421.

[117] D. Ling, M. J. Hackett, T. Hyeon, “Surface ligands in synthesis, modification, assembly and biomedical applications of nanoparticles”, *Nano Today*, **2014**, *9*, 457–477.

[118] J. Rubio-Garcia, A. Dazzazi, Y. Coppel, P. Mascalchi, L. Salomé, A. Bouhaouss, M. L. Kahn, F. Gauffre, "Transfer of hydrophobic ZnO nanocrystals to water: an investigation of the transfer mechanism and luminescent properties", *J. Mater. Chem.*, **2012**, *22*, 14538-14545.

[119] Z. Zhao, Y. Coppel, J. Fitremann, P. Fau, C. Roux, C. Lepetit, P. Lecante, J.-D. Marty, C. Mingotaud, M. L. Kahn, “Mixing Time between Organometallic Precursor and Ligand: A Key Parameter Controlling ZnO Nanoparticle Size and Shape and Processable Hybrid Materials”, *Chem. Mater.*, **2018**, *30*, 8959-8967.

[120] Y. Coppel, G. Spataro, V. Collière, B. Chaudret, C. Mingotaud, A. Maisonnat, M. L. Kahn, "Self‐Assembly of ZnO Nanoparticles–An NMR Spectroscopic Study", *Eur. J. Inorg. Chem*., **2012**, *2012*, 2691-2699.

[121] Y. Coppel, G. Spataro, C. Pagès, B. Chaudret, A. Maisonnat and M. L. Kahn, "Full characterization of colloidal solutions of long-alkyl-chain-amine-stabilized ZnO nanoparticles by NMR spectroscopy: surface state, equilibria, and affinity", *Chem. Eur. J.,* **2012**, *18*, 5384-5393.

[122] G. Spataro, A. Dazzazi, S. Fortuny, Y. Champouret, Y. Coppel, J. Rubio‐Garcia, M. L. Kahn, “Insight into the role of ligands in the yellow luminescence of zinc oxide nanocrystals”, *Eur. J. Inorg. Chem.*, **2016**, *13-14*, 2056-2062.

[123] M. L. Kahn, T. Cardinal, B. Bousquet, M. Monge, V. Jubera, B. Chaudret, “Optical properties of zinc oxide nanoparticles and nanorods synthesized using an organometallic method”, *ChemPhysChem*., **2006**, *7*, 2392-2397.

[124] Bhati V S, Hojamberdiev M, Kumar M. “Enhanced sensing performance of ZnO nanostructures-based gas sensors: A review”, *Energy Rep.*, **2020**, *6*: 46-62.

[125] L. Zhu, W. Zeng, “Room-temperature gas sensing of ZnO-based gas sensor: A review”, *Sens. Actuator A Phys.*, **2017**, *267*, 242-261.

[126] F. Chen, “Basic Principles and Applications of Solid-State NMR in Catalysis”, *J. Thermodyn. Catal.*, **2014**, *5*, 1.

[127] C. S. JOHNSON, “Diffusion ordered nuclear magnetic resonance spectroscopy: principles and applications”, *ChemInform*, **1999**, *30*, 203-256; T. D. W. Claridge, “High-Resolution NMR Techniques in Organic Chemistry”, *Elsevier*, 3rd Ed, Chapter 10.

[128] Y. Coppel, G. Spataro, C. Pagès, B. Chaudret, A. Maisonnat and M. L. Kahn, "Full characterization of colloidal solutions of long-alkyl-chain-amine-stabilized ZnO nanoparticles by NMR spectroscopy: surface state, equilibria, and affinity", *Chem. Eur. J.*, **2012**, *18*, 5384-5393.

[129] G. Pagès,V. Gilard,R. Martino,M. Malet-Martino “Pulsed-field gradient nuclear magnetic resonance measurements (PFG NMR) for diffusion ordered spectroscopy (DOSY) mapping”, *Analyst*, **2017**, *142*, 3771–3796.

[130] C. A. Fyfe, K. C. Wongmoon, Y. Huang, H. Grondey, “INEPT experiments in solid-state NMR”, *J. Am. Chem. Soc.*, **1995**, *117*, 10397-10398.

[131] D. E. Warschawski, P. F. Devaux, “^{1}H–^{13}C polarization transfer in membranes: a tool for probing lipid dynamics and the effect of cholesterol”, J*. Magn. Reson.*, **2005**, *177*, 166-171.

[132] F. M. Mulder, W. Heinen, M. van Duin, J. Lugtenburg, H. J. M. de Groot, “Spin Diffusion with ^{13}C Selection and Detection for the Characterization of Morphology in Labeled Polymer Blends with MAS NMR” *J. Am. Chem. Soc.* **1998,** *120,* 12891-12894.

[133] B. Halle, H. Wennerström, “Interpretation of magnetic resonance data from water nuclei in heterogeneous systems”, *J. Chem. Phys.*, **1981**, *75*, 1928-1943.

[134] A. C. Jen, M. C. Wake, A. G. Mikos, “Review: hydrogels for cell immobilization”, *Biotechnol Bioeng*, **1996**, *50*, 357–364.

[135] A. Singh, P. K. Sharma, V. K. Garg, G. Garg, “Hydrogels: a review”, *Int J Pharm Sci. Rev. Res.*, **2010**, *4*, 97–105.

[136] M. Djabourov, “Gelation—A review”, *Polym. Int.*, **1991**, *25*, 135-143.

[137] S. Slomkowski, J. V. Alemán, R. G. Gilbert, M. Hess, K. Horie, R. G. Jones, R. F. Stepto, “Terminology of polymers and polymerization processes in dispersed systems (IUPAC Recommendations 2011)”, *Pure Appl. Chem.*, **2011**, *83*, 2229-2259.

[138] P. G. De Gennes, “Scaling Concepts in Polymer Physics”, 1979, Cornell University Press.

[139] D. De Rossi, K. Kajiwara, Y. Osada and A. Yamauchi, “Polymer Gels”, Plenum Press, **1991**.

[140] W. H. Carothers, “Polymers and polyfunctionality”, *Trans. Faraday. Soc.*, **1936**, *32*, 39.

[141] G. Odian, “Principles of polymerization”, John Wiley & Sons, **200**4.

[142] T. Vidil, F. Tournilhac, S. Musso, A. Robisson, L. Leibler, “Control of reactions and network structures of epoxy thermosets”, *Prog. Polym. Sci.*, **2016**, *62*, 126-179.

[143] J. H. Jung, G. John, M. Masuda, K. Yoshida, S. Shinkai, T. Shimizu, “Self-assembly of a sugar-based gelator in water: Its remarkable diversity in gelation ability and aggregate structure”, *Langmuir,* **2001**, *17*, 7229–7232.

[144] G. Chen, M. Jiang, “Cyclodextrin-based inclusion complexation bridging supramolecular chemistry and macromolecular self-assembly”, *Chem. Soc. Rev.*, **2011**, *40*, 2254–2266.

[145] P. I. Hurtado, L. Berthier, W. Kob, “Heterogeneous diffusion in a reversible gel”, *Phys. Rev. Lett.*, **2007**, *98*, 98–101.

[146] A, Singh, P. K. Sharma, V. K. Garg, G. Garg, “Hydrogels: a review”, *Int J Pharm Sci Rev Res.*, **2010**, *4*, 97–105.

[147] E. M. Ahmed, “Hydrogel: preparation, characterization, and applications: a review”, *J. Adv. Res.*, **2015**, *6*,105–121.

[148] S. B. Ross-Murphy, “Structure-Property Relationships in Food Biopolymer Gels and Solutions”, *J. Rheol,* **1995**, *39*, 1451-1463.

[149] M. H. Tunick, “Small-Strain Dynamic Rheology of Food Protein Networks”, *J. Agric. Food Chem.*, **2010**, 59, 1481-1486.

[150] G. P. Andrews, D. S. Jones, “Rheological Characterization of Bioadhesive Binary

Polymeric Systems Designed as Platforms for Drug Delivery Implants”, Biomacromolecules, **2006**, *7*, 899-906.

[151] C. Creton, “Pressure-Sensitive Adhesives: An Introductory Course”, MRS Bulletin, **2003**, *28*, 434-439.

[152] K. Pal, V.K. Singh, A. Anis, G. Thakur, M.K. Bhattacharya, “Hydrogel-based controlled release formulations: designing considerations, characterization techniques and applications”, *Polym Plast Technol Eng* ,**2013**, *52*,1391–1422.

[153] T. G. Mezger, “Applied rheology: with Joe flow on rheology road”, Anton Paar, 2015.

[154] T. Mezger, “The rheology handbook”, Vincentz Network, **2020**.

[155] T Tanaka, D Fillmore, ST Sun, I Nishio, G Swislow, A Shah., “Phase transitions in ionic gels”, *Phys Rev Litt.*, **1980**, *45*,1636–1639.

[156] R.C. Hibbeler, “Mechanics of Materials”, New Jersey USA: Pearson Education. **2004**, p. 32.

[157] N. Chereminisoff, “An introduction to polymer rheology and processing”, CRC Press, London, **1993**.

[158] A. G. Marangoni, “Structure-function analysis of edible fats”, Elsevier, **2018**.

Chapter II. Mechanistic insights into the anisotropic growth of ZnO nanoparticles deciphered through 2D size plots and multivariate analysis

2.1 Introduction

As discussed in the previous chapter, many chemical procedures have been developed to control the nanoparticles' (NPs) size, polydispersity, shape, surface, volume chemical composition, etc.[1]-[3] Metallic,[4] [5] II-VI or III-V semiconducting NPs[6]-[11] are nowadays synthesized with a simple isotropic shape or more elaborate core-shell structures,[12] cubes,[13] stars,[14] bipyramidal architectures,[15] rods,[16] nanowires,[17] etc., are also largely described. In general, variation of the size and shape is dependent on the experimental chemical conditions and the proposed mechanisms.[18]-[21] Yet, a number of challenges remain, including evidencing and understanding the relationship between the experimental parameters of the synthesis and the shape of the NPs, this latter driving the NP's properties.

The aim of this chapter is to demonstrate how simple analytical tools based on statistical analysis can help us to decipher the anisotropic growth of NPs and to better understand and control the parameters governing this anisotropic growth. ZnO NPs were taken as a model system and were prepared by taking advantage of the exothermic hydrolysis of dicyclohexyl zinc precursor, [$Zn(Cy)_2$]. In one step and under mild conditions (*i.e.* room temperature and atmospheric pressure), well-defined crystalline ZnO NPs can then be synthesized.[22] In this process, the control of the morphology (*i.e.* either isotropic NPs or nanorods) is achieved by varying the experimental conditions: isotropic NPs are obtained in the presence of alkyl chain amine ligands in an organic solvent while nanorods are obtained in the same experimental conditions but in the absence of solvent.[23] Up to now, experimental results suggest the critical role of different parameters like the composition of the reaction mixture, the amount of water, the kinetics parameters of the reaction, the temperature…

To gain information on the parameters of importance for the growth of such nanorods and to better understand the growth processes, we studied the kinetics of formation of anisotropic ZnO NPs in different conditions by using two different analytical tools enabling the analysis of TEM images: 2D size plots and multivariate statistical analysis. The first one, 2D size plot, enables to extract information of the correlation between widths and lengths of anisotropic objects.[24] Each particle is characterized by two sizes, noted D1 and D2, measured on perpendicular axes. These two sizes generally correspond to the length and width of the nano-objects. For each particle and on a same graph, we plot D1 as a function of D2 and also D2 as a function of D1. The aspect ratio of the particle (noted AR) is defined as the ratio between the two lengths $AR = D1/D2$ (with $D1>D2$). It is related to a θ angle through the equation $AR = \tan\theta$. Higher anisotropy in the shape of a particle corresponds to higher AR value and to a theta angle closer to 90° in the proposed 2D plot. Nevertheless, the quantitative analysis of these data might be hampered by the presence of different sub-populations that could be tedious procedures to separate them, especially when these populations overlap each other. In order to identify them numerically and to obtain their own statistical parameters like average length and width, corresponding standard deviations, and correlation between length and width, a complementary multivariate analysis was performed[24] with the MIXMOD software (http://mixmod.org) using R package (http://www.r-project.org/). Apart from the Gaussian character of the probability densities, no assumption about the orientation, shape, and volume of the different sub-populations was made during calculation. The number of sub-populations that composed the point clouds was fixed by the user or chosen numerically thanks to the BIC criteria (Bayesian Information Criterion). Each sub-population was then characterized by the mean of the two studied variables (i.e., short and long axis lengths), as well as the corresponding standard deviations. Additionally, the correlation parameter ρ between both variables was calculated. The correlation is equal to zero when the two variables are totally independent and equal to 1 when they are affinely related to each other.

Here, we study the hydrolysis rate, the mixing time before hydrolysis, the length of the ligand aliphatic chain, and the amount of water on the anisotropic growth of ZnO NPs. In a typical experiment, the dicyclohexyl zinc precursor, $[Zn(Cy)_2]$, is mixed at room temperature with two equivalents of alkylamine RNH_2 (dodecylamine, DDA, R = $C_{12}H_{25}$) as ligand. No solvent was used. After 10 minutes, water is introduced by opening the vial. The atmospheric water vapor will induce a hydrolysis reaction leading to the formation of ZnO NPs. 2D size plots were constructed from TEM pictures and the measurements were analyzed thanks to a multivariate analysis.

The following paragraphs will successively describe the effect of the time of hydrolysis, the mixing time of the mixture of reagents before hydrolysis, the amount of water, the speeding rate of water addition, and the length of the ligand aliphatic chain on the ZnO NP morphology. It has to be mentioned that the temperature of the reaction medium is also of crucial importance. Anisotropic NPs were only obtained when temperature was kept below the critical value of 60°C to maintain the local organization of the fatty amines surrounding the growing ZnO NPs.[25] All the studies were therefore made at room temperature.

2.2 Effect of the time of hydrolysis

Advantageously, 2D size plots are of special interest to describe the modifications of NPs *versus* time during growing or aging process. In a first series of experiments, TEM grids were prepared from the same synthesis followed over time. Width and length of these NPs extracted from the TEM pictures allow one to draw the 2D size plots as a function of time (Figure 1). The point clouds obtained at 1 and 2 h are centered on the median. This corresponds to the presence of isotropic NPs. The growth of ZnO NPs clearly starts by a nucleation step where pristine isotropic NPs are formed.

Table 1**.** Multivariate analysis of the 2D plots corresponding to the TEM images of the Figure 1 (ZnO NPs versus hydrolysis time from 1 to 240 hours) through Rmixmod program[26] [27] (the dispersion is given as twice the standard deviation obtained from calculations, and multivariate analysis).

Hydrolysis time (hour)	Length (nm)	Width (nm)	Correlation
1	3.2 ± 1.6	2.1 ± 1.1	0.60
2	3.2 ± 1.8	2.0 ± 1.0	0.50
4	3.5 ± 2.5	2.5 ± 1.7	0.79
8	6.4 ± 7.6	3.0 ± 2.4	0.58
24	11.0 ± 8.2	4.1 ± 1.7	0.20
32	21.9 ± 36.7	3.7 ± 1.5	0.45
73	33.1 ± 46.2	4.5 ± 2.0	0.55
240	36.9 ± 41.7	5.4 ± 3.5	0.35

Up to 4h, the average size of the quasi-isotropic NPs slightly increases from 3.2 ± 1.6 to 3.5 ± 2.5 nm. During the first hours, these pristine NPs are maturing and their mean size increases. At 8 h, the 2D size plot shows that the points start to extend, suggesting that the anisotropic growth of the nanoparticles has begun. Correlation parameter (between length and width) ρ up to ca 0.80 is observed. In the following hours, the point cloud extends more and more up to 35 nm, while remaining quasi-parallel to the 2D size plot axis at ca 5-6 nm: the rods are becoming longer but their widths are somewhat maintained. ρ decreases and lower correlation between the length and the width is observed for these anisotropic NPs.

These results suggest that growth occurs mainly along the long axis of the NPs. A growth mechanism by oriented attachment could be here suggested.[24] [28] This hypothesis has been tested by considering two populations of NPs. Indeed, after four hours the point clouds are best fitted with two sub-populations: the first, N1, corresponds to the pristine isotropic ZnO NPs and the second, N2, corresponds to the growing nanorods. Results of the multivariate analysis considering these two clusters are listed Table 2. Note to mention that here the multivariate analysis can investigate: the classification, average size and percentage of different point groups, the correlation of two variables (length and width).

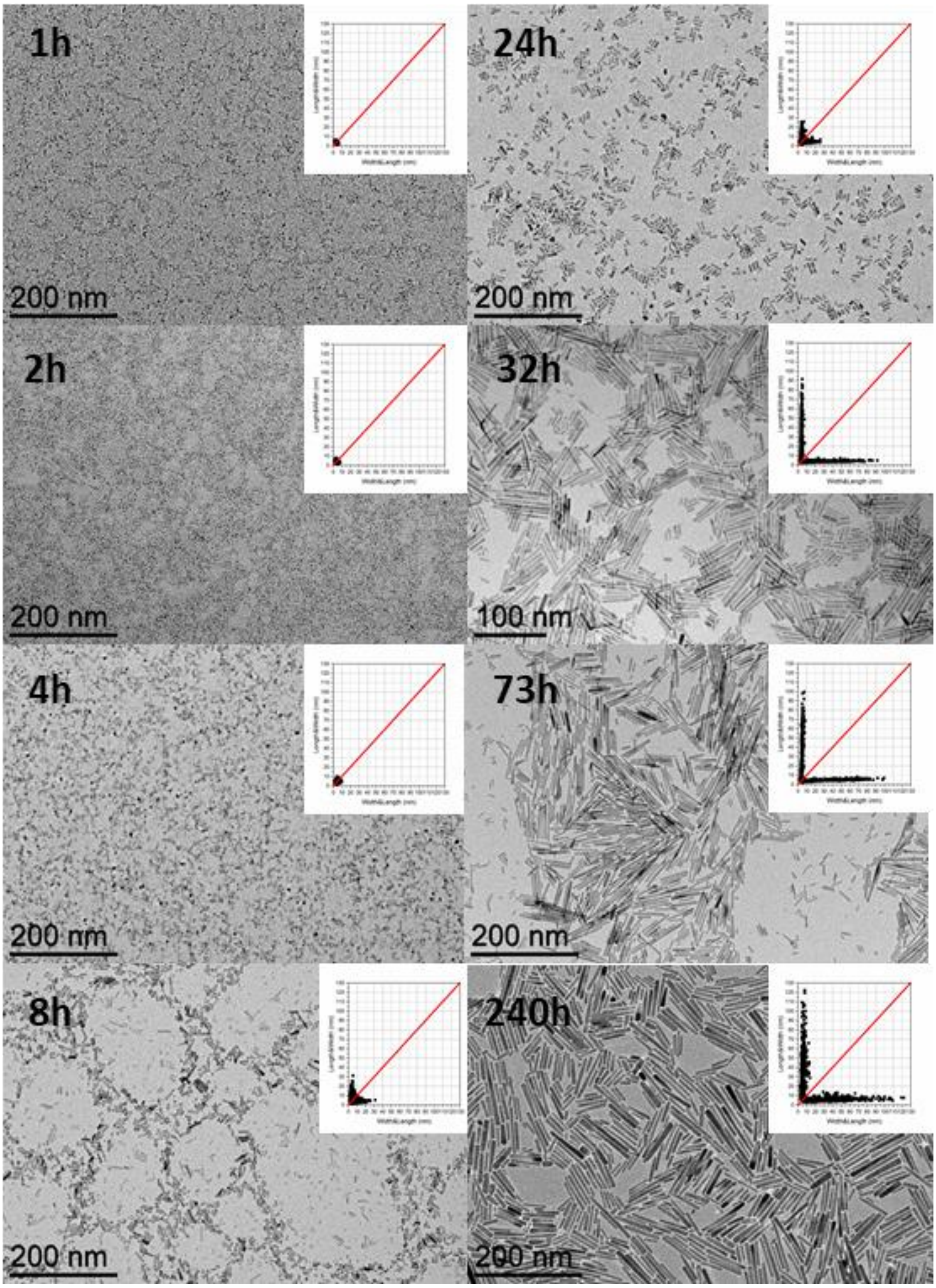

Figure 1. 2D size plots and TEM pictures of ZnO NPs versus hydrolysis time (from 1 to 240 hours). During the first hours, these pristine nanoparticles are maturing and their mean size increases.

Table 2. Multivariate analysis of the 2D plots corresponding to the TEM images of Figure 1 (ZnO NPs versus hydrolysis time from 1 to 240 hours) through a modified Rmixmod program[29] allowing access to the number and consequently the percent of

pristine NPs, N1, and anisotropically growing NPs, N2.

Hydrolysis time (hours)	Number of N1	Number of N2	Percent of N1 (%)	Percent of N2 (%)
1	2102	46	97.9	2.1
2	4509	173	96.3	3.7
4	1184	131	90	10
8	604	604	50	50
24	65	975	6.3	93.7
32	77	682	10.1	89.9
73	19	467	3.9	96.1
240	1	596	0.2	99.8

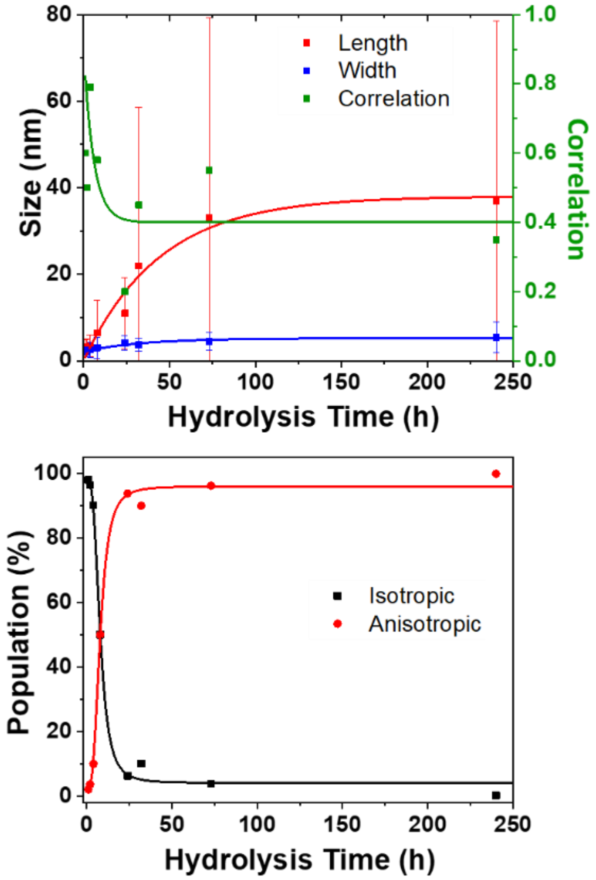

Figure 2. Mean length (red), mean width (blue) and corresponding correlation (green) obtained from a multivariate analysis (with a single Gaussian) of TEM data corresponding to the evolution of ZnO NPs average size versus hydrolysis time (from 1 to 240 hours, top) and percent of isotropic and anisotropic ZnO NPs issued from the

analysis of a modified Rmixmod software[29] (using two Gaussians one being isotropic, bottom).

Figure 2 shows the percent of isotropic and anisotropic NPs over the time of hydrolysis. Clearly, isotropic NPs decreases very quickly in favor of anisotropic ones. This indicates that after the nucleation step, the number of isotropic NPs is decreasing rapidly. Less than 10% of isotropic NPs are indeed observed after 24h. This result evidences that no nucleation occurs during the period of anisotropic growth. The nucleation and growth steps are uncorrelated and occurred sequentially in agreement with an oriented attachment process. In addition, after 24h, the overall length of the nanorods is still increasing, which strengthened the growth by oriented attachment. The isotropic NPs are consumed to the benefit of the length of the rods that increases concomitantly.[30]

Furthermore, C. Ribeiro *et al* suggest that growth of nanorods through an oriented attachments mechanism can be described as a “polymerization” reaction.[31] In that case and following various simplifications, the number of NPs, x_{max}, which have undergone a coalescence process leading to a nanorod should follow the equation:

$$x_{max} = -\frac{1}{\alpha . ln\left(\frac{8.\sqrt{2}.k_0.[S]_0.t}{1+\ 8.\sqrt{2}.k_0.[S]_0.t}\right)}$$

where t is the time of reaction, α is a constant parameter between 0 and 1, k_0 a kinetic constant and $[S]_0$ the initial concentration of active surfaces on the isotropic NPs (*i.e.* before coalescence). If one supposes that the length of the nanorod, L, is equal to:

$$L = x_{max}\ .W$$

where W is the width (i.e. the radius) of the isotropic particles, we can fit the variation of the mean length of the NPs versus time (see Figure 2). The value of the α parameter is then found at 0.06 and k_0. $[S]_0$ is estimated around 2.10^{-4} s^{-1}. This length *versus* time variation as well as the very weak growth of the nanorod diameters are therefore strong indications of an oriented attachment mechanism leading to the ZnO nanorods.

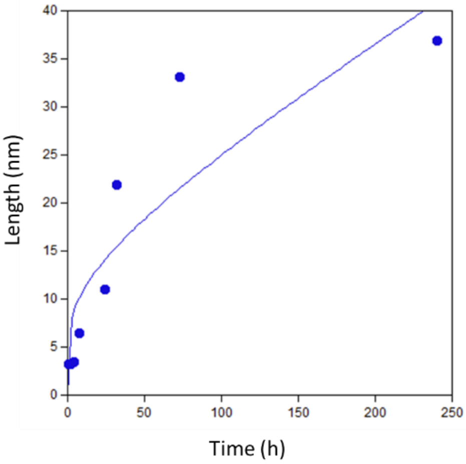

Figure 3. Fitting of the evolution of ZnO NPs average length versus hydrolysis time (from 1 to 240 hours).

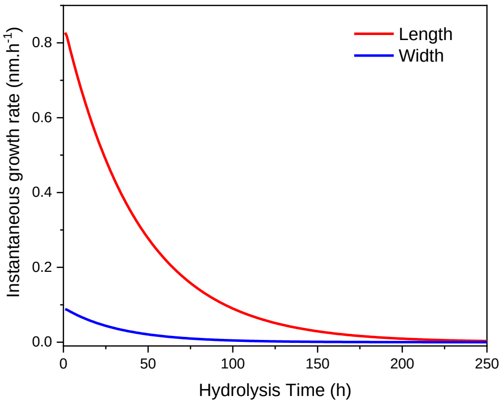

Figure 4: Instantaneous growth rate (nm.h^{-1}) as a function of time of ZnO NPs (from 1 to 240 hours, first derivative of Figure 2 –top).

Quantitative information can be extracted from the data depicted in Figure 1. In particular, the average growth rates along the two axes can be obtained by calculating the derivative at each point of the curves (Figure 4). An estimation based on a fitting of the experimental results using an exponential equation gives initial growth rates within the accuracy of the measurement in the range of 0.9 nm.h^{-1} for the length and one order of magnitude less (0.09 nm.h^{-1}) for the width. The growth in width is therefore already very slow after one hour while it continues to decrease significantly after 150 h for the length. It is however important to keep in mind that the instantaneous growth rate should be much higher in the early stages of the reaction as NPs of 3.2 ± 1.6 × 2.1 ± 1.1 nm are already observed after 1h. This apparent anisotropic shape corresponds in fact to an isotropic growth of the nanocrystals. Indeed, considering the intrinsic structural parameters of ZnO (c = 0.521 and a = b =0.325 nm), after one hour, the nanocrystals are composed of 6 unit-cells that have isotropically grown.

Whereas initial nucleation reaction is fast (after 1 minute solutions became luminescent which demonstrate the formation of ZnO NPs), growth mechanism seems to be stopped only after 5 days. This halt in the growth is certainly due to the partial carbonation of alkylamines into ammonium carbamates which, as we have recently shown,[30] leads to a complete modification of the organic stabilizing agents on the surface of the NPs. When NPs are only stabilized by alkylamines, these latter are localized only along the lateral faces leaving the basal faces accessible for growth by oriented attachment,[32]-[34] whereas in the presence of ammonium carbamates, these are located both on the lateral and the basal faces with a very strong affinity preventing the growth or attachment from continuing.[30]

2.3 Effect of the aging time of the reagent mixture before hydrolysis

Another parameter that has to be considered is the waiting time after mixing amine and zinc precursor reagents, before starting the hydrolysis step. Indeed, the viscosity of the solution increases slowly and, after 6 hours, the mixture behaves as a glass state gel.[35] This waiting time was then varied from 10 min up to 24h and the final shape of the obtained NPs observed systematically 3 days after starting the hydrolysis process (Figure 5). The 2D size plots (Figure 6) up to 4h of waiting time are very similar to each other: they show an extended point cloud almost parallel to the graph axis; corresponding to a mean width diameter of ca 4 ± 2 nm and a mean length of ca 10 ± 8 nm up to 20 nm (Table 3). As expected, the observed morphology are similar to the one obtained at the final stage (three days) in the part depicting the effect of hydrolysis time. When the mixing time reaches 5h, anisotropic growth is almost totally prevented: the average length and width over time of these particles remains roughly constant with a mean width of ca 2.1 ± 1.2 nm and a mean length of ca 3.4 ± 2.5 nm. As previously observed, the calculated correlation values are significantly lower for populations with high anisotropy (aging time < 6h): this could be related to the fact that the growth of the particles should occur essentially on their extremities in an oriented attachment mechanism.

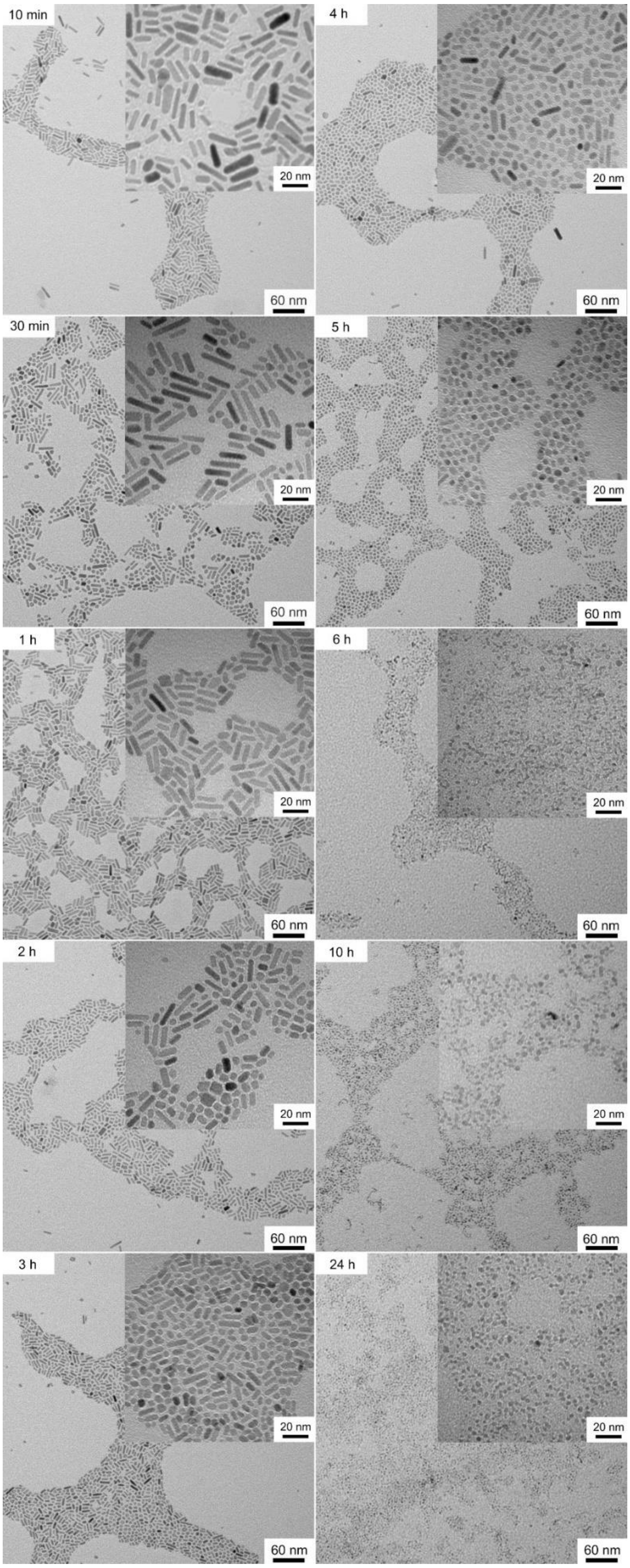

Figure 5. TEM images of the ZnO/2DDA NPs *versus* waiting time after mixing (or aging time before hydrolysis).

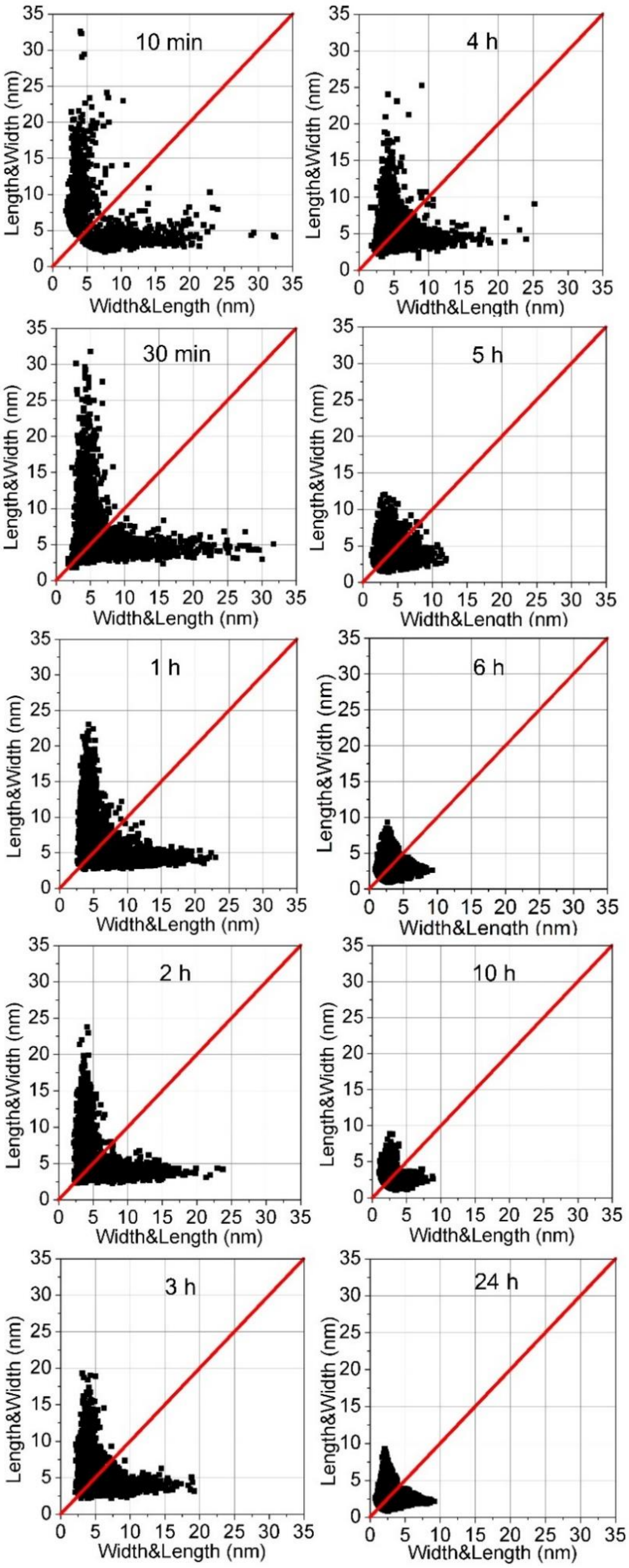

Figure 6**.** 2D size plots corresponding to the TEM images of Figure 5 (ZnO/2DDA NPs *versus* waiting time after mixing).

Table 3**.** Multivariate analysis of the 2D plots corresponding to the TEM images of the Figure 5 (ZnO/2DDA NPs *versus* waiting time after mixing) through Rmixmod program[26] [27] (the dispersion is given as twice the standard deviation obtained from calculations, and number of cluster was set to 1).

Aging time	Length (nm)	Width (nm)	correlation
10 minutes	9.3 ± 7.5	3.7 ± 1.8	0.40
30 minutes	8.6 ± 9.0	4.4 ± 1.9	0.13
1 hour	10.9 ± 7.3	4.4 ± 1.8	-0.02
2 hours	8.3 ± 6.7	3.8 ± 1.4	0.10
3 hours	7.7 ± 5.9	4.1 ± 1.6	0.02
4 hours	6.6 ± 5.4	4.2 ± 1.7	0.32
5 hours	5.1 ± 2.8	3.6 ± 1.7	0.41
6 hours	3.4 ± 2.6	2.1 ± 1.3	0.61
10 hours	3.4 ± 2.1	2.0 ± 1.0	0.40
24 hours	3.4 ± 2.7	2.1 ± 1.2	0.54

Again, the resulting point clouds were analyzed considering possible population mixing. The multivariate analysis leads to an optimal adjustment of the data set by considering, as before, two populations of particles: one isotropic and the second anisotropic, comprising N1 and N2 nanoparticles respectively, which are similar to the one obtained after three days in the previous synthesis (Figure 1). They show an extended point cloud almost parallel to the graph axis; corresponding to a mean diameter of ca 4 nm and a length up to 20 nm of the nanorods. The multivariate analysis of these graphs was conducted as described previously. Percent of N1 and N2 is shown in Figure 7. In this case, up to a mixing time of 4 hours, the values of N1 and N2 remain constant with a mean value of more than 95% for N2 (*i.e.* anisotropic NPs) and less than 5% for N1 (*i.e.* isotropic NPs). Then, the percentages are abruptly reversed for a waiting time of 5h. This reflects an abrupt transition from anisotropic NPs to isotropic ones. When the mixing time reaches 5h, anisotropic growth is totally prevented. These results should be compared with rheological measurements of the reaction medium over time, which make it possible to measure the variation of the viscosity of the medium (Figure 8). Between 0 and 5h, the values of G' and G" increase slowly and reach respectively 0.5 and 0.1 Pa, which indicates a liquid medium whose viscosity increases progressively. At 5h, G' and G" increase abruptly, and G’ becomes higher than G”, the medium becomes very viscous and reaches a semi-glassy state within a few minutes.[35]

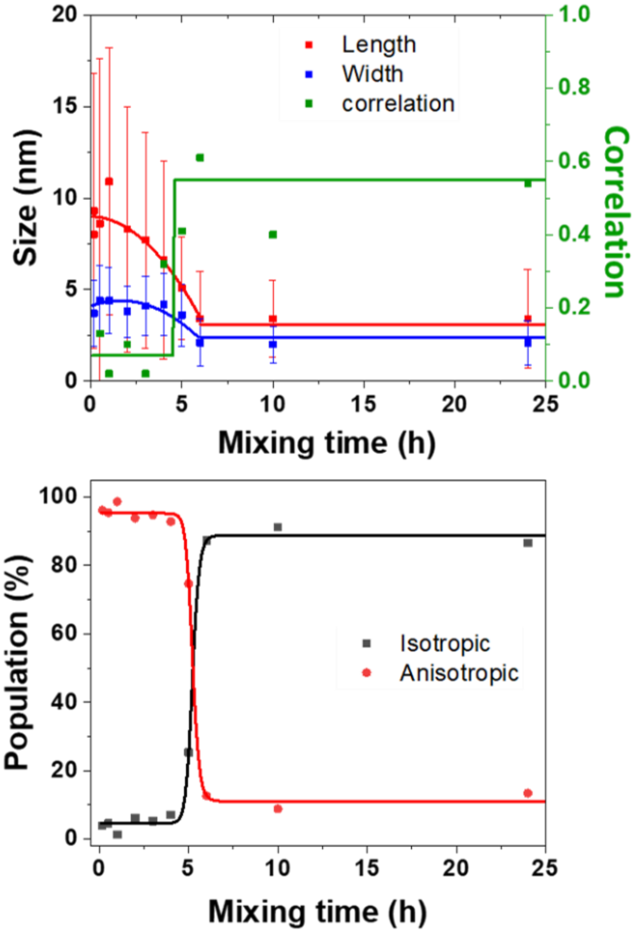

Figure 7. Mean length (red), mean width (blue) and corresponding correlation (green) obtained from a multivariate analysis (with a single Gaussian) of TEM data corresponding to the evolution of ZnO NPs average size versus the aging time of the reagent mixture before hydrolysis (from 1h to 24 hours, top) and percent of isotropic ZnO NPs (N1) and anisotropic ZnO NPs (N2) issued from the analysis of a modified Rmixmod software[29] (using two Gaussians one being isotropic, bottom)

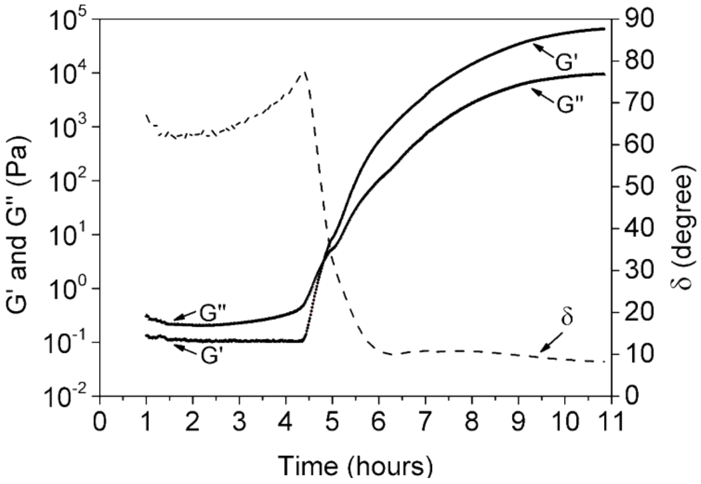

Figure 8. Time dependence of the elastic modulus G’, the viscous modulus G'' and the phase angle, δ, between the stress and strain measured under sinusoidal stress (frequency 1 Hz) for the $[Zn(Cy)_2]/2DDA$ mixture under nitrogen. The origin of the time

scale corresponds to the mixing process.[35]

Clearly, a correlation between viscosity of the medium and NPs shape exists. The multivariate analysis of the data quantitatively corroborates the abrupt transition from anisotropic to isotropic NPs with an average diameter almost constant and equal to 4 nm from 10 minutes to 5 hours that decreases to 2 nm after 5 hours and length (for which the uncertainties are large) of ca 10 nm that reaches 2 nm after 5h.

As suggested by C. Ribeiro et al., the kinetic related to an oriented attachment mechanism should consider the viscosity of the medium, η.[36] The diffusion coefficient of the NPs controlling collision process leading to contact and coalescence will decrease as 1/η with the viscosity as well as the kinetic constant associated to such process. Longer waiting time (higher than 4-5 hours) leads to very high viscosity, which should limit the diffusion speed and growth process of the NPs. This explains why shorter NPs are observed for such long waiting time.

2.4 Effect of the speeding rate of water addition and the amount of water

The effects of hydrolysis time and mixing time illustrate the importance of the kinetic parameters of the reaction. The question then arises of the speed of arrival of water in the medium to lead by hydrolysis of $[Zn(Cy)_2]$ the formation of ZnO NPs. To study this effect, water feeding rate was controlled by using PTFE tubes of different lengths as depicted schematically in Figure 9.

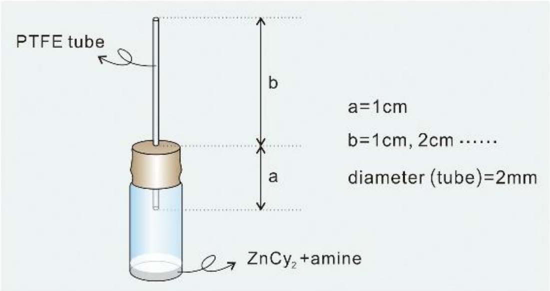

Figure 9. Schematic illustration for the preparation of ZnO NPs depending on different length of tubes for hydrolysis (vial dimension: height: 3 cm, diameter: 1.5 cm). Water is coming from the top of the tube.

Indeed, following the Fick's law, the gaseous water flow, J, from the atmosphere to the vial containing the reactants should be:

$$J = - D\, dC/dx,$$

where D is the diffusion coefficient of gaseous water in air (ca 0.25 cm^2/s),[37] C the concentration of gaseous water along the position x in the tube. The outside concentration of gaseous water, C_{out}, can be roughly estimated by the ideal gas law:

$$C_{out} = RH_{mean}.\ P_s/RT$$

where RH_{mean} is the mean value of the relative humidity of the atmosphere (ca 70%)[38] and P_s the saturated pressure of water at the average temperature T (20°C), leading to C_{out} close to 7.10^{-4} $mol.L^{-1}$. The inner concentration C_{in} should be close to zero because of the (fast) hydrolysis reaction. Therefore, the flow could be estimated to:

$$J = D.C_{out} / L,$$

where L is the total length of the PTFE tube (i.e. a + b in Figure 9) and the rate of water addition is J.S where S in the section of the PTFE tube, i.e. $2.2.10^{-8}$ $mol.s^{-1}$ /L(in cm) for a tube diameter of $\Phi = 2$ mm. Increasing the tube length from 2 cm to 20 cm should therefore divide the water flow rate by a factor of 10 to ca 10^{-9} $mol.s^{-1}$. With such a rudimentary theoretical rate, 70 hours (*i.e.* roughly 3 days) are needed to hydrolyze all the zinc precursor.

In brief, the water addition speeding is varied from 10^{-7} down to 10^{-9} $mol.s^{-1}$. To avoid at maximum the observed gelation process[35], hydrolysis was initiated, in all following experiments, 10 minutes after the mixing process.

As shown in Figure 10, anisotropic NPs with mean length of 16.5 ± 11.6 nm could be prepared if the vial without stopper was used. Interestingly, the length of the NPs decreased if, for a given diameter equal to 2 mm, longer tubes were used (i.e. lowering the feeding rate). For the longest 20 cm tube quasi-isotropic 1.7 ± 1.1 nm ZnO NPs were thus obtained with, as expected for isotropic ZnO NPs, higher correlation values. Decreasing the feeding rate of water favored the gelation process to occur, and prevent the formation of anisotropic NPs. As expected, the same tendency is observed when the diameter of the PTFE tube was increased from 2 mm to 4 mm. This increase in diameter results in an increase of the water flow rate by a factor of 4 and therefore longer NPs were obtained with larger tube for a given length. Moreover, as expected from the fact that the water flow should be inversely proportional to the tube length (see supporting information), anisotropic NPs with similar size were obtained when comparing tubes with respective lengths equal to 1 and 4 cm and diameters equal to 2 and 4 mm, respectively. Thus, as illustrated in Figure 11 size was found to be proportional to Φ^2/L (with Φ and L the diameter and length of the tubes, respectively), values which is directly related to the water feeding rate. In conclusion, increasing the amount of water reaching per unit of time the reactive medium (by using larger and/or longer tubes) enables the growing process to occur more rapidly than gelation process and promotes the formation of anisotropic nanoparticles.

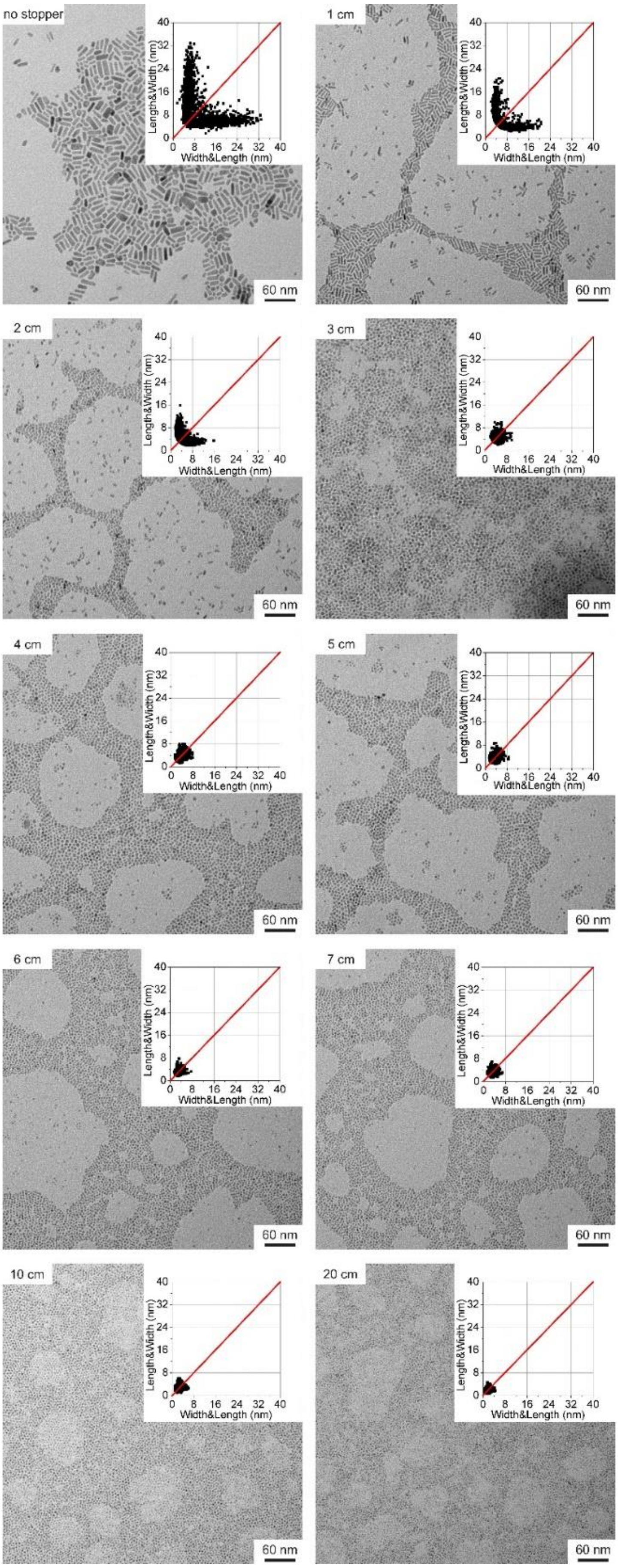
no stopper
1 cm
2 cm
3 cm
4 cm
5 cm
6 cm
7 cm
10 cm
20 cm
Length&Width (nm)
Width&Length (nm)
0
8
16
24
32
40
60 nm

Figure 10. TEM images (and corresponding 2D plots) of synthesized ZnO NPs for various PTFE external tube length (L in cm).

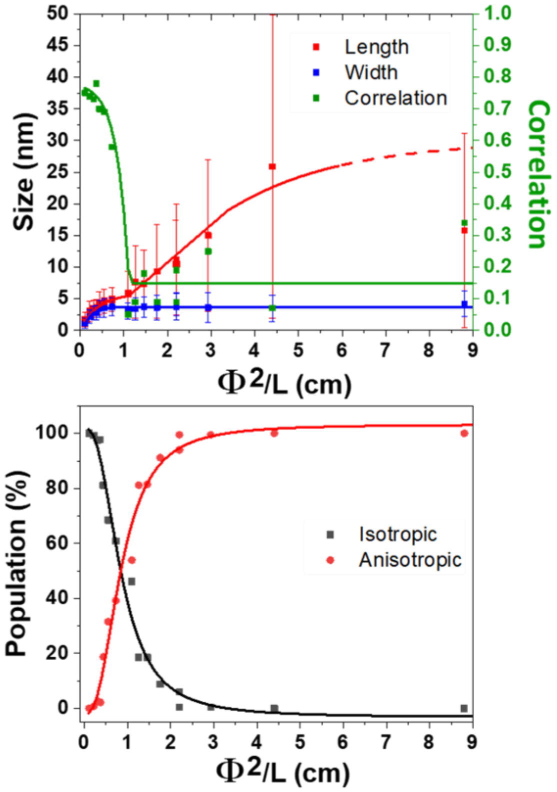

Figure 11. Influence of water flow rate with is proportional to Φ^2/L (with Φ and L the diameter and length of the tubes respectively) on the morphology of obtained NPs, the results are issued from a multivariate analysis (with a single Gaussian). The red, blue and green line depicts the mean width, mean length and corresponding correlation respectively. The lines are just guided for the eyes (top). Percent of isotropic ZnO NPs (N1) and anisotropic ZnO NPs (N2) issued from the analysis of a modified Rmixmod software[29] (using two Gaussians one being isotropic, bottom).

Apart from the kinetic of water feeding, the amount of water introduced in the vessel has been varied from 2 equiv. up to 100 equiv. relatively to zinc precursor as depicted in Figure 12.

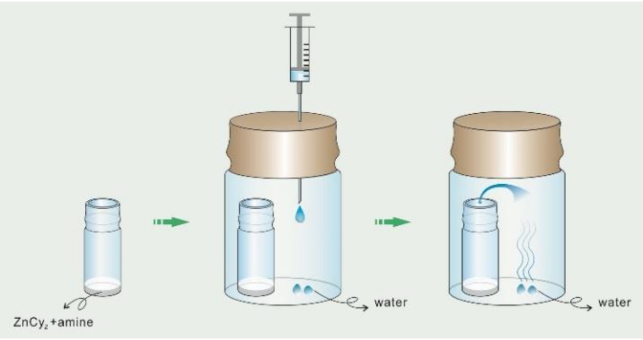

Figure 12. Schematic illustration for the preparation of ZnO NPs depending on different equivalent of water.

Results are reported in Figure 13. Increasing the amount of water leads to a decrease of the NPs aspect ratio. In the case of NPs stabilized by 2 equiv. DDA and with 2 equiv. of water, the 2D size plots reveal a distribution of size where the average width and length are equal to 4.8 ± 1.5 nm and 53.8 ± 41.2 nm, respectively. As the amount of water increases, the 2D size plot exhibits less and less extended length range, the points cloud is more and more focused around the median line which is characteristic of a decrease of the aspect ratio. Especially for more than 8 equiv. of water, the width of the NPs increases from 5 nm up to 7 nm. Interestingly, the number of isotropic NPs is increasing as the amount of water increases (Table 4 and Figure 13). This result suggests that large amount of water favors multi-nucleation.

Table 4: Multivariate analysis of the 2D plots corresponding to the TEM images of Figure 13 (ZnO NPs prepared in the presence of 2 eq. DDA for different amounts of water) through a modified Rmixmod program[29] allowing access to the number and consequently the percent of pristine NPs, N1, and anisotropicaly growing NPs, N2.

Equivalent of H_2O	Number of N1	Number of N2	Percent of N1 (%)	Percent of N2 (%)
2	0	300	0	100
4	0	301	0	100
8	2	298	0.6	99.4
12	2	302	0.6	99.4
20	14	286	4.7	95.3
40	19	281	6.3	93.7
70	17	284	5.6	94.4
100	32	268	10.6	89.4

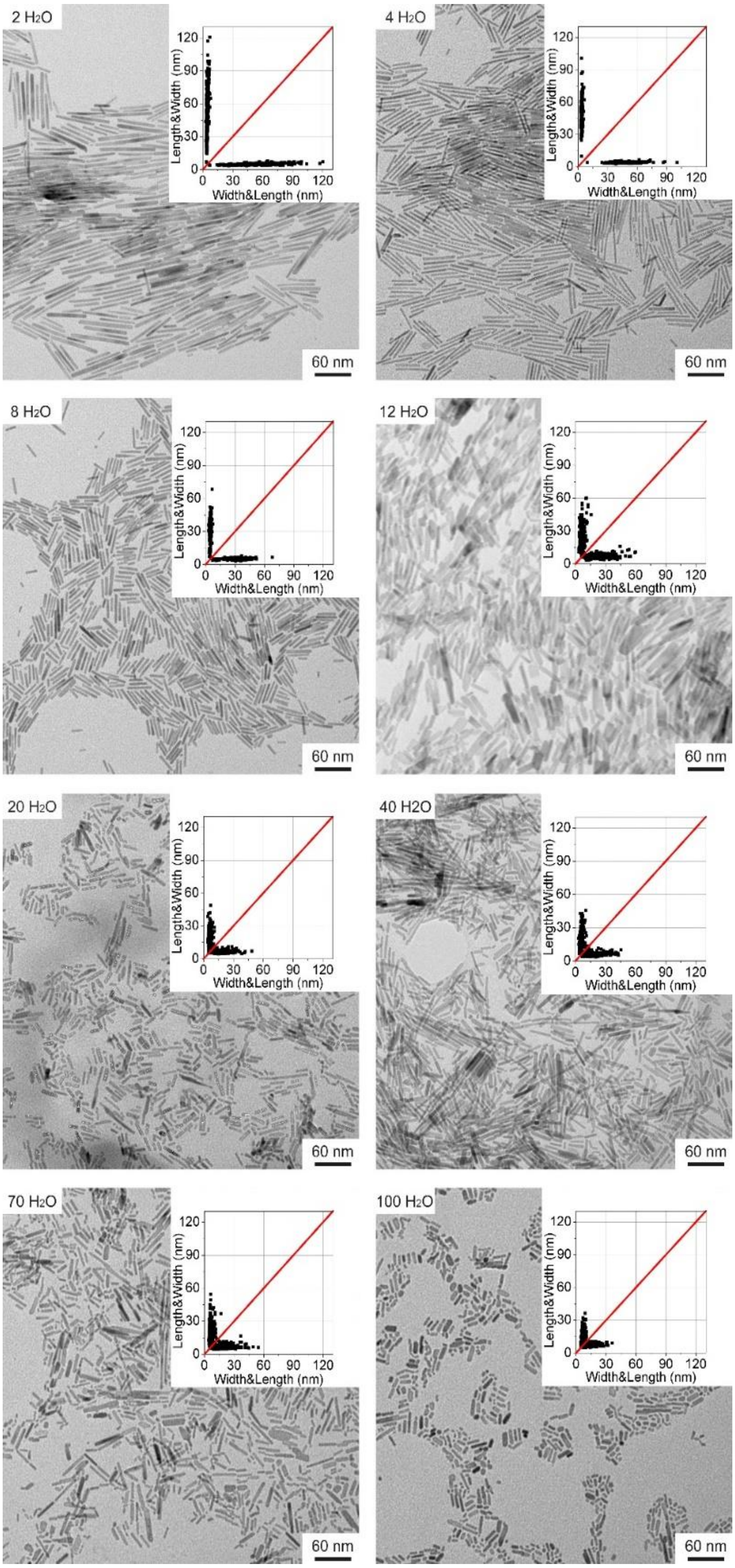

Figure13. TEM pictures and 2D size plots of ZnO NPs prepared in the presence of 2

eq. DDA for different amounts of water.

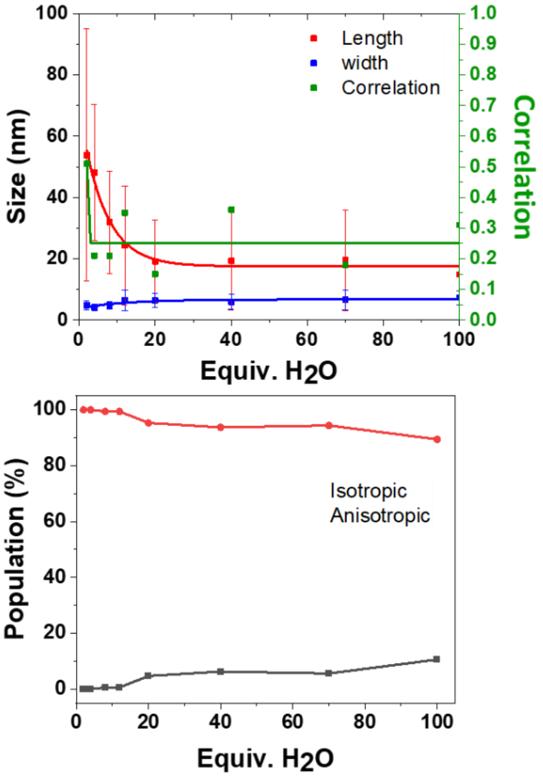

Figure 14. Results issued from a multivariate analysis (with a single Gaussian). The red, blue and green line depicts the mean width, mean length and corresponding correlation respectively. The lines are just guided for the eyes.

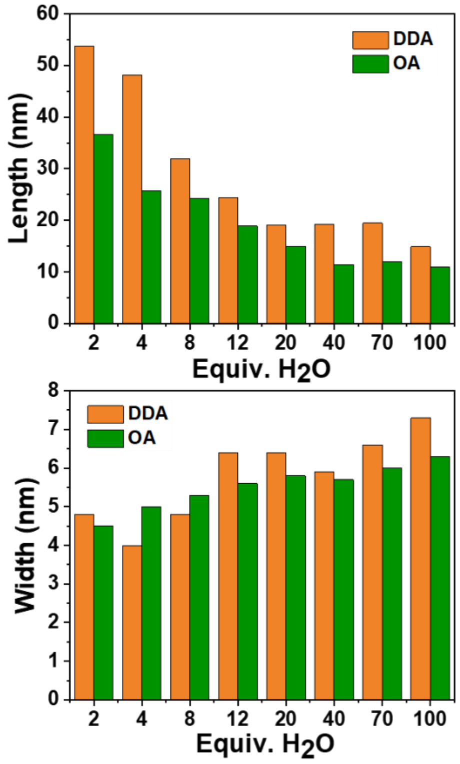

Figure 15. Variation in length (left) and width (right) of ZnO nanorods synthesized in

the presence of DDA or OA as a function of the number of water equivalents to the Zn precursor.

As the quantity of zinc precursor is the same for all the experiments (0.25 mmol), multi-nucleation competes with growth and consequently, aspect ratio decreases. Figure 14 shows the evolution of the length, width and correlation as a function of the water amount. Correlation between length and width remains roughly constant whatever the amount of added water. As previously discussed, an oriented attachment mechanism from isotropic NPs formed during nucleation step can easily explain this observation.

2.5 Effect of the length of the fatty amine

The structure of the amine can also influence the morphology of the particles obtained. In order to measure this impact, an additional series of experiments was performed with octylamine, OA (C_8H_{17}-NH_2) instead of DDA with varying amounts of water. The analysis results for case of OA are shown in Experimental Part.

Comparison of the results are shown in Figure 15. As observed with DDA, increasing the final amount of water favors the formation of shorter and slightly larger nanorods with lower aspect ratio. In addition, for an equivalent quantity of water, while the width of the nanorods is similar regardless of the ligand, the aspect ratio is much higher when DDA is used instead of OA. The length of the NPs ranges from 5 to 65 and 15 to 100 nm for OA and DDA, respectively (For the case of OA, see Table 1 in Experimental Part). Another important difference is the absence of isotropic NPs for 2 and 4 equiv. of water in the presence of DDA. The effect of alkyl chain can be related to the specific organization of the reaction medium before and during hydrolysis process. This organization may be either due to the interaction of zinc ions with primary amine[35] and/or to the formation of well-organized liquid crystalline phases for the obtained hybrid materials.[25] This organization is prone to modify the rheological behavior of reactive medium and might be responsible for the differences observed between the different amine in the frame of oriented attachment mechanism.

2.6 Conclusions

In this chapter, we demonstrate how simple analytical tools based on statistical analysis can help us to decipher the anisotropic growth of NPs and to better understand and control the parameters governing this anisotropic growth. A fine comparison of the synthetic protocol of the role of the hydrolysis rate, the mixing time before hydrolysis, the length of the ligand aliphatic chain, and the amount of water allowed to evidence the relative importance of those experimental parameters on the anisotropic growth of the ZnO NPs. All the data suggest that the growth mechanism occurred through an oriented attachment process that is eventually hampered by gelation process induced by interaction of zinc precursor or ZnO NPs with amine ligands. These findings shed a light on the relative importance of experimental parameters that rule the growing of nano-objects and as such are crucial to identify, study, and control for design progress in nanoscience. One last parameter was not yet analyzed: the influence of the type of amine (primary, secondary or tertiary) for a constant alkyl tail. This is the main objective of the following chapter.

References

[1] G. Schmid, “Nanoparticles: From Theory to Application”, Wiley VCH, Weinheim, **2004**.

[2] X. Liang, S. Bai, X. Wang, X. Dai, F. Gao, B. Sun, Z. Ning, Z. Ya and Y. Jin, “Colloidal metal oxide nanocrystals as charge transporting layers for solution-processed light-emitting diodes and solar cells”, *Chem. Soc. Rev.*, **2017**, *46*, 1730-1759.

[3] T. Song, F. Gao, S. Guo, Y. Zhang, S. Li, H. You, Y. Du, “A review of the role and mechanism of surfactants in the morphology control of metal nanoparticles”, *Nanoscale*, **2021**, *13*, 3895.

[4] M. Zhou, C. Li, J. Fang, “Noble-metal based random alloy and intermetallic nanocrystals: Syntheses and applications”, *Chem. Rev.* **2021**, *121*, 736−795.

[5] C. Gao, F. Lyu, Y. Yin, “Encapsulated metal nanoparticles for catalysis”, *Chem. Rev.*, **2021**, *121*, 834−881.

[6] X.-M. Liu, X. Cui, K. Dastafkan, H.-F. Wang, C. Tangz, C. Zhao, A. Chen, C. He, M. Han, Q. Zhang, “Recent advances in spinel-type electrocatalysts for bifunctional oxygen reduction and oxygen evolution reactions”, *J. Energy Chem.*, **2021**, *53*, 290–302.

[7] X.-L. Shi, J. Zou, Z.-G. Chen, “Advanced thermoelectric design: from materials and structures to devices”, *Chem. Rev.* **2020**, *120*, 7399−7515.

[8] Z. Xie, Y. Duo, Z. Lin, T. Fan, C. Xing, L. Yu, R. Wang, M. Qiu, Y. Zhang, Y. Zhao, X. Yan, H. Zhang, “The rise of 2D photothermal materials beyond graphene for clean water production”, *Adv. Sci.* **2020**, *7*, 1902236.

[9] L. Cheng, X. Wang, F. Gong, T. Liu, Z. Liu, “2D Nanomaterials for Cancer Theranostic Applications”, *Adv. Mater.* **2020**, *32*, 1902333.

[10] J. G. DiStefano, A. A. Murthy, S. Hao, R. dos Reis, C. Wolvertona, V. P. Dravid, “Topology of transition metal dichalcogenides: the case of the core–shell architecture”, *Nanoscale*, **2020**, *12*, 23897.

[11] S. R. Alvarado, Y. J. Guo, T. P. A. Ruberu, E. Tavasoli and J. Vela, “Inorganic chemistry solutions to semiconductor nanocrystal problems”, *Coord. Chem. Rev.*, **2014**, *263-264*, 182-196.

[12] G. D. Li and Z. Y. Tang, “Noble metal nanoparticle @ metal oxide core/yolk–shell nanostructures as catalysts: recent progress and perspective”, *Nanoscale*, **2014**, *6*, 3995-4011.

[13] H. J. Yang, S. Y. He, H. L. Chen and H. Y. Tuan, “Monodisperse copper nanocubes: Synthesis, self-assembly, and large-area dense-packed films”, *Chem. Mater.*, **2014**, *26*, 1785-1793.

[14] M. W. Rotz, K. S. B. Culver, G. Parigi, K. W. MacRenaris, C. Luchinat, T. W. Odom and T. J. Meade, “High relaxivity Gd (III)–DNA gold nanostars: investigation of shape effects on proton relaxation”, *ACS Nano*, **2015**, *9*, 3385-3396.

[15] J. Jonca, A. Ryzhikov, M. L. Kahn, K. Fajerwerg, A. Chapelle, P. Menini and P. Fau, “SnO_2" Russian Doll" octahedra prepared by metalorganic synthesis: A new structure for sub-ppm CO detection”, *Chem. Eur. J.*, **2016**, *22*, 10127-10135.

[16] K. Thorkelsson, P. Bai and T. Xu, “Self-assembly and applications of anisotropic nanomaterials: A review”, *Nano Today*, **2015**, *10*, 48-66.

[17] G. L. Drisko, C. Gatel, P.-F. Fazzini, A. Ibarra, S. Mourdikoudis, K. Fajerwerg, P. Fau and M. L. Kahn, “Air-stable anisotropic monocrystalline nickel nanowires characterized using electron holography”, *Nano Letters*, **2018**, *18*, 1733−1738.

[18] P. Melinon, S. Begin-Colin, J. L. Duvail, F. Gauffre, N. H. Boime, G. Ledoux, J. Plain, P. Reiss, F. Silly, B. Warot-Fonrose, “Engineered inorganic core/shell nanoparticles”, *Phys. Rep.-Rev. Sec. Phys. Lett.*, **2014**, *543*, 163 197.

[19] S. Mourdikoudis, V. Colliere, C. Amiens, P. Fau and M. L. Kahn, “Metal–Organic Pathways for Anisotropic Growth of a Highly Symmetrical Crystal Structure: Example of the fcc Ni”, *Langmuir*, **2013**, *29*, 13491-13501.

[20] Y. Xia, Y. Xiong, B. Lim and S. E. Skrabalak, “Shape-controlled synthesis of metal nanocrystals: simple chemistry meets complex physics?”, *Angew. Chem. Int. Ed.*, **2009**, *48*, 60-103.

[21] Y. Xia, X. Xia and H. C. Peng, “Shape-controlled synthesis of colloidal metal nanocrystals: thermodynamic versus kinetic products”, *J. Am. Chem. Soc.*, **2015**, *137*, 7947-7966.

[22] M. Monge, M. L. Kahn, A. Maisonnat and B. Chaudret, “Room-Temperature Organometallic Synthesis of Soluble and Crystalline ZnO Nanoparticles of Controlled Size and Shape”, *Angew. Chem. Int. Ed.*, **2003**, *42*, 5321-5324.

[23] M. L. Kahn, A. Glaria, C. Pages, M. Monge, L. Saint Macary, A. Maisonnat and B. Chaudret, “Organometallic chemistry: an alternative approach towards metal oxide nanoparticles”, *J. Mater. Chem.*, **2009**, *19*, 4044-4060.

[24] Z. Zhao, Z. Zheng, C. Roux, C. Delmas, J. D. Marty, M. L. Kahn and C. Mingotaud, “Importance of the Correlation between Width and Length in the Shape Analysis of Nanorods: Use of a 2D Size Plot To Probe Such a Correlation”, *Chem. Eur. J.*, **2016**, *22*, 12424-12429.

[25] Z. Zheng, R. Butynska, C. Valverde Serrano, J.-D. Marty, C. Mingotaud and M. L. Kahn, “One step synthesis of hybrid liquid-crystal ZnO nanoparticles: control of the nanoparticle anisotropy by temperature”, *Chem. Eur. J.*, **2016**, *22*, 15614-15618.

[26] R. Lebret, S. Iovleff, F. Langrognet, C. Biernacki, G. Celeux, G. Govaert, “Rmixmod: The R package of the model-based unsupervised, supervised, and semi-supervised classification Mixmod library”, Journal of Statistical Software, **2015**, *67*, 1-29.

[27] R. Lebret, S. Iovleff, F. Langrognet, M. R. Lebret, L. Rcpp, “Package ‘Rmixmod’ ”, **2015**.

[28] X. Xue, R. L. Penn, E. R. Leite, F. Huang and Z. Lin, “Crystal growth by oriented attachment: kinetic models and control factors”, *CrystEngComm*, **2014**, *16*, 1419-1429.

[29] Modified mixmod software:

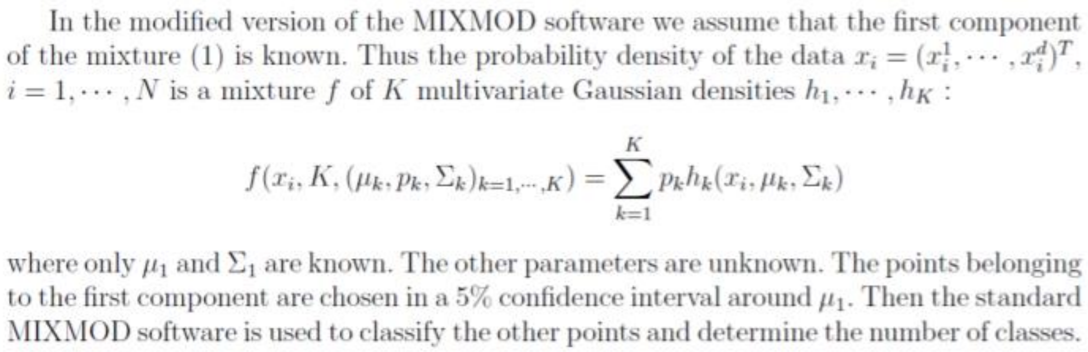

In the modified version of the MIXMOD software we assume that the first component of the mixture (1) is known. Thus the probability density of the data $x_i = (x_i^1, \cdots, x_i^d)^T$, $i = 1, \cdots, N$ is a mixture f of K multivariate Gaussian densities $h_1, \cdots, h_K$:

$$f(x_i, K, (\mu_k, p_k, \Sigma_k)_{k=1,\cdots,K}) = \sum_{k=1}^{K} p_k h_k(x_i, \mu_k, \Sigma_k)$$

where only μ_1 and Σ_1 are known. The other parameters are unknown. The points belonging to the first component are chosen in a 5% confidence interval around μ_1. Then the standard MIXMOD software is used to classify the other points and determine the number of classes.

[30] G. Spataro, Y. Champouret, Y. Coppel and M. L. Kahn, “Prominence of the Instability of a Stabilizing Agent in the Changes in Physical State of a Hybrid Nanomaterial”, *Chem. Phys. Chem.*, **2020**, *21*, 2454-2459.

[31] C. Ribeiro, E. J. H. Lee, E. Longo and E. R. Leite, “Oriented attachment mechanism in anisotropic nanocrystals: A “polymerization” approach”, *ChemPhysChem*, **2006**, *7*, 664–670.

[32] G. Spataro, Y. Champouret, P. Florian, Y. Coppel and M. L. Kahn, “Multinuclear solid-state NMR study: a powerful tool for understanding the structure of ZnO hybrid nanoparticles”, *Phys. Chem. Chem. Phys.*, **2018**, *20*, 12413 – 12421.

[33] M. L. Kahn, T. Cardinal, B. Bousquet, M. Monge, V. Jubera and B. Chaudret, “Optical properties of zinc oxide nanoparticles and nanorods synthesized using an organometallic method”, *Chem. Phys. Chem.*, **2006**, *7*, 2392-2397.

[34] Y. Coppel, G. Spataro, C. Pages, B. Chaudret, A. Maisonnat and M. L. Kahn, “Full characterization of colloidal solutions of long-alkyl-chain-amine-stabilized ZnO nanoparticles by NMR spectroscopy: surface state, equilibria, and affinity”, *Chem. Eur. J.*, **2012**, *18*, 5384-5393.

[35] Z. Zhao, Y. Coppel, J. Fitremann, P. Fau, C. Roux, C. Lepetit, P. Lecante, J.-D. Marty, C. Mingotaud, M. L. Kahn, “Mixing Time between Organometallic Precursor and Ligand: A Key Parameter Controlling ZnO Nanoparticle Size and Shape and Processable Hybrid Materials”, *Chem. Mater.*, **2018**, *30*, 8959-8967.

[36] C. Ribeiro, E. J. H. Lee, E. Longo and E. R. Leite, “A kinetic model to describe nanocrystal growth by the oriented attachment mechanism”, *ChemPhysChem*, **2005**, *6*, 690–696.

[37] J. Rumble, *CRC Handbook of Chemistry and Physics, 100th Edition*, 2019.

[38] https://www.wofrance.fr/weather/maps/city.

Chapter III. Anisotropic growth of ZnO nanoparticles driven by the structure of amine surfactants: the role of surface dynamics in nanocrystal growth

3.1 Introduction

As discussed in the previous chapter, in the organometallic pathway leading to ZnO NPs, the role of the general structure of the amine and especially the number of substituents around the nitrogen atom –i.e. primary vs secondary or tertiary amine– was not investigated in details. In the following paragraphs, the first comparative study establishing the different roles played by primary, secondary and tertiary amine surfactants is therefore described. These amines of identical aliphatic chain-length were mixed with the zinc precursor to get ZnO NCs of very different morphology: either 2D defined nanorods, or isotropic spherical nanoparticles, or shapely ill-defined aggregates. In the course of nanoparticles formation we analyzed at each step of the synthesis both experimentally by multinuclear NMR (^{1}H, ^{13}C, ^{17}O) and theoretically by DFT modeling the role of the amine, including pertinent surface dynamics.

3.2 Size and morphologies depending on the amine structures

We prepared ZnO NPs following the usual method based on the controlled hydrolysis of the dicyclohexyl zinc compound, [Zn(Cy)$_2$], in the presence of the amine. Classically, the precursor and the surfactants are mixed in a vial and two equivalents of water are added in a homemade reactor allowing water vapor to diffuse into the reaction medium (see experimental section for details). Figure 1 shows the TEM images of the ZnO NPs obtained following this procedure when dodecylamine (C_{12}-NH_2), *N*-methyldodecylamine (C_{12}-$NH(CH_3)$), or *N,N*-dimethyldodecylamine, (C_{12}-$N(CH_3)_2$) are used as surfactant.

Clearly, the morphology specifically depends on the number of substituents on the amine nitrogen. Nanorods with a diameter of 5.0 ± 0.7 nm and a length of 16 ± 7 nm are obtained when a primary amine is used, while isotropic NCs of 7.3 ± 1.1 nm and aggregates are obtained for secondary and tertiary amines, respectively (see Table 1 in the Experimental Part). These ZnO nanoparticles obtained adopt a hexagonal structure as evidenced by PXRD (see Figure 1 and Table 2 in the Experimental Part). All the TEM pictures, we analyzed through the 2D size plot which enables to extract information on the correlation between widths and lengths of anisotropic objects.[1] As seen in Figure 1, for primary amine, the length is not strongly correlated to the diameter of the NPs suggesting that the growth along the long axis of the nanorod is more or less independent of the diameter increase. On the contrary, for secondary amine, the 2D plot shows a cloud of points aligned along the diagonal as expected from isotropic or poorly anisotropic NPs.

To rationalize these results, we analyzed the role of the amine at all stages of NC synthesis. In the following, the formation of the 1:1 adduct between the zinc precursor and the amine is first described. Then, the composition of the reaction medium as a function of time is characterized and the formation of amido complexes is shown for primary and secondary amines. Finally, the interaction of the different amines with the surface of the NPs is systematically reported.

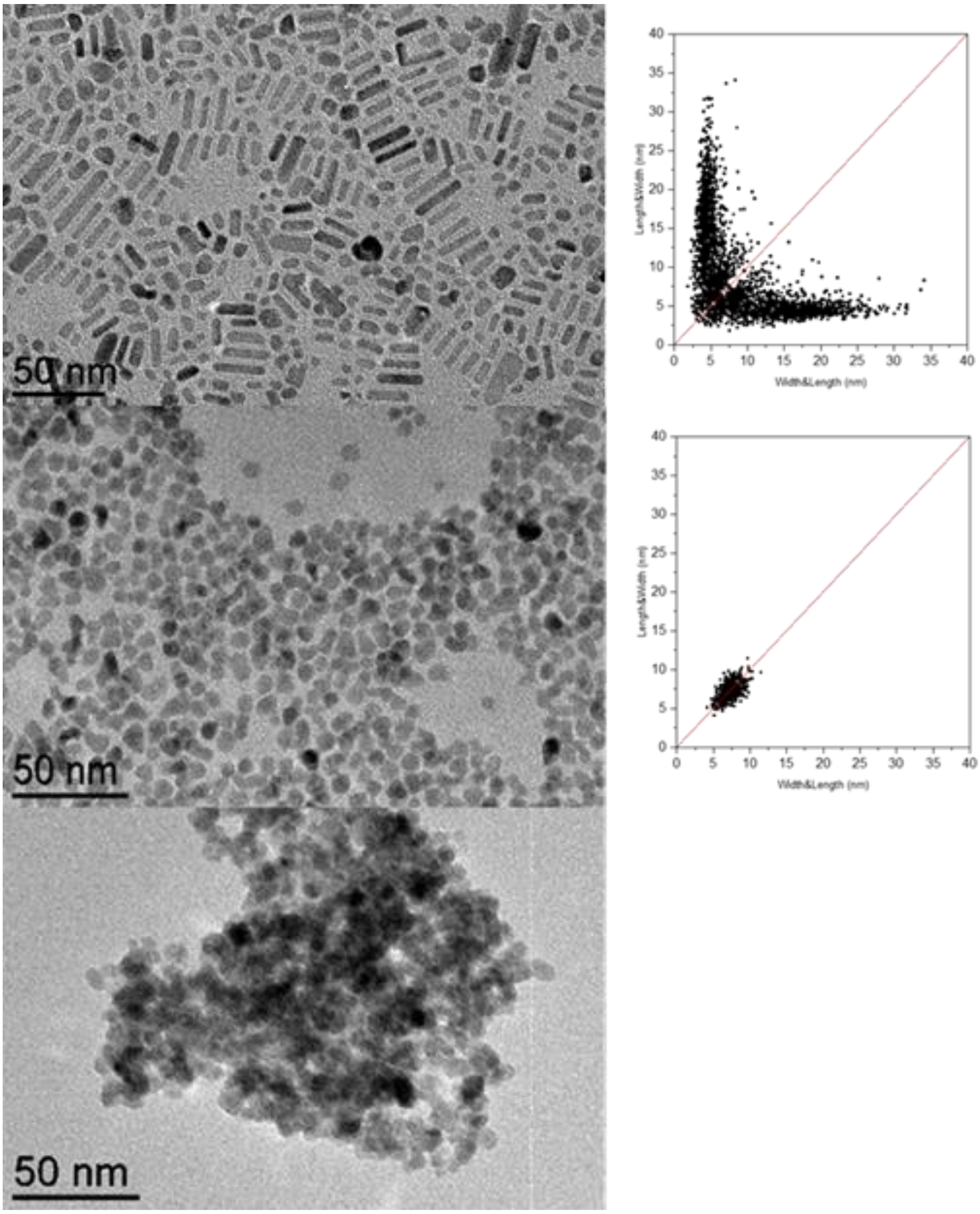

Figure 1**.** TEM images and associated 2D size plots[1] of the ZnO NCs obtained when dodecylamine (C_{12}-NH_2) (top), *N*-methyldodecylamine (C_{12}-$NH(CH_3)$) (middle), or *N,N*-dimethyldodecylamine, (C_{12}-$N(CH_3)_2$) (bottom) are used as stabilizing agent.

3.3 Adduct formation

Regardless of the alkylamine, mixing of the surfactant and the zinc precursor leads to the formation of a 1:1 adduct as evidenced notably through the shifts of the ^{1}H NMR signals for the aliphatic chain (Figures 2-4) and the characteristic signals of these spectra are listed in the following Table 1.

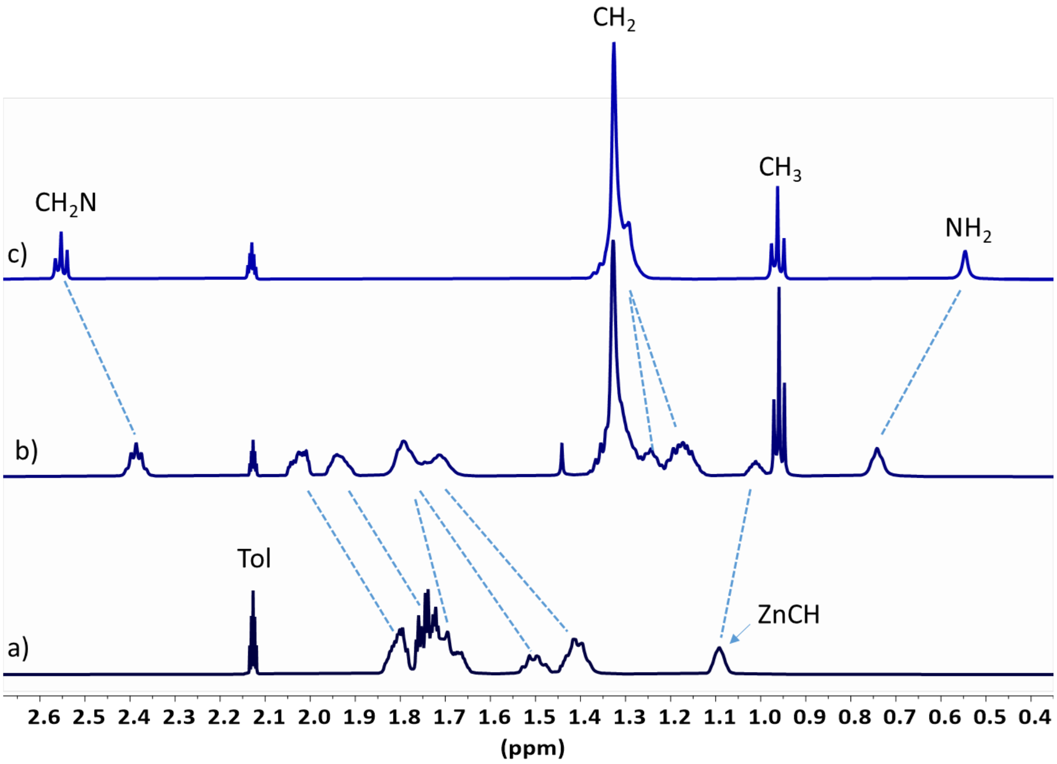

Figure 2. ^{1}H NMR spectra (298 K, toluene-d^8) of [Zn(Cy)$_2$] (a), of [Zn(Cy)$_2$] with 2 eq. of C$_{12}$-NH$_2$ after 1 h of mixing (b) and of C$_{12}$-NH$_2$ (c).

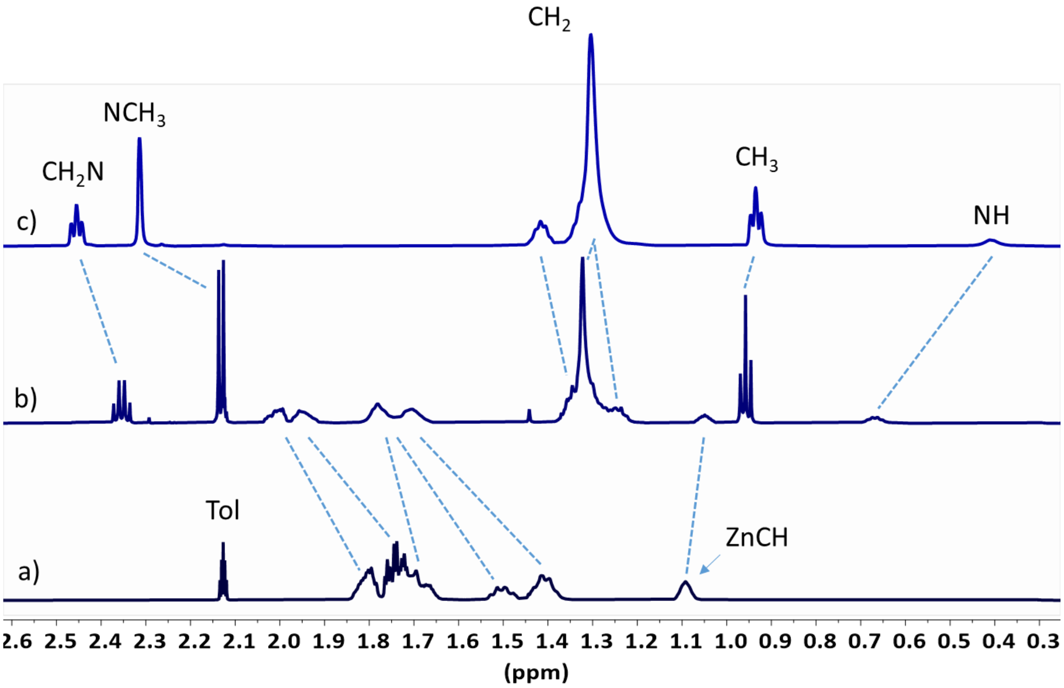

Figure 3. ^{1}H NMR spectra (298 K, toluene-d^8) of [Zn(Cy)$_2$] (a), of [ZnCy$_2$] with 2 eq. of C$_{12}$-NH(CH$_3$) after 1h of mixing (b) and of C$_{12}$-NH(CH$_3$) (c).

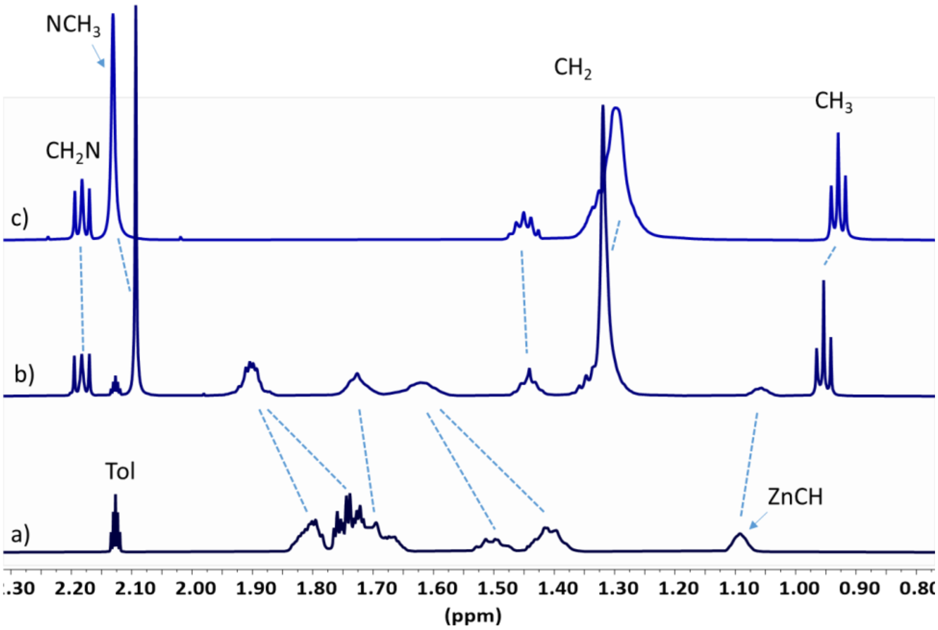

Figure 4. ^{1}H NMR spectra (298 K, toluene-d^8) of [Zn(Cy)$_2$] (a), of [Zn(Cy)$_2$] with 2 eq. of C_{12}-N(CH$_3$)$_2$ after 1h of mixing (b) and of C_{12}-N(CH$_3$)$_2$ (c).

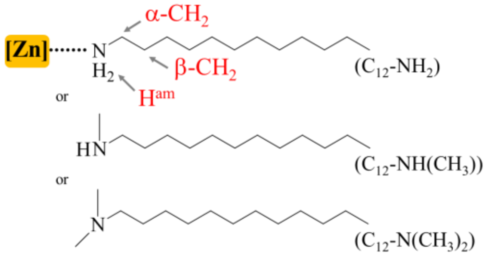

Table 1. Chemical shift of proton, Spin-Spin Coupling Constants J (Hz) and multiplicity, and self-diffusion coefficient values after 1 hour of mixing, D_{1h}, of surfactant alone and of the surfactant-zinc precursor mixtures.

Sample	α-CH$_2$ chemical shift (ppm)	α-CH$_2$ multiplicity J_{HH} (Hz)	self-diffusion coefficient, D_{1h}, ($\times 10^{10}$ m^2.s^{-1})
[Zn(Cy)$_2$]	-	-	10.7 ± 0.4
C_{12}-NH$_2$	2.55	Triplet, $J_{\alpha\beta}$ = 6.6	12.0 ± 0.3
C_{12}-NH(CH$_3$)	2.45	Triplet, $J_{\alpha\beta}$ = 7.1	13.0 ± 0.3
C_{12}-N(CH$_3$)$_2$	2.18	Triplet, $J_{\alpha\beta}$ = 7.3	13.0 ± 0.3
[Zn(Cy)$_2$] in mixtures	-	-	10.0 ± 0.2
C_{12}-NH$_2$ in mixture	2.39	Triplet of triplet, $J_{\alpha\beta}$ = 6.6, $J_{\alpha am}$ = 6.8	8.0 ± 0.2
C_{12}-NH(CH$_3$) in mixture	2.35	Doublet of triplet, J_{β} = 6.6, $J_{\alpha am}$ = 6.8	8.0 ± 0.2
C_{12}-N(CH$_3$)$_2$ in mixture	2.18	Triplet, $J_{\alpha\beta}$ = 7.3	13.0 ± 0.2

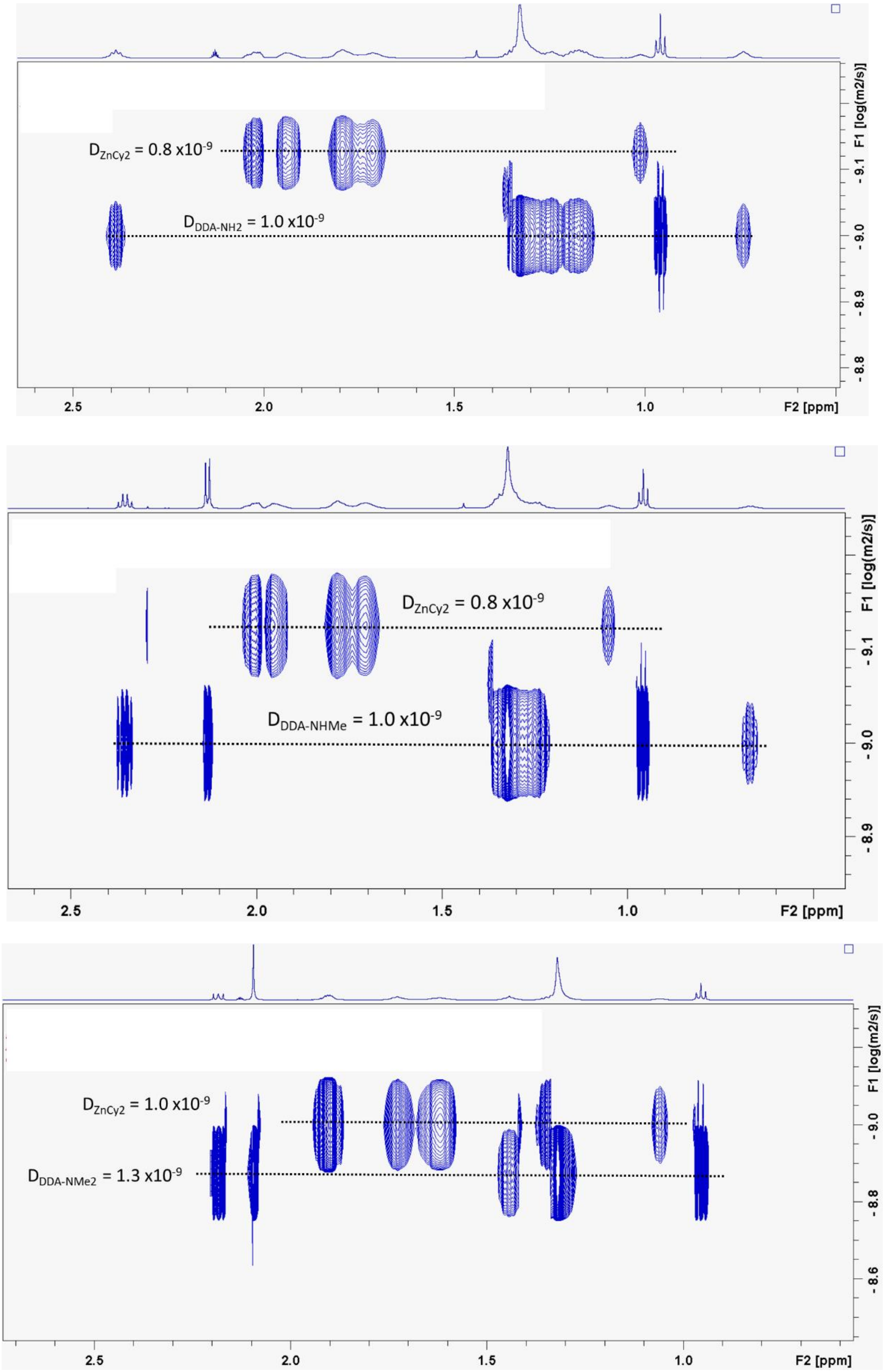

Figure 5. ^{1}H DOSY NMR spectra of [Zn(Cy)$_2$] with 2 eq. of C$_{12}$-NH$_2$ (top), C$_{12}$-NH(CH$_3$) (middle) or C$_{12}$-N(CH$_3$)$_2$ (bottom) after 1h of mixing.

This adduct formation is also supported by the change in multiplicity of the proton signal corresponding to the protons in the α-position relative to nitrogen that rises from coupling of the protons both to the β-methylene group of the alkyl chain, and eventually to the amino group protons H_{am}. The ^1H NMR spectra of the free alkylamine show a triplet signal which changes for a triplet of triplet and a doublet of triplet for C_{12}-NH_2 and C_{12}-$NH(CH_3)$, respectively. This coupling is visible because of the coordination of the surfactant to the zinc atom that slows down the exchange phenomena of the labile amino hydrogen. Changes of the self-diffusion coefficients D measured by PGSE-NMR spectroscopy also confirm the formation of this adduct (Figure 5 and Table 1).

In the same experimental conditions, the self-diffusion coefficients of the surfactant and the zinc precursor are significantly higher than those measured for the mixtures. Such observations indicate a fast exchange (on the NMR timescale) between free and coordinated amine molecules and substantiate the reversible coordination of the amine to the metal center of the zinc complex. The solutions are therefore composed of the 1:1 adduct in rapid equilibrium with the free surfactants and $[Zn(Cy)_2]$ complex. The association constants (K_a) for the different amines were determined from ^1H NMR titration data.[2]

$$[Zn(Cy_2)] + \text{amine} \leftrightarrows [Zn(Cy_2)(\text{amine})] \quad K_a \qquad \text{(eq. 1)}$$

K_a of 140 (± 40), 110 (±20), and 20 (±5) M^{-1} were estimated for the primary, secondary, and tertiary amines, respectively. These values indicate a comparable affinity of primary or secondary amines for the $[ZnCy_2]$ complex and a lower affinity of tertiary amines for the Zinc complex. The amount of adduct present in the reaction medium is therefore comparable when primary and secondary amines are used, and much lesser for the tertiary amine.

The experimental results were corroborated by DFT simulations. The structure and stability of the various $[Zn(Cy_2)(amine)]$ complexes were investigated at the DFT level, using a model hexyl chain instead of the C_{12} alkyl chain of C_{12}-NH_2, in order to reduce the computational cost. Geometries of the corresponding $[Zn(Cy)_2(C_6H_{13}NH_xMe_{2-x})]$ complexes (x = 0-2), calculated at the PBE-D3/DGDZVP level in vacuum are shown in Figure 6. In order to get as close as possible to the experimental synthesis conditions, calculations have also been made in a polarizable continuum medium (PCM). The Zinc coordination sphere remains almost unchanged when taking into account an octylamine solvent (Table 2).

Table 2. Selected geometrical data of $[Zn(Cy)_2]$ and the $[Zn(Cy)_2(C_6H_{13}NH_xMe_{2-x})]$ complexes (x = 0-2), calculated at the PBE-D3/DGDZVP level. *: PCM calculation in octylamine solvent, ε = 3.1). Distances in Å and angles in degrees.

	Zn-C distance		C-Zn-C angle	H_{axial}-C-C-H_{axial} dihedral	Zn-N distance
$[Zn(Cy)_2]$	1.972	1.972	180	160	-
$[Zn(Cy)_2]$*	1.986	1.986	179	161	-
$[Zn(Cy)_2(C_6H_{13}NH_2)]$	1.999	2.002	158	50	2.345
$[Zn(Cy)_2(C_6H_{13}NH_2)]$*	2.007	2.010	159	50	2.337
$[Zn(Cy)_2(C_6H_{13}NHMe)]$	1.998	2.003	157	84	2.368

$[Zn(Cy)_2(C_6H_{13}NHMe)]$*	2.008	2.013	156	77	2.354
$[Zn(Cy)_2(C_6H_{13}NMe_2)]$	2.005	2.010	144	84	2.407
$[Zn(Cy)_2(C_6H_{13}NMe_2)]$*	2.015	2.018	144	94	2.392

Zn–N and both Zn–C bonds are lengthened in the $[Zn(Cy)_2(C_6H_{13}NH_xMe_{2-x})]$ complex compared to the complex with the hexylamine. The C–Zn–C angle initially at 180° in $[Zn(Cy)_2]$ decreases upon rotation of the cyclohexyl ring to accommodate the steric hindrance provided by the methyl substituent(s) of the amine (Figure 6).

The nature and strengths of the Zn–C and Zn–N bonds can be described from both QTAIM and ELF topological analyses.[12]-[16] Relevant QTAIM and ELF descriptors are given in Table 2 above and Table 3 in Experimental Part, respectively. For the three Zn–amine complexes, the QTAIM description of the Zn–N bonds is in agreement with dative bonding with a weak covalence degree (V/G ≈ 1, DI ≈ 0.3). The bond strength, as indicated by the Espinosa's interaction energy E_{int},[19]-[21] is of the same order of magnitude regardless of the amine. E_{int} is equal to 14.7, 13.8, and 12.0 kcal mol^{-1} for primary, secondary, and tertiary amines, respectively. Similarly, the QTAIM description of the Zn–C bond is very close for all three complexes and corresponds to a polar covalent bond (V/G close to 2, DI ≈ 0.8). E_{int} is also comparable for $[ZnCy_2(C_6H_{13}\text{-}NH_2)]$ (42.0 and 41.5 kcal mol^{-1}) and $[ZnCy_2(C_6H_{13}NHMe)]$ (42.1 and 41.4 kcal mol^{-1}) and decreases very slightly for the tertiary amine $[ZnCy_2(C_6H_{13}NMe_2)]$ complex (40.9 and 40.8 kcal mol^{-1}) possibly because of the steric hindrance. The ELF analysis is in agreement with the above QTAIM description. The ELF descriptors of Zn–N (respectively Zn–C) bonds are almost the same regardless of the amine type. The oxidation state of the zinc atom is +Ⅱ. The weak atomic contribution of Zn to the V(N) ELF basin (lower than 3%) and the weak covariance (|cov. (V(N), C(Zn))| ≤ 0.08) are in favor of a dative Zn–N bond of weak covalence degree, while the large atomic contribution of Zn to V (Zn, C) and the large negative covariance (cov. (V(Zn, C), C(Zn)) ≈ - 0.36) are in favor of a polar covalent Zn–C bond comparable to the one of the $[Zn(Cy)_2]$ complex (see Table 4 and Figure 2 in the Experimental Part). The Zn–C bonds of the $[Zn(Cy)_2]$ fragment are only slightly affected by the amine coordination and may be described by the similar most representative mesomeric forms of about equal weight of the $[Zn(Cy)_2]$ complex (see Figure 3 in the Experimental Part).[22]

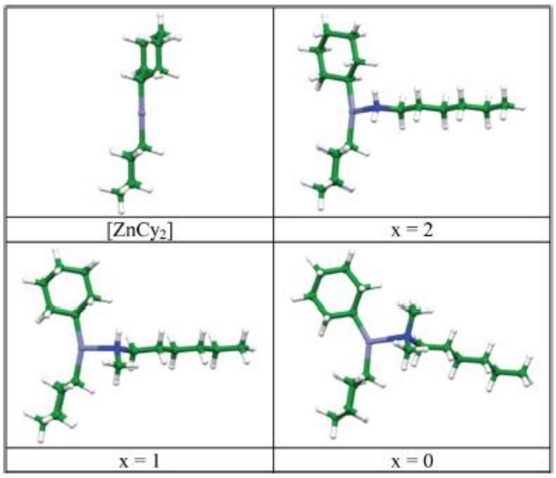

Figure 6. Geometries of [Zn(Cy)$_2$] and [Zn(Cy)$_2$(C$_6$H$_{13}$NH$_x$Me$_{2-x}$)] complexes (x = 0-2) calculated at the PBE-D3/DGDZVP level.

Gibbs energies (ΔG) of the formation of [Zn(Cy)$_2$(C$_6$H$_{13}$NH$_x$Me$_{2-x}$)] complexes (x = 0-2) and the corresponding association constants (K) were then calculated at 298 K at the PBE-D3/DGDZVP level both in vacuum and in octylamine solvent medium following eq. 2. The results are reported in Table 3.

$$[\mathrm{Zn(Cy)_2}] + \mathrm{C_6H_{13}NH_xMe_{2-x}} \leftrightarrows [\mathrm{Zn(Cy)_2(C_6H_{13}NH_xMe_{2-x})}] \qquad \text{(eq. 2)}$$

$$\Delta G = G([\mathrm{Zn(Cy)_2(C_6H_{13}NH_xMe_{2-x})}]) - G([\mathrm{Zn(Cy)_2}]) - G(\mathrm{C_6H_{13}NH_xMe_{2-x}})$$

$$\Delta G = -RT \log K$$

$$K = [\mathrm{Zn(Cy)_2(C_6H_{13}NH_xMe_{2-x})}]/([\mathrm{Zn(Cy)_2}][\mathrm{C_6H_{13}NH_xMe_{2-x}}])$$

Table 3. Gibbs energies of Zn complexes formation (ΔG in kcal mol^{-1}) and association constants (K in M^{-1}) calculated at 298 K, at the PBE-D3/DGDZVP level *: PCM calculation in octylamine solvent, ε= 3.1.

[Zn(Cy)$_2$(C$_6$H$_{13}$NH$_x$Me$_{2-x}$)]	x = 2	x = 1	x = 0
ΔG	– 1.36	–0.95	+ 1.52
ΔG*	+ 1.58	+ 1.21	+ 4.06
K	9.92	4.97	0.08
K*	0.07	0.13	0.001

Regardless of the calculation conditions (*i.e.* in vacuum or in octylamine solvent medium), ΔG (resp. ΔG*) values are little negative or positive but close to zero, except for the dimethylhexyl amine for which a significant positive value of ca +4 kcal mol^{-1} is calculated in octylamine solvent. This suggests that coordination of the tertiary amine to the zinc atom is not favorable despite a recognized higher Lewis basicity.[3] The strong steric hindrance induced by the two methyl groups thus disfavors the coordination; the electronic effects are, according to the ELF and QTAIM topological analyses of the Zn–N bond described above, identical regardless of the structure of the amine. Interestingly, the association constants of the primary and secondary amine to [ZnCy$_2$] are close to each other, whatever the reaction medium, while for the tertiary amine, the association constant is much lower, in agreement with the experimental results.

These results confirmed our hypothesis that the tertiary amine has a low propensity to form adducts, while the primary and secondary amines does. For these latter, we have shown here both experimentally and theoretically that the association constants were comparable. Therefore, the difference found in NP morphology when primary and secondary amine surfactants are used cannot originate from an initial difference in coordination to Zinc. The reactivity of the zinc–amine complexes was thus investigated from Fukui indices condensed on QTAIM and ELF basins.[23] For all three Zn–amine complexes and $[Zn(Cy)_2]$, the largest f_{ELF}^{-} (resp. f_{QTAIM}^{-}) values are only found for Zn–C bonds (resp. C atomic basins) and are very similar (see Tables 5 and 6 in the Experimental Part). The Zn–C bonds (resp. C atoms bound to Zn) appear therefore to be the most sensitive to nucleophilic attack (see Tables 5 and 6 in the Experimental Part), for example during the coordination of the amine to $[Zn(Cy)_2]$.

Before studying the role of the interaction of amines on the surface of the NPs, another reaction must therefore be considered, namely the acid-base reaction between the precursor and the surfactant that will give rise to amido complexes for primary or secondary amines only (eq. 3, x = 0 or 1).

$[Zn(Cy)_2]+C_6H_{13}NH_{1+x}Me_{1-x}\rightarrow[ZnCy(C_6H_{13}NH_xMe_{1-x})]+CyH$ (eq. 3)

3.4 Acid-base reaction

The acid-base reaction was investigated by computational DFT studies (PBE-D3/DGDZVP level of calculation). Based on the reaction Gibbs energies calculated at 298 K, this acid-base reaction is only slightly more favorable for the secondary amine than that for the primary amine (–11.3 *versus* –9.7 kcal mol^{-1}, respectively). This suggest that the acid-base reaction is not expected to play a key role in the change of the NC morphology between primary and secondary amine. However, our modeling does not take into account the possible formation of oligomers through this acid-base reaction. Indeed, in a previous study, we showed that for primary amine, this reaction leads to the formation of mono and bis-amido complexes that oligomerized over time, and which are responsible for the formation of processable gels through entanglement of the oligomers after several hours.[4] In the context of the present study, this oligomerization could be prevented by steric hindrance in the case of the secondary amine. Multinuclear NMR measurements, describe below, were therefore performed to confirm such hypothesis.

Consistent with DFT computational approach, the ^1H NMR spectra as well as the D values for C_{12}-$N(CH_3)_2$ and $[Zn(Cy)_2]$ alone (13.0 ± 0.3 and 10.7 ± 0.4, respectively) or in the mixture (13.0 ± 0.3, 10.0 ± 0.2, Table 1) evidence that the $[Zn(Cy)_2]/C_{12}$-$N(CH_3)_2$ mixture consists mostly of the free surfactants and the $[Zn(Cy)_2]$ complex. ^1H NMR spectrum recorded after two weeks shows no change (Figure 7c).

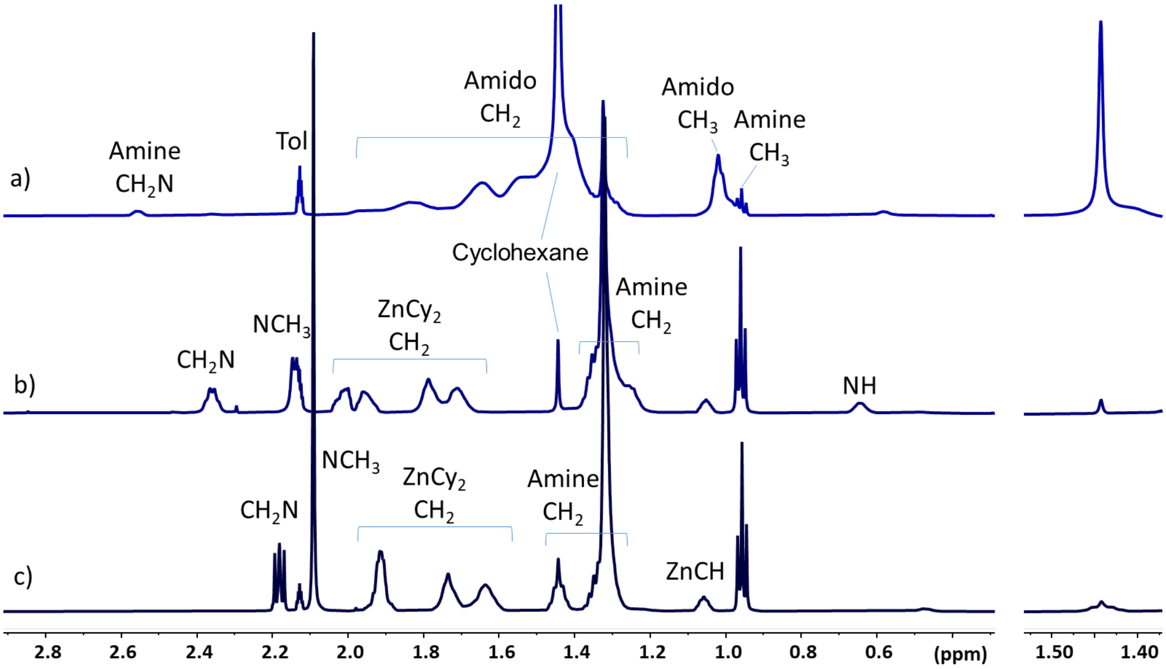

Figure 7. ^{1}H NMR spectra (298 k, Tol-d^8) of [Zn(Cy)$_2$] mixed with 2 eq. of C$_{12}$-NH$_2$ (after 190 h at 298K-after this delay, the mixture behaves as a gel[4]) (a), of C$_{12}$-NH(CH$_3$) (after 380 h at 298K and 70 h at 323K) (b) and of C$_{12}$-N(CH$_3$)$_2$ (after 380 h at 298K and 70 h at 323K) (c). Right enlargement: cyclohexane signal.

In contrast, for C$_{12}$-NH(CH$_3$), the ^{1}H NMR spectrum of the mixture exhibits similar features *(i.e.* broadening of the signals especially for α-C*H*$_2$ and NC*H*$_3$ resonances, additional peak at 2.9 ppm with a self-diffusion coefficient D of 5 ± 0.4 $\times 10^{-10}$ m^2.s^{-1}, Figure 8) as the ones observed over time for C$_{12}$-NH$_2$ (D of 6.6 and 4.3 $\times 10^{-10}$ m^2 s^{-1})[5] that are characteristic of mono and bis-amido molecular complexes (Figure 7a and b).

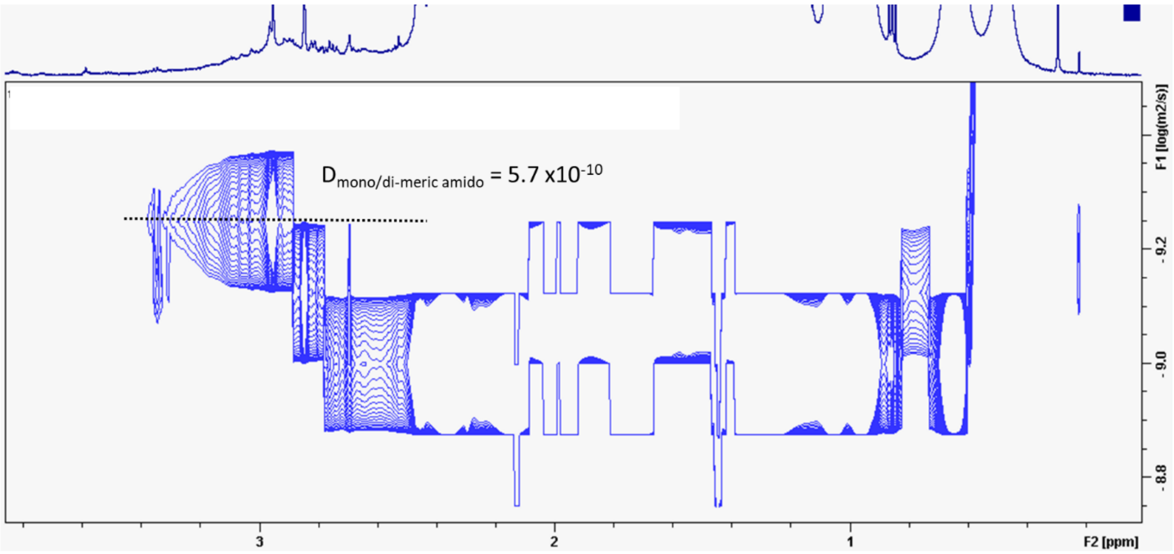

Figure 8. ^{1}H DOSY NMR spectra of [Zn(Cy)$_2$] mixed with 2 eq. of C$_{12}$-NH(CH$_3$) after 380 h at 298 K and 70 h at 323 K.

Importantly, by integration of ^{1}H liquid NMR signals, an amount of roughly 10% of amido species could be estimated. The reaction mixture is thus primarily composed of the free [Zn(Cy)$_2$] complex and the C$_{12}$-NH(CH$_3$) surfactant. The sharp signal at 1.44 ppm corresponding to evolving cyclohexane molecules from cyclohexyl protonation is observed in agreement with the acid-base reaction taking place between the amine and the Zinc precursor. Note that this peak is much more important in the case of C$_{12}$-NH$_2$ than for C$_{12}$-NH(CH$_3$) (Figure 7a,b, respectively) which substantiates that the acid-base reaction is more effective for primary amines and suggests that oligomerization occurs only in this case.

This result was confirmed by ^{13}C MAS NMR study evidencing that no formation of Zn amido oligomers occurs when [Zn(Cy)$_2$] and 2 equiv. C$_{12}$-NHCH$_3$ are mixed (Figure 9-11).

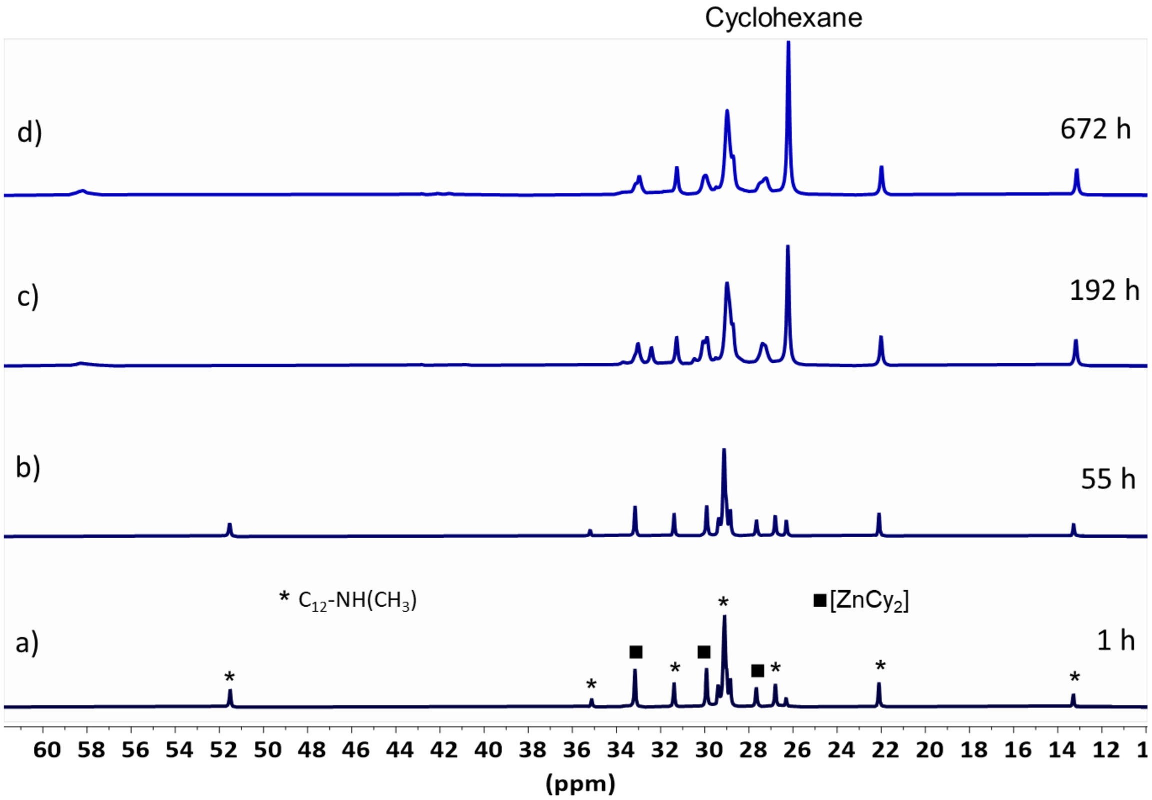

Figure 9. ^{13}C INEPT MAS NMR spectra (295 K) of [Zn(Cy)$_2$] with 2 eq. of C$_{12}$-NH(CH$_3$) after mixing of 1 h (a). 55 h (b). 8 days (c) and 28 days (d).

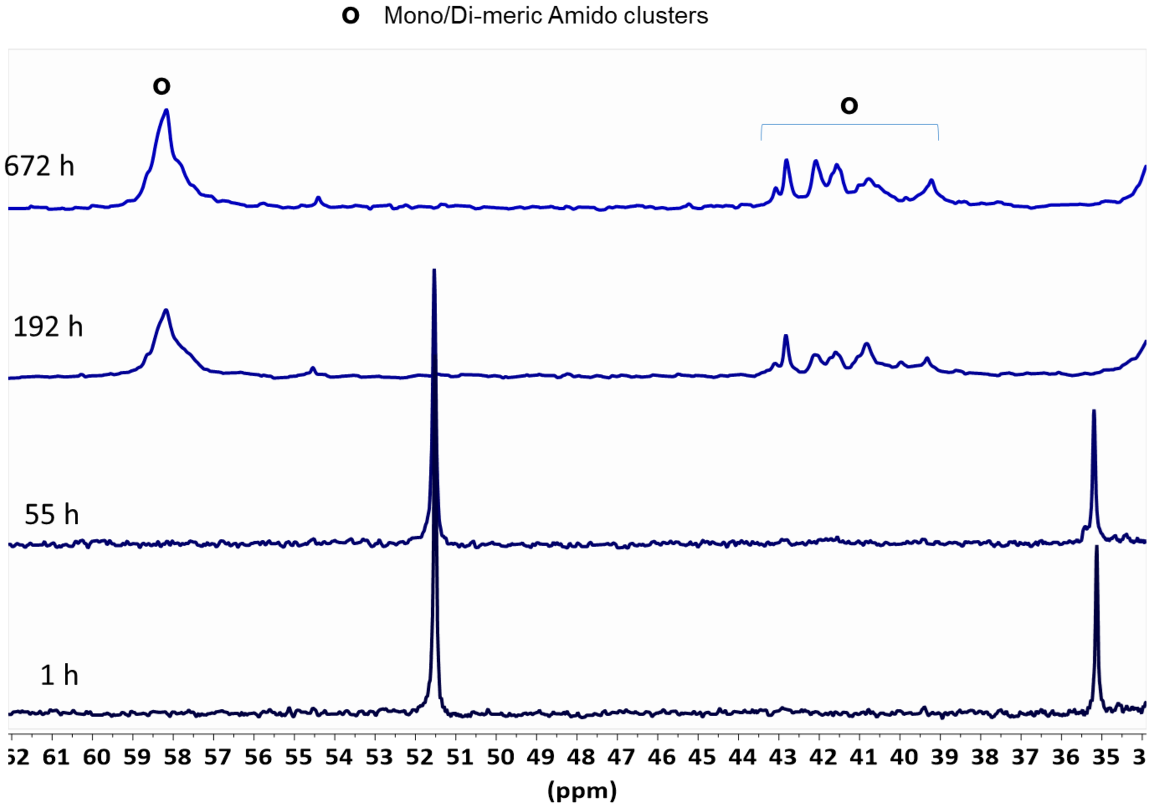

Figure 10. Enlargement of ^{13}C INEPT MAS NMR spectra (295 K) of $[Zn(Cy)_2]$ with 2 eq. of C_{12}-$NH(CH_3)$ after mixing of 1 h (a). 55 h (b). 8 days (c) and 28 days (d).

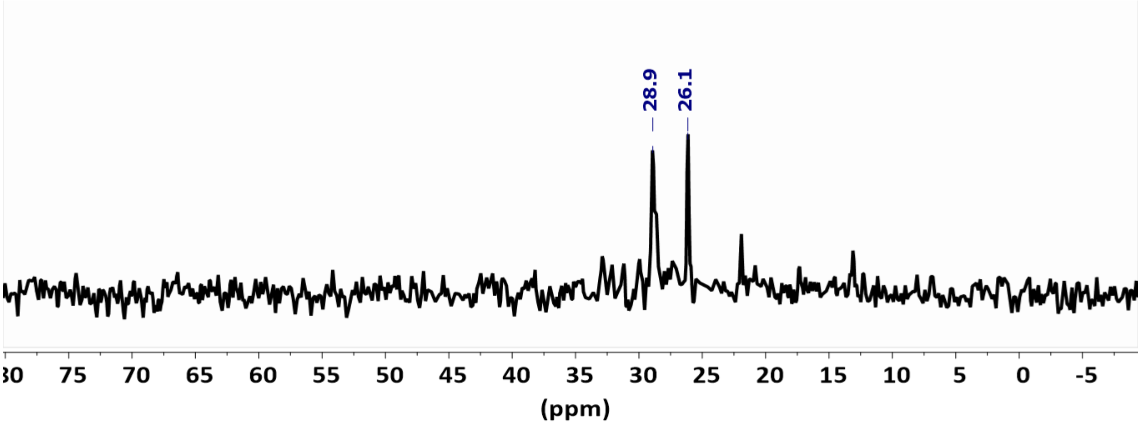

Figure 11. ^{13}C CPMAS NMR spectrum (295 K) of $[Zn(Cy)_2]$ with 2 eq. of C_{12}-$NH(CH_3)$ after mixing of 28 days.

After 55 h of mixing, the only change observed in the ^{13}C INEPT experiment is a small increase of the cyclohexane signal at 26.2 ppm. After 8 days, in addition to a notable increase of the cyclohexane signal, new ^{13}C INEPT signals appear notably in the 57-59 and 38-44 ppm ranges. These signals are characteristic of the formation of different molecular species made of monomeric and dimeric Zn amido complexes. However, no ^{13}C CPMAS signal is observable stating that such molecular species remain small and exhibit high mobility, which assert that they are not oligomers. After 28 days, these signal just slightly increase and only very weak ^{13}C CPMAS signals could be detected.

Thus, while both primary and secondary amines lead to Zn amido complexes, a notable difference is observed between primary and secondary amines: secondary amines are too hindered and only primary amines form oligomers. However, our NMR study showed that such oligomerization takes place on the timescale of several hours[4] and on the other hand, the preparation of ZnO nanorods requires hydrolysis to be conducted for three days to achieve a maximum aspect ratio. In order to know whether the oligomers observed with the primary amines are responsible for the formation of the nanorods, it is therefore important to know which of the two oligomerization or the hydrolysis has the higher rate.

3.5 [Zn(Cy)₂] hydrolysis *vs* acid-base reaction

Controlled hydrolysis of [Zn(Cy)$_2$] in the presence of C$_{12}$-NH$_2$ was performed using ^{17}O-enriched water (40%). Samples were taken at different time (between 10 minutes and 6.5 hours) and ^{1}H, DOSY, ^{13}C, and ^{17}O NMR experiments conducted. First, ^{1}H spectra evidenced a decrease of the [Zn(Cy)$_2$] resonances until their complete disappearance after a reaction time of about 2 h (Figure 12). [Zn(Cy)$_2$] starting precursor is completely consumed after this time.

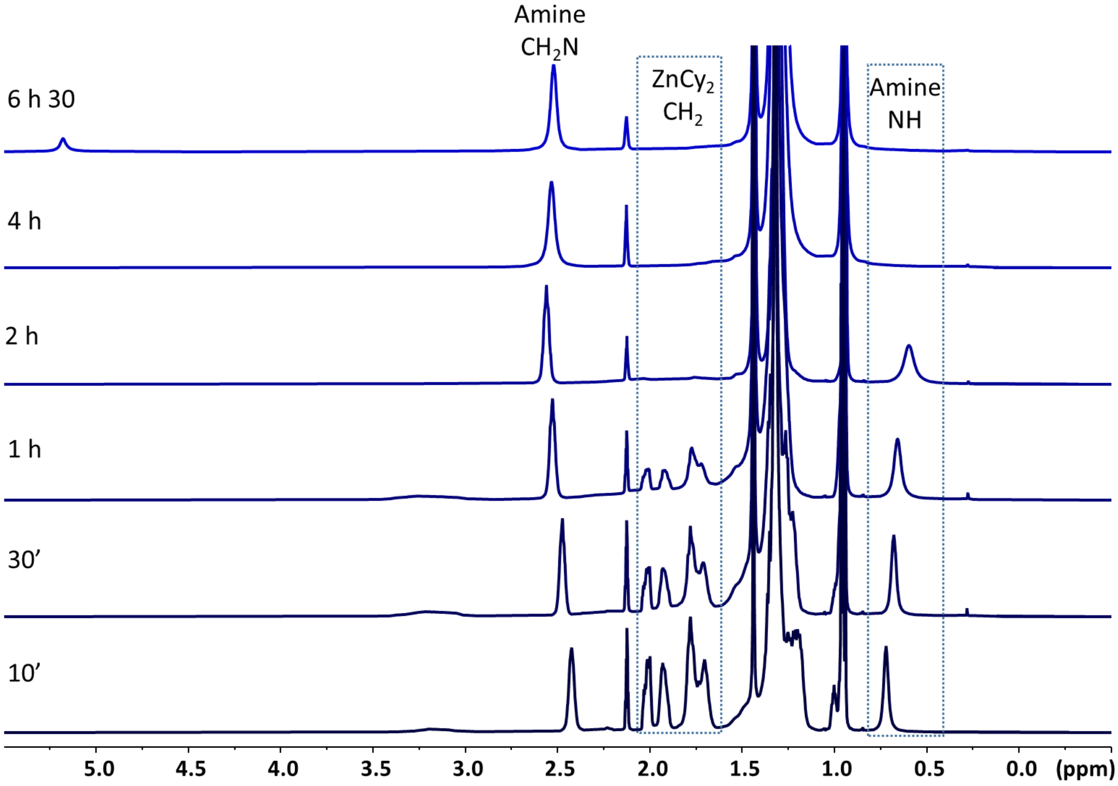

Figure 12. ^{1}H NMR spectra (298 K, toluene-d^8) of [Zn(Cy)$_2$] mixed with 2 eq. of C$_{12}$-NH$_2$ after different hydrolysis reaction time.

Concomitantly, ^{1}H resonances of C$_{12}$-NH$_2$ changed; especially the ones of N*H* and α-C*H*$_2$ groups, which shows that C$_{12}$-NH$_2$ electronic environment changes over time. Importantly, the broad and weak signals detected around 3 ppm, which superimposed the ones previously assigned to mono- and dimeric zinc amido complexes and zinc amido oligomers (Figure 13) exhibit diffusion coefficient values between 5.7 and 4.0 $\times10^{-10}$ m^2 s^{-1} (Figure 14), which is consistent with D values measured for mono- and dimeric zinc amido complexes but definitely not with oligomeric species[4] (1.3 $\times10^{-10}$ m^2 s^{-1}).

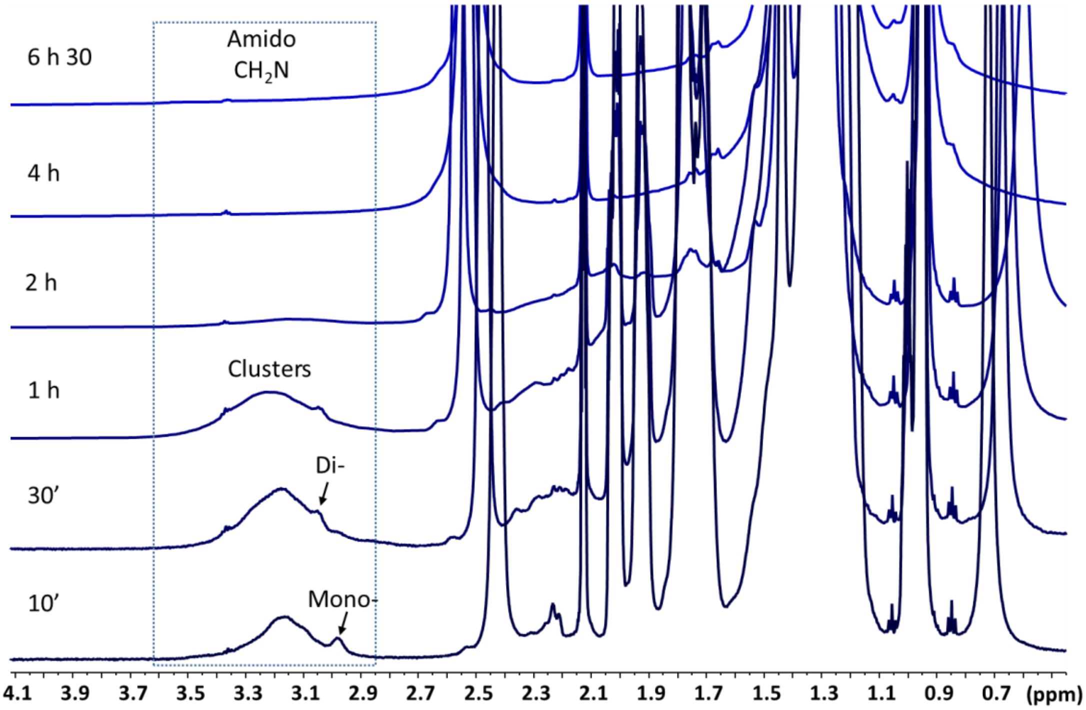

Figure 13. Vertical enhancement of the ^{1}H NMR spectra (298 K, toluene-d^8) of $[Zn(Cy)_2]$ mixed with 2 eq. of C_{12}-NH_2 after different hydrolysis reaction time presented Figure 12.

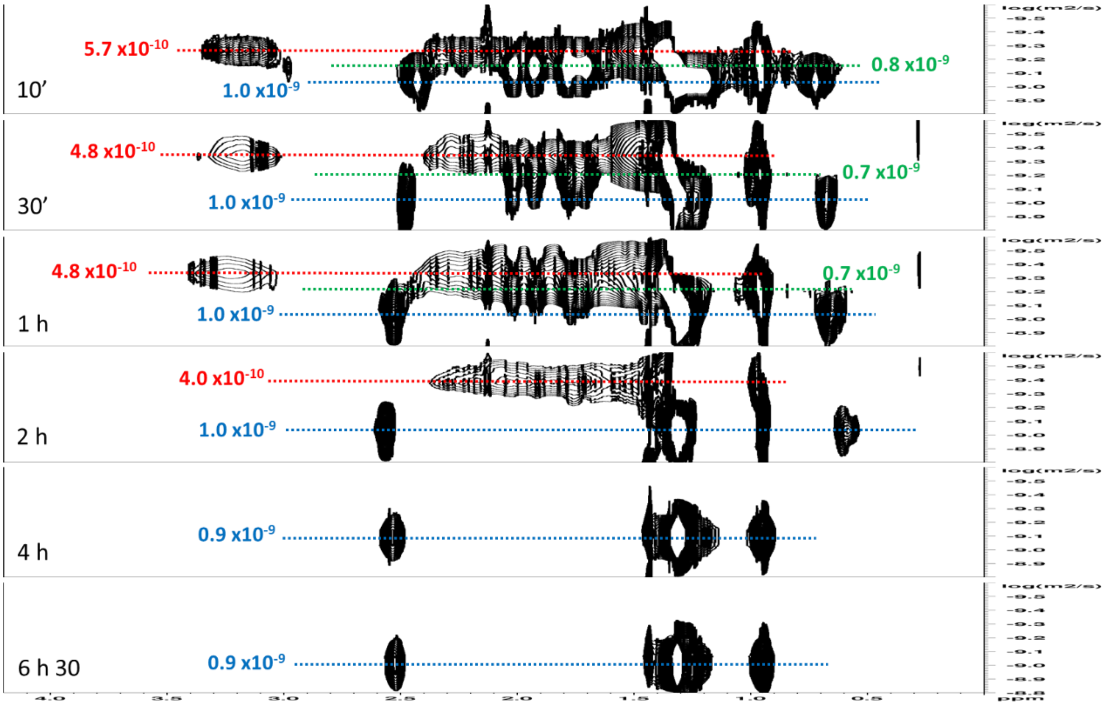

Figure 14. ^{1}H DOSY NMR spectra (298 K, toluene-d^8) of $[Zn(Cy)_2]$ mixed with 2 eq. of C_{12}-NH_2 after different hydrolysis reaction time.

^{13}C INEPT and CP MAS experiment confirmed the formation of the Zn-amido complexes only. Up to 2 h, characteristic ^{13}C signals of amido α-CH_2 and β-CH_2 groups are indeed observed at 48.1 and 37.5 ppm only in INEPT spectra (Figure 15) but not in the CP MAS ones (Figure 16).

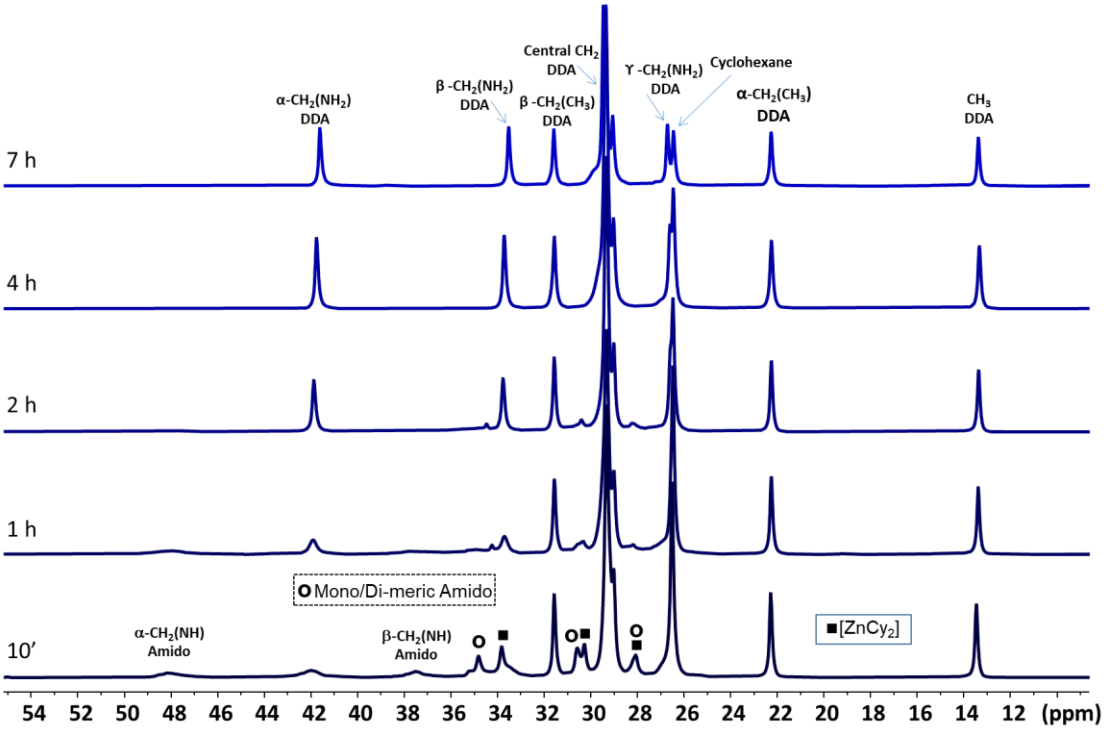

Figure 15. ^{13}C INEPT MAS NMR spectra (295 K) of [Zn(Cy)$_2$] with 2 eq. of C_{12}-NH_2 under water vapor with mixing time.

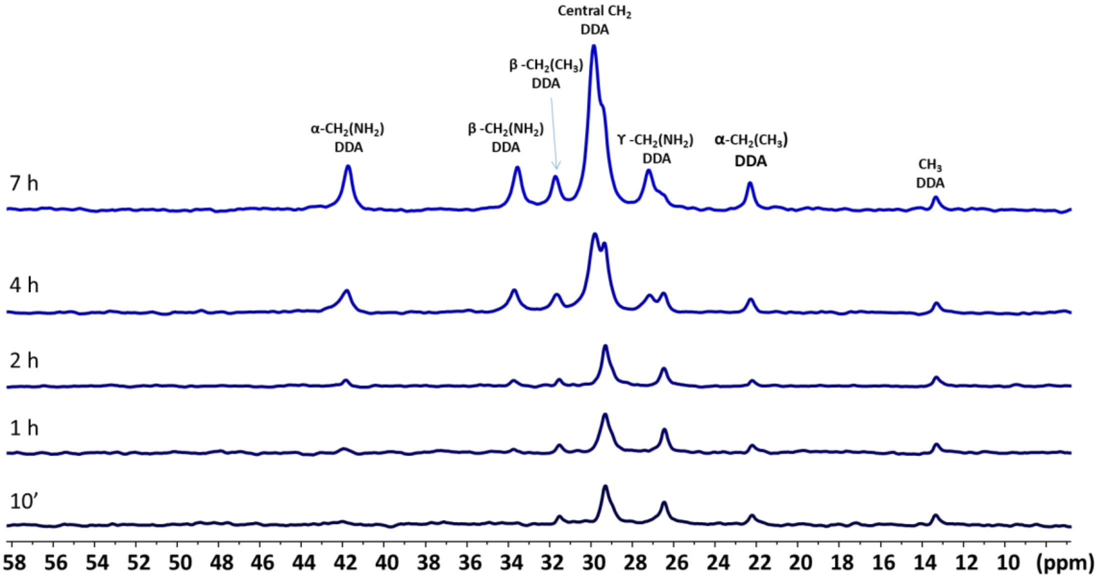

Figure 16. ^{13}C CP MAS NMR spectra (295 K) of [Zn(Cy)$_2$] with 2 eq. of C_{12}-NH_2 under water vapor with mixing time.

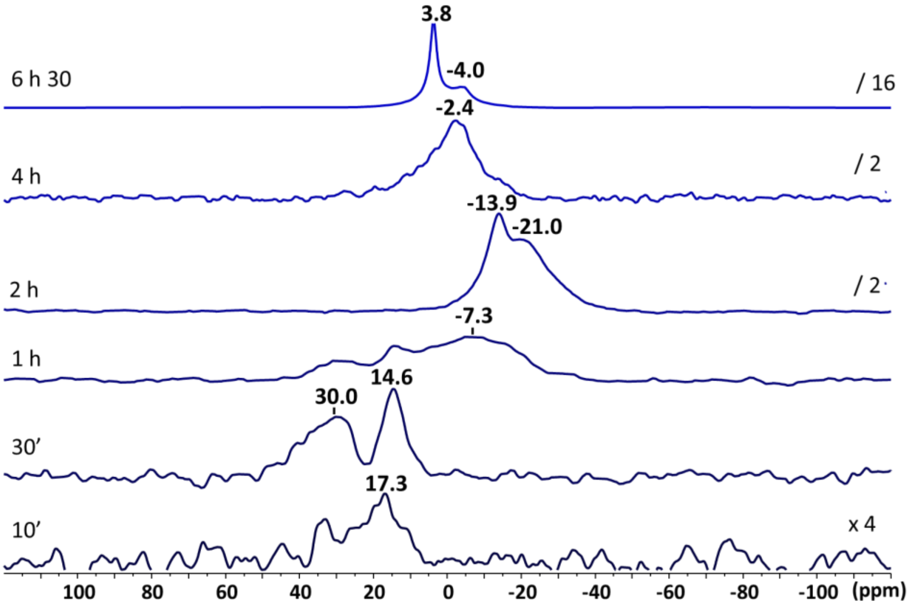

Figure 17. ^{17}O NMR spectra (298 K, toluene-d^8) of [Zn(Cy)$_2$] mixed with 2 eq. of C_{12}-NH_2 after different hydrolysis reaction time.

After 2 h, these INEPT signals disappear and no signal associated to oligomers shows up in the CP experiment. Finally, after 7 h, both CP and INEPT ^{13}C MAS spectra show signals typical of C_{12}-NH_2 stabilizing ZnO NCs.[6] Figure 17 shows ^{17}O NMR spectra recorded over time. After 10 min, weak and broad signals are observed in the 10-40 ppm range. Their intensity and resolution increase significantly for 30 min of hydrolysis time and signals at 14.6 and 30.0 ppm are clearly observed. These latter can tentatively be assigned to hydroxyl groups and water molecules within zinc molecular complexes as they definitely do not correspond to ZnO for which classical ^{17}O signals are observed between –18 to –30 ppm.[7] They can neither be attributed to Zn–O–Cy species, since no correlating ^1H resonance can be detected above 3.5 ppm (Figure 13). After 1 h, the new broad resonance observed at –7.3 ppm can be assigned to various small-sized [$Zn_{x+y}O_x(OH)_{2y}$] clusters, nuclei of future ZnO NCs. The evolution of the ^{17}O signals over time confirms this hypothesis: after 2 h, signals at –13.9 and –21.0 ppm remained the ones observed for ZnO NCs,[8] suggesting the formation of small dispersible ZnO NCs at this early stage of the reaction. The disappearance of these signals at longer time is due to the formation of large ZnO NCs that no longer give observable liquid-state NMR signal. The signal around 0.0 ppm is characteristic of water molecules interacting with ZnO NCs surface, in fast exchange between solution and the surface of ZnO.[8]

Overall, the detailed multinuclear NMR analysis established that the hydrolysis reaction takes precedence over any oligomerization process that occur with primary amine surfactants in the absence of water. These results suggest that the difference in morphology is not chiefly due to significant differences at the early stage of molecular state between primary and secondary amines. This prompted us to examine, in more details, the interaction and surface dynamics of the various alkyl amines on the ZnO NCs.

3.6 Amine interaction with ZnO NCs and surface dynamics.

The interaction of amines on the surface of ZnO NCs can be studied by solid state NMR.[8] [9] In brief, while DP is not selective and shows all the species on the NCs surface regardless of their dynamics, CP and INEPT sequences evidence selectively rigid and mobile species, respectively. Figure 18 compares the ^{13}C CP, DP and INEPT MAS NMR spectra of ZnO NCs stabilized by either C_{12}-NH_2 (ZnO@C_{12}-NH_2, Figure 18 left) or C_{12}-$NH(CH_3)$ (ZnO@C_{12}-$NH(CH_3)$, Figure 18 right).

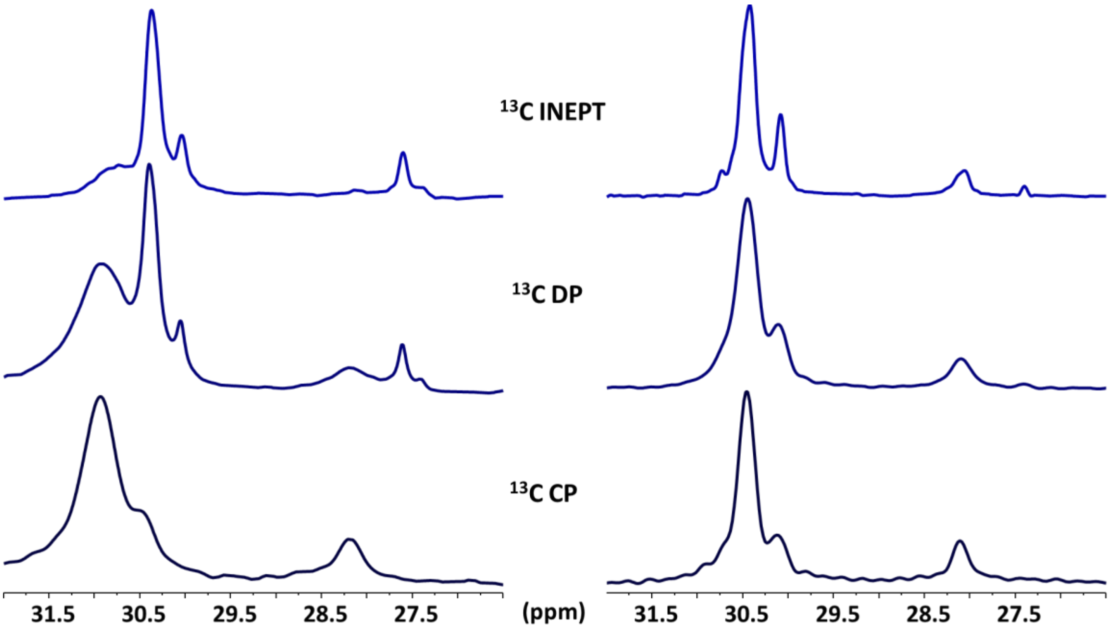

Figure 18. ^{13}C CP, DP and INEPT MAS NMR spectra (295 K) of ZnO stabilized with 0.2 eq. of C_{12}-NH_2 (left), and with 0.2 eq. of C_{12}-$NH(CH_3)$ (right).

First of all, INEPT spectra exhibit similar central CH_2 signals for both ZnO@C_{12}-$NH(CH_3)$ and ZnO@C_{12}-NH_2 stating that the mobile amine possesses the same conformation regardless of their structure. Second, ZnO@C_{12}-$NH(CH_3)$ exhibit similar ^{13}C spectra regardless of the polarization mode which suggests that C_{12}-$NH(CH_3)$ possess the same conformation regardless of its dynamics. This contrasts with the ZnO@C_{12}-NH_2 spectra for which the CP and INEPT spectra are very different stating that mobile and rigid C_{12}-NH_2 possess different conformations. Moreover, sharper CP MAS signals are clearly observed for ZnO@C_{12}-$NH(CH_3)$ NCs than for ZnO@C_{12}-NH_2. This important result points out to an increase in chain mobility of the rigid C_{12}-$NH(CH_3)$ compared to the rigid C_{12}-NH_2 at the ZnO surface and suggests weaker interactions of the C_{12}-$NH(CH_3)$ with the ZnO surface than the ones of C_{12}-NH_2. Importantly, CP *J*-resolved experiment performed on ZnO@C_{12}-NH_2 evidenced a bent conformation of C_{12}-NH_2 at the ZnO surface induced by hydrogen bonds.[9] Such bent conformation is not observed for C_{12}-$NH(CH_3)$ highlighting the absence of hydrogen bonds in ZnO@C_{12}-$NH(CH_3)$.

Finally, a transferred NOE experiment,[5] was realized on ZnO NPs in solution with 1 equiv. of C_{12}-NH_2 and 10 equiv of C_{12}-$NH(CH_3)$ (Figure 19).

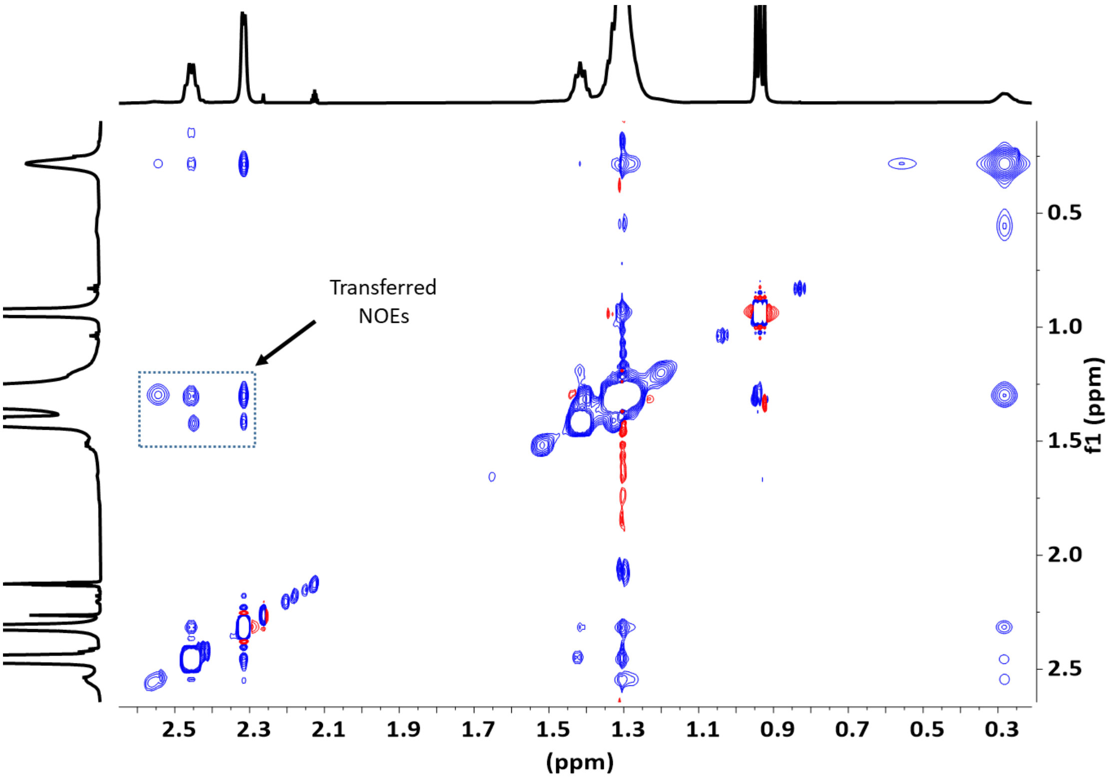

Figure 19. ^1H NOESY NMR spectra of ZnO with 1 eq. of C_{12}-NH_2 and 10 eq. of C_{12}-$NH(CH_3)$.

Despite the large excess of secondary amine introduced, the typical primary amine ^1H α-CH_2 signal at 2.54 ppm is strongly broadened and showed an intense transferred NOE correlation, which evidences that the presence of a large 10-fold excess of secondary amine compared to the corresponding primary amine, do not lead to any sensible decrease of the quantity of primary amine at the ZnO surface. This clearly confirms the higher affinity of the primary amine for ZnO.

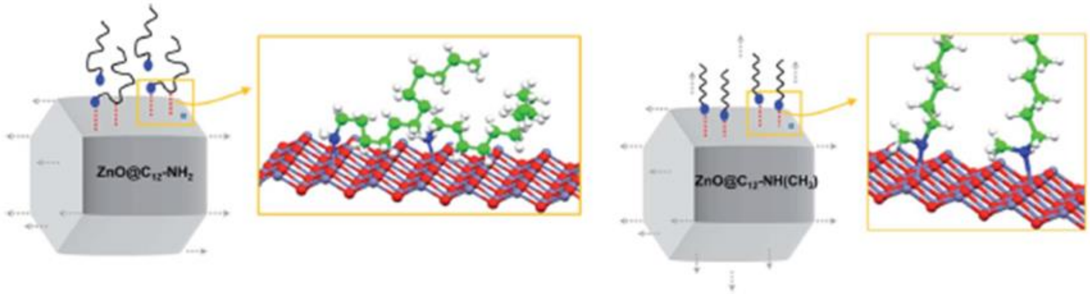

Scheme 1. Overview of the proposed model for either the anisotropic or isotropic growth of ZnO depending on the structure of the amines which are localized on the lateral faces of the NCs, namely primary or secondary amine, respectively. H-bonds formed between primary amine and ZnO surface reduced their mobility while secondary amine remains mobile at the surface of the NC.

From a geometrical perspective (Scheme 1), multiple H-bonding formed between primary amine and ZnO surface reduce the mobility of primary amines at the surface of the NC. This additional network mainly localizes along the lateral faces of the NCs (left),[5] and is directly responsible for the 1D anisotropic growth of ZnO NCs. Conversely, the secondary amine surfactant does not form such hydrogen bonding network, or to a much limited extent (right). They consequently remain mobile over the entire surface of the NCs, and a formal 3D isotropic growth is expected from such situation. In the last system, in ZnO aggregates formed in the presence of tertiary amine C_{12}-$N(CH_3)_2$, the amine much weakly interact with the surface of NCs, and it does not participate to segregate the particles or to orientate any particular growth. Accordingly, no NOE-Tr signal is observed (Figure 20).[5] The precursor colloids formed in solution are not sufficiently stabilized and therefore aggregate.

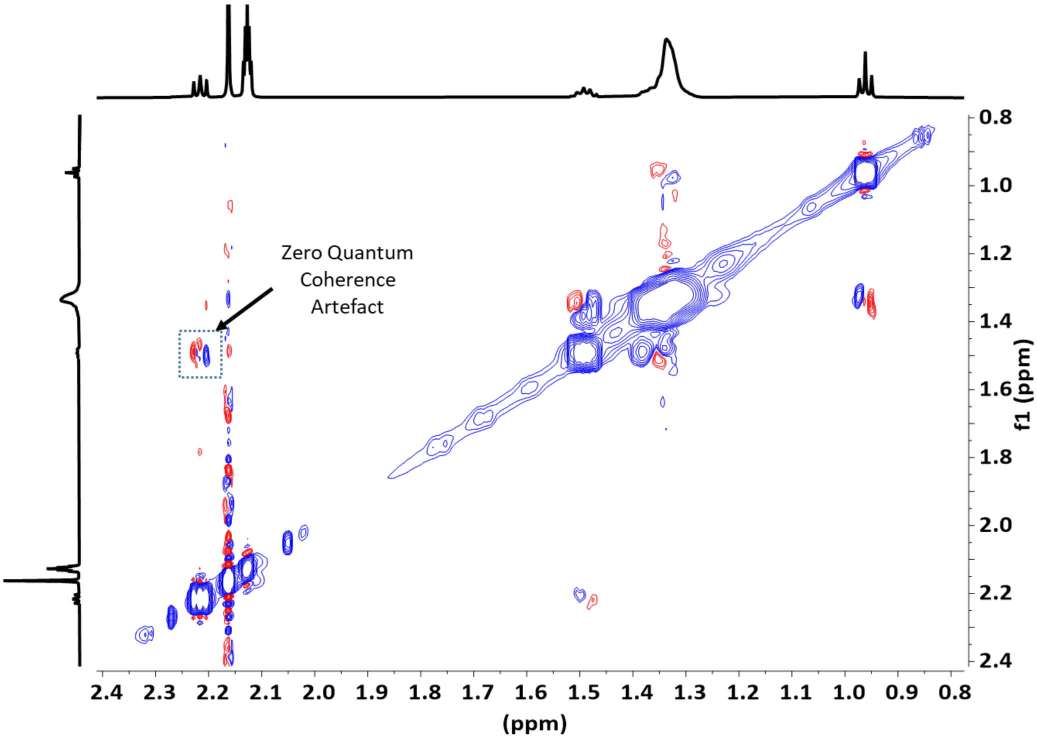

Figure 20. ^1H NOESY NMR spectra of ZnO with x eq. of C_{12}-$N(CH_3)_2$

3.7 Conclusions

In this chapter, we focused the effect of the structure of the amine (primary, secondary or tertiary) by keeping the aliphatic chain length constant. Regardless of the amine structure, a 1:1 adduct is originally formed. However, while its association constant is consistent for related primary and secondary amine, it is one order of magnitude smaller for the corresponding tertiary amine. The difference between primary and secondary amine surfactants comes from the propensity of primary amine to form zinc-amido oligomers, a reaction which is impeded in the case of secondary amine because of a higher steric hindrance.

However, the reaction rate of such oligomerization was proved much slower than the competitive hydrolysis reaction generating the NPs, and has a negligible influence over NPs structuring. We thus demonstrated that the difference in morphology between ZnO NPs observed as a function of the amine structure arises from a strong difference in their dynamics at the surface of the growing NPs. Multiple H-bonding interaction at ZnO surface for primary amine, identified by ^{13}C MAS NMR, leads to a reduced mobility of these amine compared to secondary amines, which remain mobile at the surface of the NPs in all the dimension of space.

Our approach in the present study could clearly be extended to a great number of metal and semi-conducting nanoparticles stabilized in solution by surfactants such as thiols, carboxylic acids, phosphines, carbenes, etc. This would provide fundamental knowledge towards a rationalized vision of the mild and controlled synthesis of NCs in solution. Most importantly, we have shown herein that the efficient and very widespread use of primary amines in the synthesis of nanoparticles via solution protocols is attributable to weak interaction hydrogen bonds with strong influence on the surface of the growing nanoparticle and final morphology and the structure of the end hybrid material.

In view of the discovered gelation phenomenon, it's believed the existence of gelation phenomenon plays some kind of role in the formation of ZnO nano-objects. Thus, it matters also continuing going further to investigate the gelation kinetic to figure out what the driving force is in gelation process. This will be detailed presented in next chapter.

3.8 Computational details

Geometries were fully optimized at the PBE-D3/DGDZVP level of calculation using Gaussian09.[10] Vibrational analysis was performed at the same level as the geometry optimization. Solvent effects of octylamine (ε = 3.1)[11] were included using the polarizable continuum model (PCM) implemented in Gaussian09. The influence of the length of the alkyl chain of the model amine of C_{12}-NH_2 was studied. No significant difference was found in the results using either hexylamine ($H_2NC_6H_{13}$) or octylamine ($H_2NC_8H_{17}$). The former was therefore selected in order to reduce the computational cost. However, octylamine was used as the solvent in PCM calculations, as its required dielectric constant was known.

Electron Localization Function (ELF)[12] [13] topological analysis and Quantum Theory of Atoms in Molecules (QTAIM)[14] [15] analysis were performed with the TopMod package.[16] ELF maps were plotted using the Molekel program.[17] QTAIM analysis was also performed with the AIMAll software.[18]

References

[1] Z. Zhao, Z. Zheng, C. Roux, C. Delmas, J. D. Marty, M. L. Kahn and C. Mingotaud, "Importance of the Correlation between Width and Length in the Shape Analysis of Nanorods: Use of a 2D Size Plot To Probe Such a Correlation", *Chem.–Eur. J.*, **2016**, *22*, 12424–12429.

[2] P. Thordarson, "Determining association constants from titration experiments in supramolecular chemistry", *Chem. Soc. Rev.*, **2011**, *40*, 1305–1323.

[3] R. J. Ouellette and J. David Rawn, "Organic Chemistry Study Guide: Organic chemistry study guide: Key concepts, problems, and solutions", *Elsevier*, **2015**, pp. 465–494.

[4] Z. Zhao, Y. Coppel, J. Fitremann, P. Fau, C. Roux, C. Lepetit, P. Lecante, J.-D. Marty, C. Mingotaud and M. L. Kahn, "Mixing Time between Organometallic Precursor and Ligand: A Key Parameter Controlling ZnO Nanoparticle Size and Shape and Processable Hybrid Materials", *Chem. Mater.*, **2018**, *30*, 8959–8967.

[5] Y. Coppel, G. Spataro, C. Pages, B. Chaudret, A. Maisonnat and M. L. Kahn, "Full characterization of colloidal solutions of long‐alkyl‐chain‐amine‐stabilized ZnO nanoparticles by NMR spectroscopy: surface state, equilibria, and affinity", *Chem.–Eur. J.*, **2012**, *18*, 5384–5393.

[6] G. Spataro, Y. Champouret, P. Florian, Y. Coppel and M. L. Kahn, "Multinuclear solid-state NMR study: a powerful tool for understanding the structure of ZnO hybrid nanoparticles", *Phys. Chem. Chem. Phys.*, **2018**, *20*, 12413–12421.

[7] Y. Champouret, Y. Coppel and M. L. Kahn, "Evidence for Core Oxygen Dynamics and Exchange in Metal Oxide Nanocrystals from In Situ ^{17}O MAS NMR", *J. Am. Chem. Soc.*, **2016**, *138*, 16322–16328.

[8] G. Spataro, Y. Champouret, P. Florian, Y. Coppel and M. L. Kahn, Phys. "Multinuclear solid-state NMR study: a powerful tool for understanding the structure of ZnO hybrid nanoparticles", *Chem. Chem. Phys.*, **2018**, *20*, 12413–12421.

[9] M. L. Kahn, T. Cardinal, B. Bousquet, M. Monge, V. Jubera and B. Chaudret, "Optical properties of zinc oxide nanoparticles and nanorods synthesized using an organometallic method", *ChemPhysChem*, **2006**, *7*, 2392–2397.

[10] M. J. Frisch, G. W. Trucks, H. B. Schlegel, G. E. Scuseria, M. A. Robb, J. R. Cheeseman, G. Scalmani, V. Barone, B. Mennucci, G. A. Petersson, H. Nakatsuji, M. Caricato, X. Li, H. P. Hratchian, A. F. Izmaylov, J. Bloino, G. Zheng, J. L. Sonnenberg, M. Hada, M. Ehara, K. Toyota, R. Fukuda, J. Hasegawa, M. Ishida, T. Nakajima, Y. Honda, O. Kitao, H. Nakai, T. Vreven, J. A. Montgomery Jr, J. E. Peralta, F. Ogliaro, M. Bearpark, J. J. Heyd, E. Brothers, K. N. Kudin, V. N. Staroverov, R. Kobayashi, J. Normand, K. Raghavachari, A. Rendell, J. C. Burant, S. S. Iyengar, J. Tomasi, M. Cossi, N. Rega, J. M. Millam, M. Klene, J. E. Knox, J. B. Cross, V. Bakken, C. Adamo, J. Jaramillo, R. Gomperts, R. E. Stratmann, O. Yazyev, A. J. Austin, R. Cammi, C. Pomelli, J. W. Ochterski, R. L. Martin, K. Morokuma, V. G. Zakrzewski, G. A. Voth, P. Salvador, J. J. Dannenberg, S. Dapprich, A. D. Daniels, O. Farkas, J. B. Foresman, J. V. Ortiz, J. Cioslowski and D. J. Fox, Gaussian 09, Revision D.01, Gaussian, Inc., Wallingford CT, 2009.

[11] P. M. Chassaing, F. Demangeot, V. Paillard, A. Zwick, N. Combe, C. Pag`es, M.

L. Kahn, A. Maisonnat and B. Chaudret, Phys. Rev. B: Condens. “Surface optical phonons as a probe of organic ligands on ZnO nanoparticles: An investigation using a dielectric continuum model and Raman spectrometry”, *Matter Mater. Phys.*, **2008**, *77*, 153306.

[12] A. D. Becke and K. E. Edgecombe, “A simple measure of electron localization in atomic and molecular systems”, *J. Chem. Phys.*, **1990**, *92*, 5397–5403.

[13] B. Silvi and A. Savin, “Classification of chemical bonds based on topological analysis of electron localization functions”, *Nature*, **1994**, *371*, 683–686.

[14] R. F. W. Bader, “X-Ray Analyses and the Structure of Organic Molecules”, in Atoms In Molecules, Clarendon Press, Oxford, UK, **1990**.

[15] R. F. W. Bader and H. Essen, “The characterization of atomic interactions”, *J. Chem. Phys.*, **1984**, *80*, 1943–1960.

[16] S. Noury, X. Krokidis, F. Fuster and B. Silvi, “Computational tools for the electron localization function topological analysis”, *Comput. Chem.*, **1999**, *23*, 597–604.

[17] Molekel 4.3 from CSCS, http://www.cscs.ch/molekel/.

[18] T. A. Keith, AIMAll (Version 17.11.04), TK Gristmill Software, Overland Park KS, USA, http://www.aim.tkgristmill.com.

[19] E. Espinosa, E. Molins and C. Lecomte,” Hydrogen bond strengths revealed by topological analyses of experimentally observed electron densities”, *Chem. Phys. Lett.*, **1998**, *285*, 170–173.

[20] E. Espinosa, I. Alkorta, I. Rozas, J. Elguero and E. Molins, “About the evaluation of the local kinetic, potential and total energy densities in closed-shell interactions”, *Chem. Phys. Lett.*, **2001**, *336*, 457–461.

[21] Eint = $- 1/2V_{bcp}$ and Eint (kcal mol^{-1}) = $- 313.754 \times V_{bcp}$ (au).

[22] C. Lepetit and M. L. Kahn, “QTAIM and ELF topological analyses of zinc-amido complexes”, *Res. Chem. Intermed.*, **2021**, *47*, 377–395.

[23] W. Tiznado, E. Chamorro, R. Contreras and P. Fuentealba, “Comparison among four different ways to condense the Fukui function”, *J. Phys. Chem.*, **2005**, *109*, 3220–3224.

Chapter IV. The driving force of the formation of the gel

As discussed in the previous chapters, in the organometallic pathway leading to ZnO NPs, the discovered gelation process has important consequences on the final size and shape of the synthetized NPs. It is therefore paramount to determine the rheological properties of the gels as well as the important parameters controlling their formation and behavior. In this chapter, we described the macroscopic rheology and molecular NMR measurements performed on the [Zn(Cy)$_2$] organometallic precursor and a primary alkyl amine mixture. We focused our attention (both at a macroscopic and a molecular scale) on the effect of the alkyl chain length (from pentyl, C5 to dodecyl, C12) on the formation of the zinc organometallic gels. Rheological measurements gave us access to values of the elastic and viscous moduli, respectively, G' and G", which are macroscopic data to define after which time the mixture changes from a liquid state to the gel state. NMR spectroscopic studies gave us access to complementary information on the molecular scale of how gelation takes place.

To set up the rheological measurements, two requirements which represent experimental difficulties had to be overcome. The first one is that the measurement had to be performed under inert atmosphere so that the hydrolysis of the mixture was avoided. Since the rheometer is not a tightly closed system (measurements were made with a 25 mm plate−plate aluminum geometry with a gap of 500 μm, see Experimental Part), to the contrary of a glove box and/or NMR tubes, an extra plastic cylinder was placed around the geometry to avoid drying and a slow nitrogen flow is maintained during the whole measurement. With amines of high boiling point[1] (octylamine: b.p. = 176°C or dodecylamine, b.p. = 259°C), the flow did not flush out the amines. But with shorter alkyl chain amines (b.p. hexylamine 131°C), even when the flow is set up at the minimum to avoid hydrolysis, the flow probably flushed out a part of the amine, leading to changes in the mixture proportions. Rheological measurements thus reflected both stoichiometric modifications and effects of the gelation. The second difficulty to monitor the gelation by rheology is the fact that the moduli increased from c.a. 0.1 Pa to c.a. 10000 Pa, that is, 5 orders of magnitude. The applied stress must be adapted throughout the experiment to keep a good sensitivity (see Experimental Part). But if a brutal increase of the applied stress is applied, the sample structure breaks. Thus, stepwise and delicate increase of the stress must be applied. Even by applying these two constraints, avoiding hydrolysis and breakage was not granted all the time, making the measurement a bit tricky.

4.1 Rheology measurement

Starting with octylamine, direct observation with naked eyes of the amine/Zn precursor suggested that strong changes occurred around 8h after mixing. Therefore, to perform the rheological experiments, a fresh mixture was prepared and left to mature in the glove box during 4 hours. Then, the mixture is injected in the rheometer chamber and protected from the air by a nitrogen flux. The gelation process can be monitored by registering the changes of the elastic and viscous moduli (respectively G′ and G) with a sinusoidal stress amplitude comprised between 0.1 and 100 Pa, at a frequency of 1 Hz from 0 to 22h after injection of the sample in the rheometer geometry. Figure 1 shows the rheogram for the [Zn(Cy)2] – octylamine (OA) mixture.

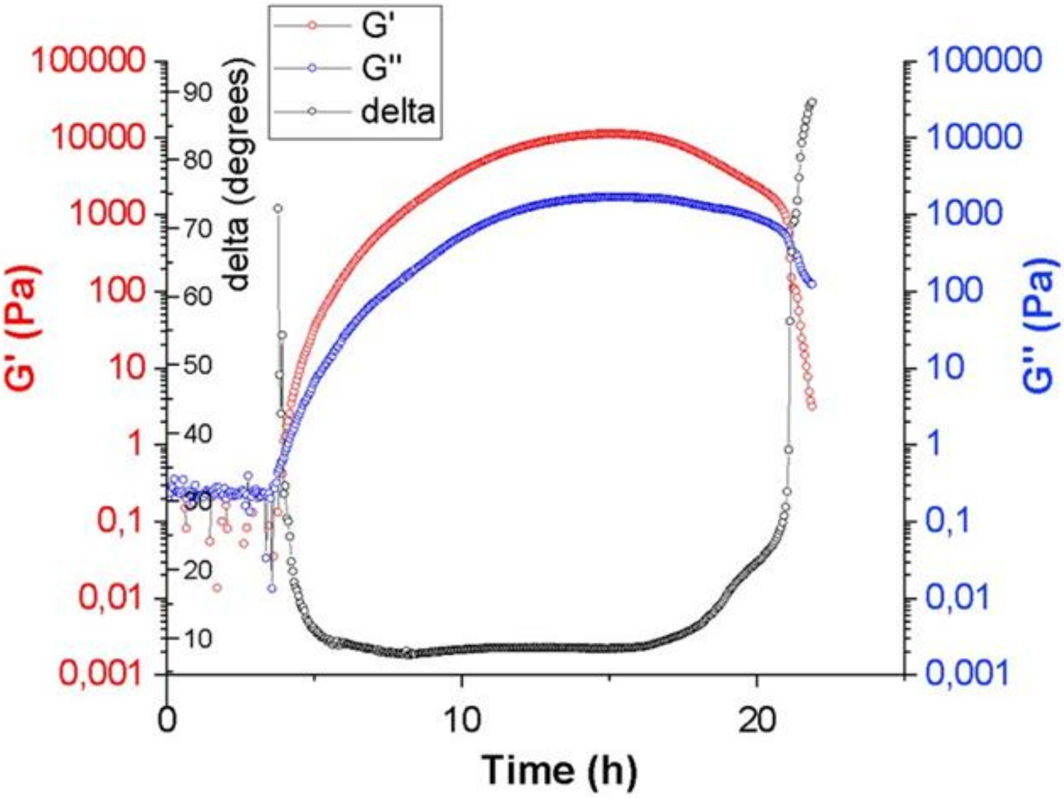

Figure 1: Elastic (G', red), viscous (G", blue) modulus and dephasing (delta, black) of [Zn(Cy)2] – octylamine (OA) mixture over time. The monitoring is started 4 hours after mixing (t = 0 h on the rheogram).

Up to 3h40 after injection in the rheometer, namely 7h40 min after the preparation, both moduli are still low (viscous modulus G'' ≈ 0.25 Pa; elastic modulus G' ≈ 0.15 Pa) with G'' larger than G', which is characteristic of a liquid state.[2] A sharp increase of the elastic modulus G' (from 0.15 to 12000 Pa, 5 orders of magnitude) and viscous G" (from 0.25 to 1700 Pa, 5 orders of magnitude) moduli is measured between 7h40 min and 15h which quantifies the increase of the viscosity. During this transition, G' becomes higher than G'', the elastic behaviour becomes predominant. This highlights the formation of a network with a cross-linking density increasing with time.[2] After 15h, the moduli start to decrease, most probably indicating that the sample began to break. In this case, either the applied shear stress was too high or slipping or separation from the plates occurred. At the end of the experiment, the gap was still adequately filled with a transparent yellowish vitreous solid allowing us to state that the experiment was carried out under conditions that prevented the hydrolysis of the mixture during the measurement. It broke up into platelets with the opening of the gap. The rheological data thus demonstrates that the mixture initially liquid became more and more viscous and then behaves typically like a gel or a glassy material. These results are similar to the one already described for the [Zn(Cy)2] - dodecylamine mixture.[3] Coherent data are unfortunately not obtained for all the systems, as we will see in the next paragraph.

In the case of the [Zn(Cy)$_2$]-hexylamine system, the mixture has been injected in the rheometer at a time close to the expected transition time (after 7h of maturation in the glove box, thus, much later compared with octylamine (4h) and dodecylamine (1h) systems).

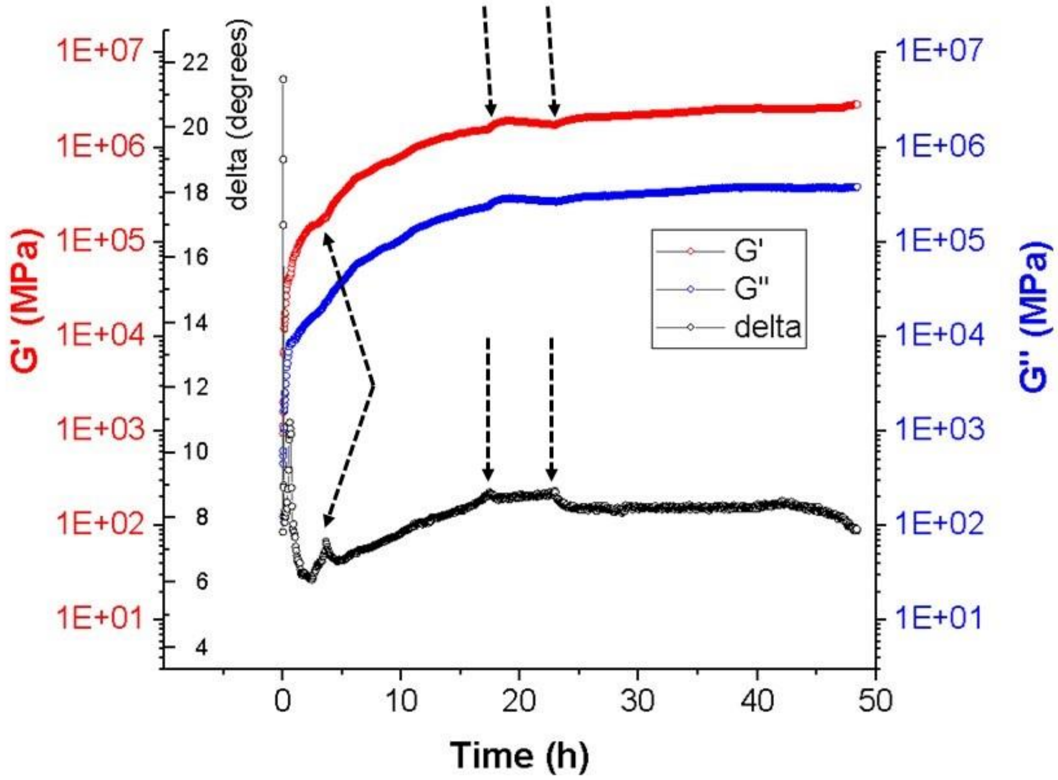

Figure 2: Elastic (G', red), viscous (G", blue) and dephasing (delta, black) of a [Zn(Cy)$_2$] - hexylamine. The monitoring is started 7 hours after mixing for hexylamine (t = 0 h on the rheogram). Other attempts with slightly different conditions of measurement or waiting time before injection gave similar results.

A sharp increase of the moduli (see Figure 2) is observed at the very beginning of the measurement which does not correspond to naked eye observations or NMR measurements (see below). The change is expected to occur around 20h (13h after injection in the rheometer). In the rheometer, the nitrogen flow, even if kept very low, probably flushed out the amine, explaining the abrupt increase of the moduli at the beginning. This effect should be more important with the lower boiling point of hexylamine (bp: 131°C) compared with octylamine (bp: 176°C) or dodecylamine (bp: 259°C). The sharp increase of the moduli hinders the observation of the expected gelation transition. However, several events are observed during the measurement but not understood. A peak on the dephasing curve and an inflexion point on G' curve is observed 3h20 after injection, and two other small changes are observed at 16h30 and 23h20 which may reflect an intrinsic change in the system rheology. It corresponds to, respectively, 10h20, 23h30 and 30h20 after preparation of the mixture. At the end of the measurement, 57h after mixing, a sticky orange-brown paste is observed. It does not change when stirred with a spatula and no liquid is exuded. It slowly becomes a white and thin powder. Rheological data for this system are therefore clearly trickier to obtain and analyse. It's why complementary experiments with NMR have been performed.

4.2 Kinetic study based on Solid state NMR

Magic Angle Spinning (MAS) NMR measurements has been carried out for characterization of the pristine $[Zn(Cy)_2]/RNH_2$ (1:2) mixture as well as to follow in a molecular level the gelation process. Indeed, ^{13}C signal intensities obtained using cross- (CP) and INEPT- polarization transfer sequences yield information on the local dynamics of the alkyl chain: the CP and INEPT sequences edit molecular segments being respectively rigid or mobile.[4] [5] Note that unlike rheology measurements, NMR spectroscopy allows sample preparation and measurement in a controlled atmosphere. The sealed rotors can be prepared in a glove box to protect the reaction medium from humidity. Measurements are made therefore easier. This allows the probing of shorter aliphatic chain lengths without changing the stoichiometry of the system being measured. Thus, we not only studied the same mixtures as for the rheology measurements, namely $[Zn(Cy)_2]$/DDA, $[Zn(Cy)_2]$/OA and $[Zn(Cy)_2]$/HA (hexylamine), but we were also able to extend the study to the $[Zn(Cy)_2]$/HPA (heptylamine) system and remarkably also to the system with a chain length as short as pentylamine (PA).

Whatever the length of the alkyl chain, there is always a period of time when no signal is detected in the ^{13}C CP-MAS experiments (Figures 3 top and 4-5) while strong ^{13}C signals are observed in the ^{13}C INEPT-MAS experiments (Figures 3 bottom and 6-7). These results indicate that at the beginning, the $[Zn(Cy)_2]/ RNH_2$ (1:2) mixture is a liquid with highly mobile molecules. The ^{13}C INEPT-MAS signals has been previously assigned to amine, $[Zn(Cy)_2]$, cyclohexane and a mixture of monomeric and dimeric Zn amido complexes as well as small Zn amido oligomers. The intensity of the ^{13}C resonance of the cyclohexane ($\delta = 26.2$ ppm) observed in the ^{13}C INEPT-MAS spectra increases over time indicating the replacement of the Zn coordinated cyclohexyl groups by amido groups. This replacement rate is very similar regardless of the alkyl chain length and a plateau is reached after about 8 h (Figure 8).

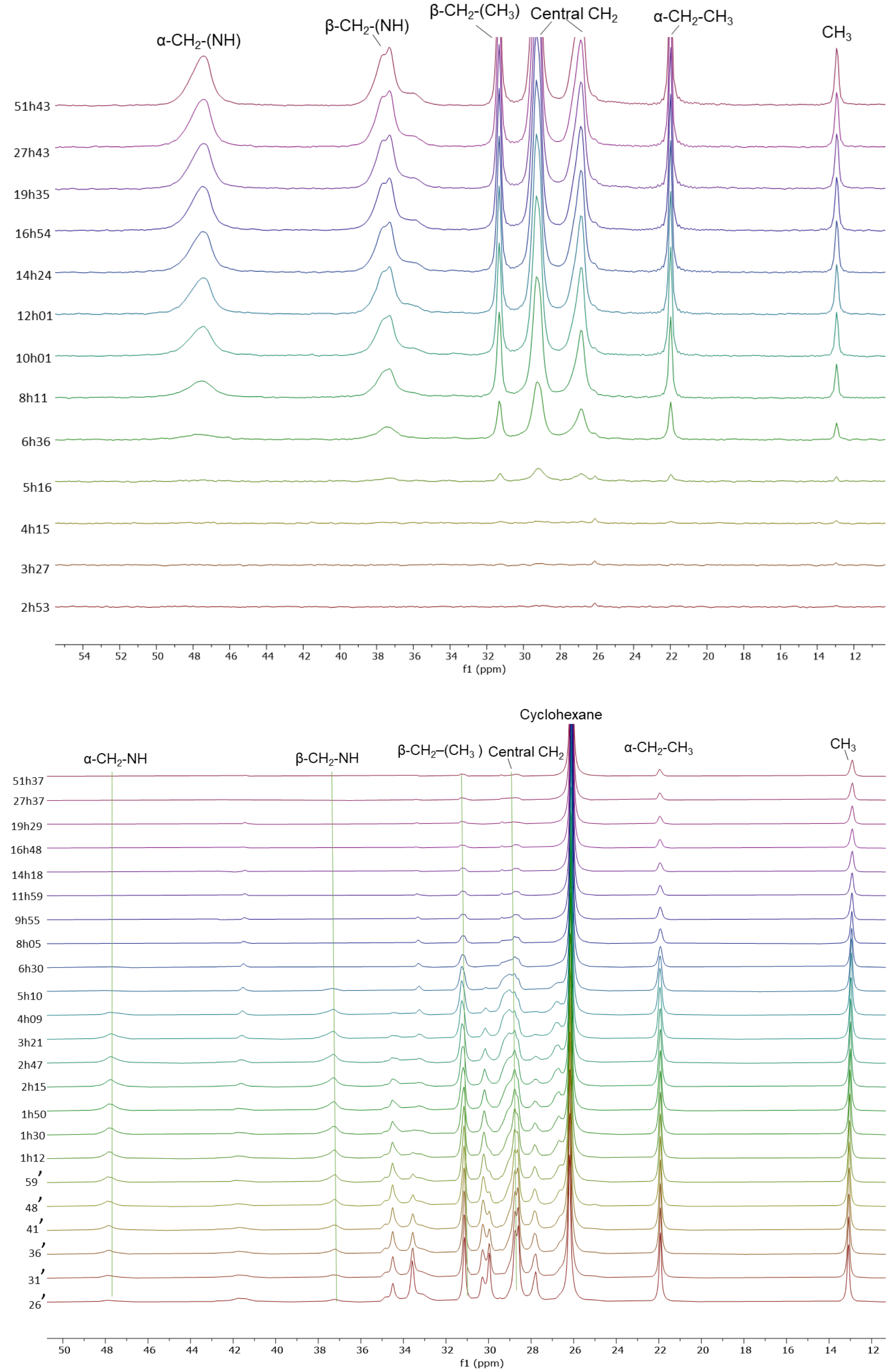

Figure 3: ^{13}C CP (top) and INEPT (bottom)-MAS experiments of the [Zn(Cy)$_2$]/OA (C8) (1:2) mixture over time.

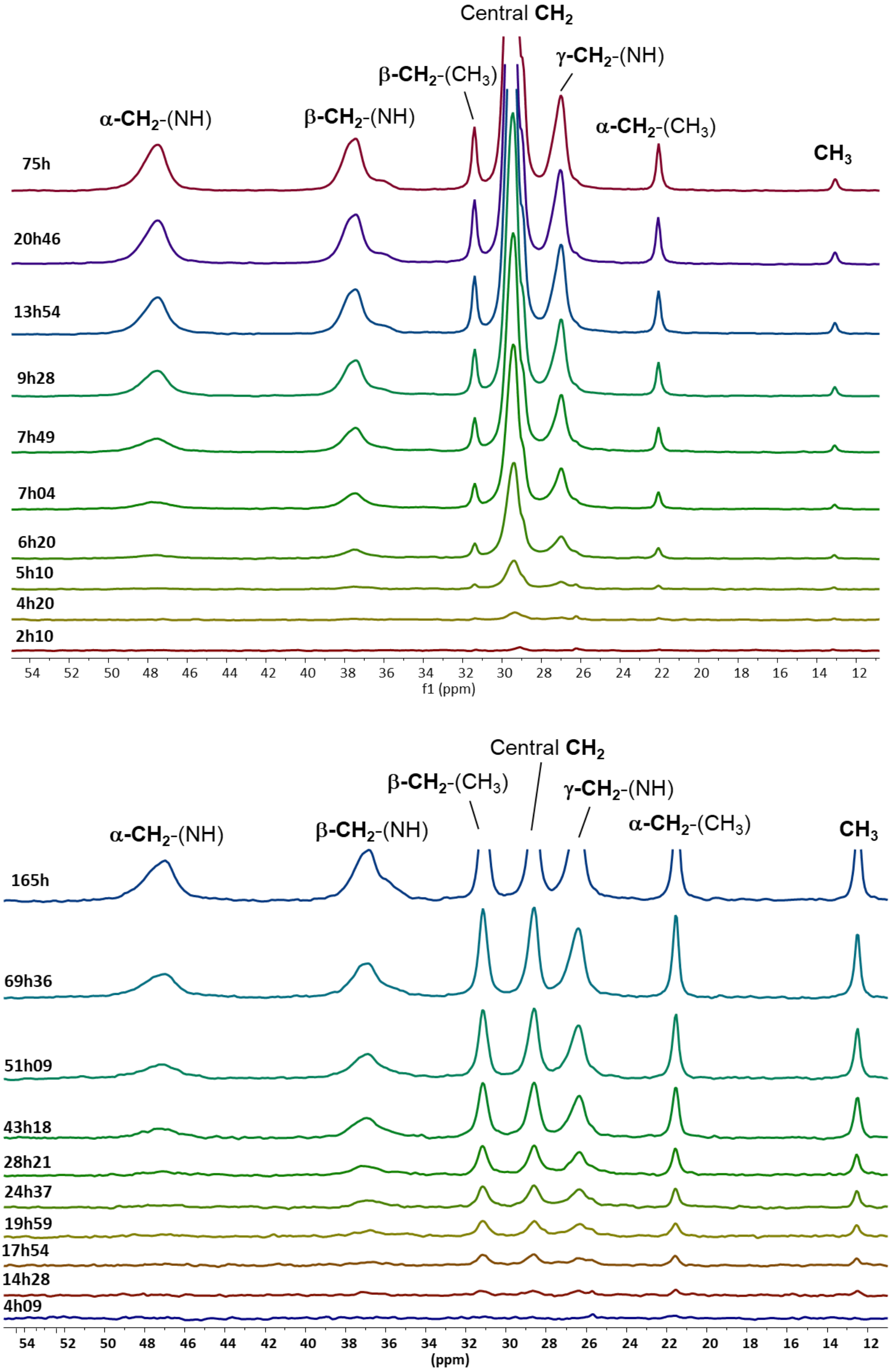

Figure 4: ^{13}C CP-MAS experiments of the [Zn(Cy)$_2$]/Amine (1:2) mixture over time. Top: DDA amine (C12). Bottom: HPA amine (C7)

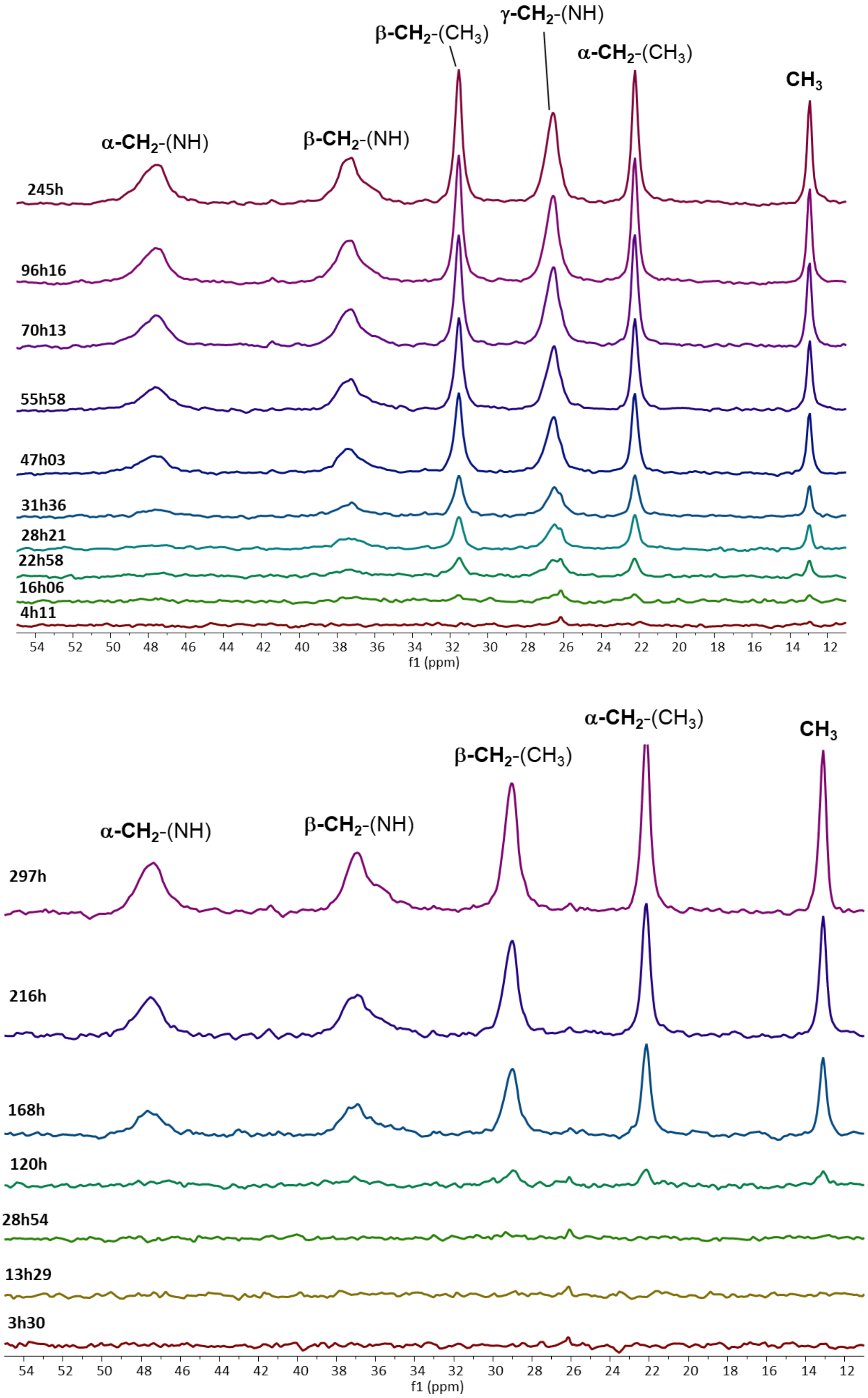

Figure 5: ^{13}C CP-MAS experiments of the [Zn(Cy)$_2$]/Amine (1:2) mixture over time. Top: HA amine (C6). Bottom: PA amine (C5)

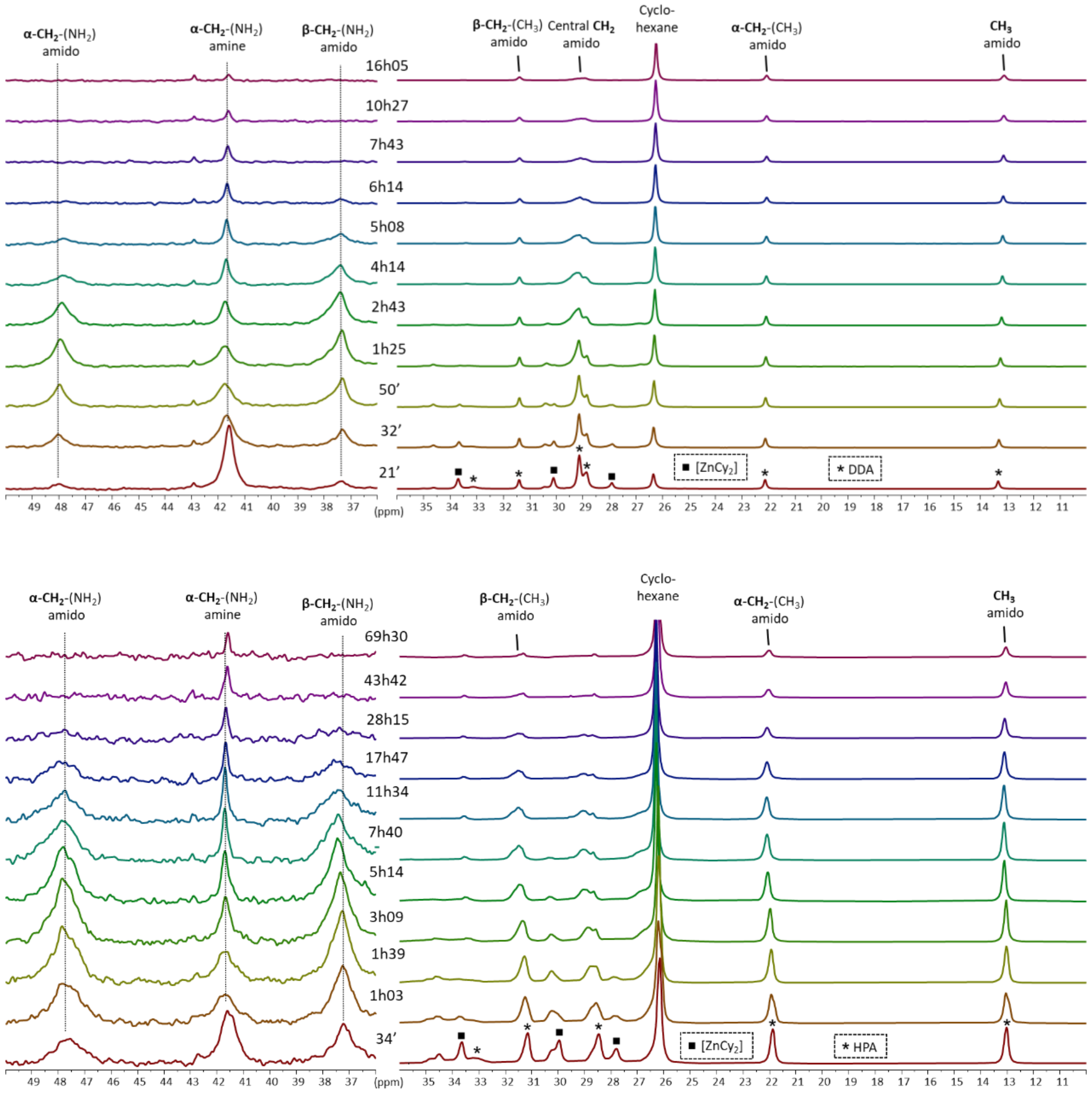

Figure 6: ^{13}C INEPT-MAS experiments of the [Zn(Cy)$_2$]/amine (1:2) mixture over time. Top: DDA amine (C12). Bottom: HPA amine (C7)

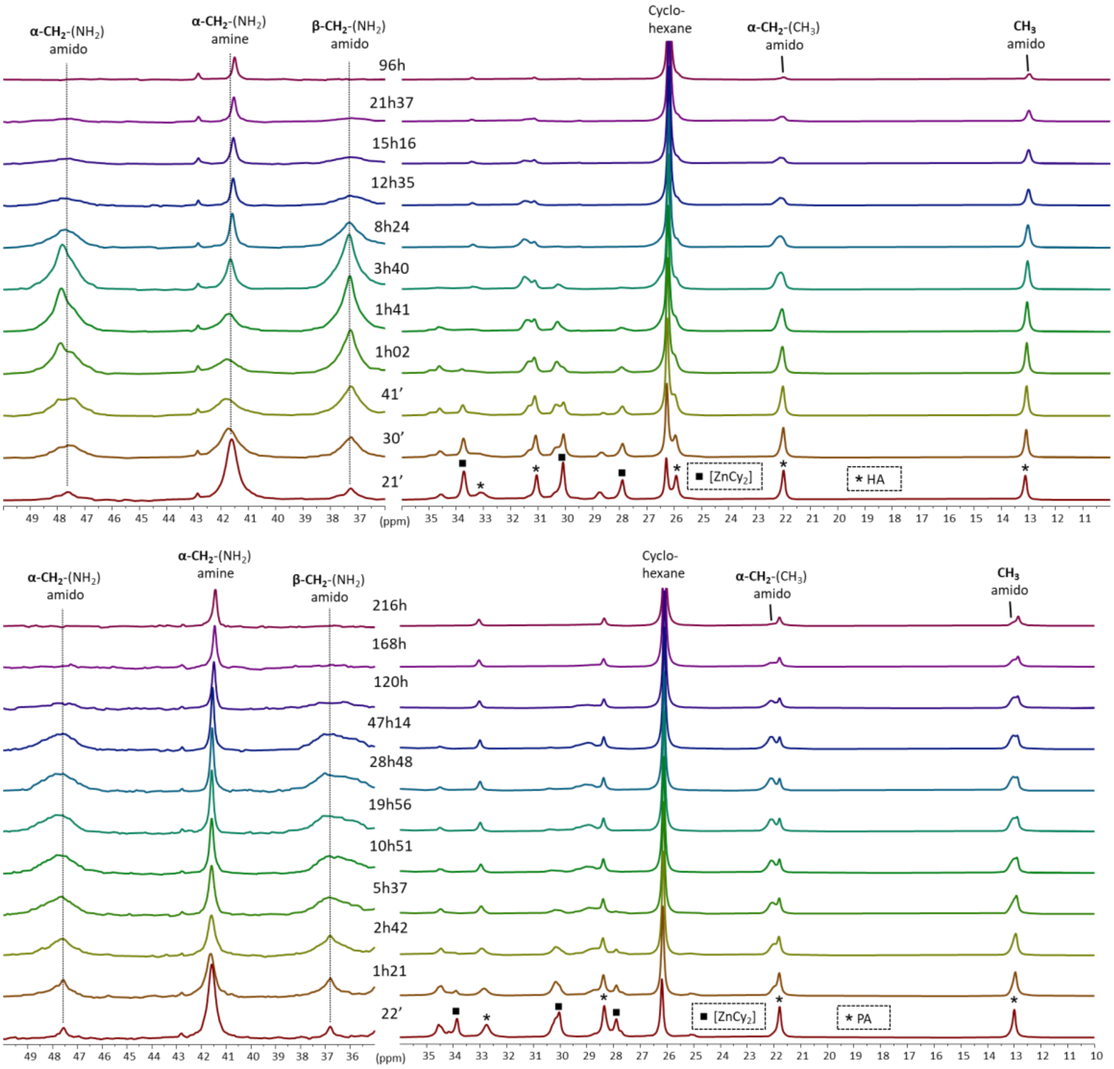

Figure 7: ^{13}C INEPT-MAS experiments of the $[Zn(Cy)_2]$/amine (1:2) mixture over time. Top: HA amine (C6). Bottom: PA amine (C5)

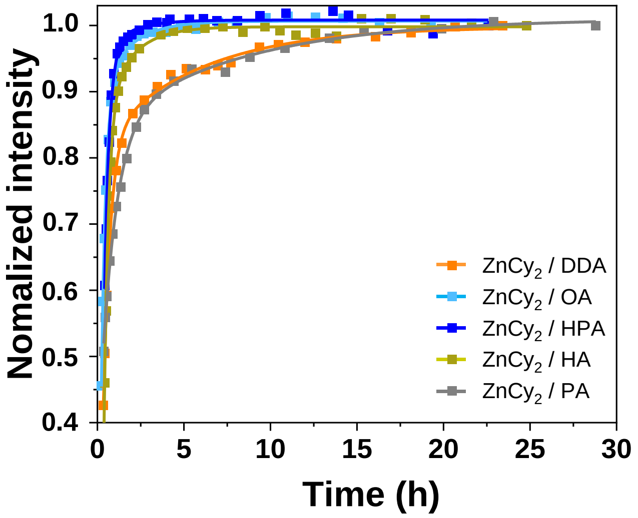

Figure 8: Comparison of the evolution of ^{13}C signal intensity (normalized) of the cyclohexane over time for the different alkylamines. (Lines are just guided for eyes.)

Additionally, the intensities of the characteristic ^{13}C resonances of the Zn amido species observed in the ^{13}C INEPT-MAS spectra at ca. 47.7 and ca 37.3 ppm begin to increase over time until the signals associated to $[Zn(Cy)_2]$ disappear, and then slowly decrease up to their total disappearance. Then, signals of some mobile alkylamine groups can still be detected in the ^{13}C INEPT-MAS. Concomitantly, ^{13}C signals of Zn amido oligomers start to appear in the CP-MAS spectra with their intensities increasing over time up to a certain level (Figures 6-7). These results indicate a rigidification of the alkyl chain of Zn amido oligomers over time. Furthermore, we can note that at the end of the oligomerization, the ^{13}C CP-MAS signal of the carbon close the CH_3 group are weaker than the ones at the center of the alkyl chain or close to the NH group and that the reverse is observed for the ^{13}C INEPT-MAS. These differences are however getting weaker as alkyl chains become smaller. This indicates an increase of the mobility of the methyl alkyl chain extremity for the longest alkyl chains.

Contrary to the release of the cyclohexane, the rates of disappearance of the ^{13}C INEPT signals and of growth of the ^{13}C CP signals of the Zn amido species clearly depend on the alkyl chain length. Regardless of the alkyl chain length, the evolution of the CP signals over time show a sigmoidal growth (Figure 9).[6]

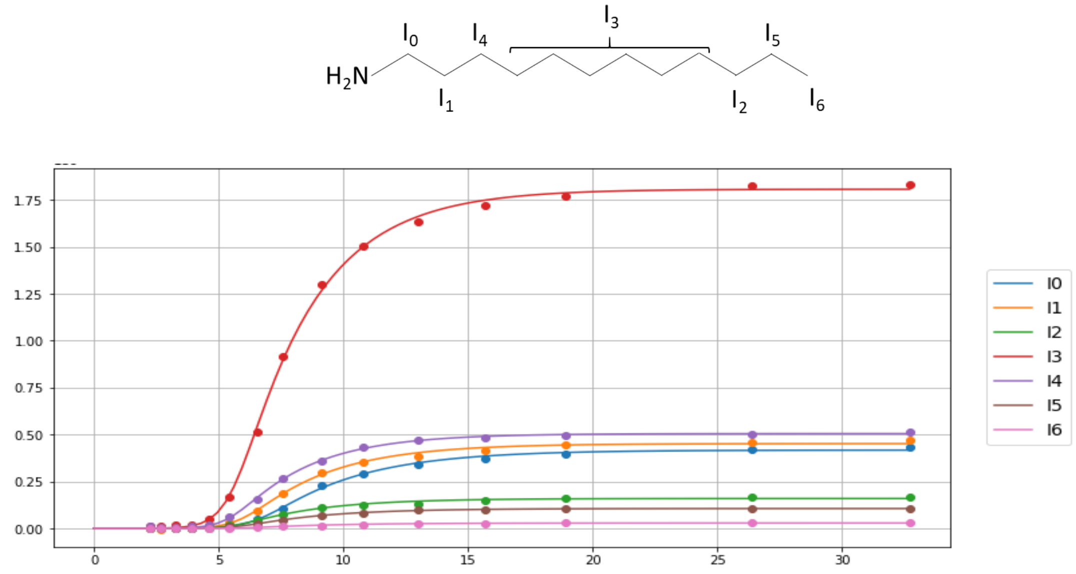

Figure 9. Example of ^{13}C CP-MAS experiments for the $[Zn(Cy)_2]$/DDA (1:2) mixture. Evolution of the integrals (a.u.) of various NMR peaks versus time (in hours). Top: structure of the DDA and assignments of the different integrals I_n.

To fit these experimental curves, a phenomenological model derived from the Finke−Watzky[6] one but including inhibition phenomena (such as steric hindrance) has been used. Each signal is therefore fitted with the following equation:

$$A_0\left(1-\left(\frac{A_0k_2+k_1}{A_0k_2+k_1e^{t(A_0k_2+k_1)}}\right)^{ni}\right)$$

where:

A_0 is a constant associated to the maximum value of the signal
ni ranges between 0 and 1. The lower ni, the higher the inhibition phenomena it is.
k_1 and k_2 are two kinetic constants.

Whatever the exact meaning of these constants in the model used in this paper, we used this equation to characterize the experimental sigmoid through the following parameters:

1. t_{max}, time of the inflection point,

$$t_{max} = \frac{\log\left(\frac{A_0k_2}{k_1ni}\right)}{A_0k_2+k_1}$$

2. maxSlope or S_{stiff}, relative rate at the inflection point,

$$maxSlope = A_0k_2\left(\frac{A_0k_2+k_1}{A_0k_2+\frac{A_0k_2}{ni}}\right)^{ni+1}$$

3. $A(t_{max})/A_0$, relative intensity at the inflection point,

$$\frac{A(t_{max})}{A_0} = 1-\left(\frac{A_0k_2+k_1}{A_0k_2+\frac{A_0k_2}{ni}}\right)^{ni}$$

4. $t_{induction}$, induction period obtained from the third derivative,

$$t_{induction} = \frac{\log\left(\frac{A_0k_2\left(3ni-\sqrt{5ni^2+6ni+1}+1\right)}{2k_1ni^2}\right)}{A_0k_2+k_1}$$

5. $t_{inhibition}$, inhibition period obtained from the third derivative.

$$t_{inhibition} = \frac{\log\left(\frac{A_0k_2\left(3ni+\sqrt{5ni^2+6ni+1}+1\right)}{2k_1ni^2}\right)}{A_0k_2+k_1}$$

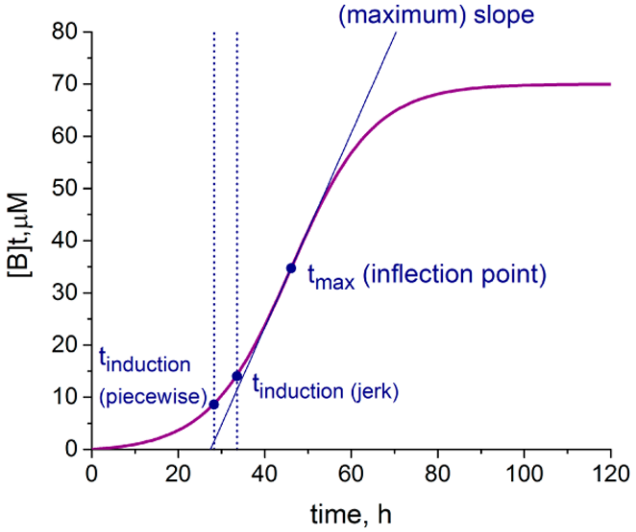

Figure 10. Position of t_{max} (time of the inflection point), maxSlope (relative rate at the

inflection point), $t_{induction}$ (induction period obtained from the third derivative) on the sigmoid.[6]

Figure 10 extracted from the reference [6] illustrates some of the previous parameters.

Table 1 summarize the main results including the induction time (t_{ind}) i.e. the time it takes for the system to start presenting reduced mobility molecules, the time associated to the inflection point (t_{max}) and the associated relative rate (S_{stiff}), i.e. the time required for half of the molecules to have reduced mobility and the instantaneous speed associated with the stiffening phenomenon, and the inhibition time (t_{inhib}) i.e. the time after which the system no longer evolves.

For these data, we extracted the average values of the parameters for each molecular system (see Table 2).

Table 1. Full analysis of the data using the previous equation.

Sample name	Signal	S_{stiff} (h^{-1})	t_{max} (h)	t_{ind} (h)	t_{inhib} (h)
$[Zn(Cy)_2]$/DDA	α-NH_2	0.17	7.7	6.3	9.0
	β-NH_2	0.19	6.9	5.7	8.1
	β-CH_3	0.20	6.6	5.5	7.8
	Central-CH_2	0.21	6.5	5.4	7.6
	γ-NH_2	0.21	6.4	5.3	7.5
	α-CH_3	0.19	6.8	5.6	8.0
	CH_3	0.19	7.1	5.9	8.3
$[Zn(Cy)_2]$/OA	α-NH_2	0.18	7.2	5.9	8.5
	β-NH_2	0.19	6.7	5.5	7.9
	β-CH_3	0.21	6.3	5.2	7.4
	Central-CH_2	0.21	6.2	5.1	7.3
	γ-NH_2	0.21	6.2	5.1	7.3
	α-CH_3	0.20	6.5	5.4	7.7
	CH_3	0.18	6.9	5.7	8.2
$[Zn(Cy)_2]$/HPA	α-NH_2	0.01	28.2	17.7	38.7
	β-NH_2	0.02	23.0	14.7	31.3
	β-CH_3	0.02	19.9	12.9	27.0
	Central-CH_2	0.02	20.4	13.1	27.6
	γ-NH_2	0.02	19.5	12.6	26.3
	α-CH_3	0.02	20.6	13.2	27.9
	CH_3	0.02	20.9	13.4	28.3
$[Zn(Cy)_2]$/HA	α-NH_2	0.02	33.8	19.3	48.3
	β-NH_2	0.02	28.3	16.7	39.9
	β-CH_3	0.02	26.7	15.9	37.5
	γ-NH_2	0.02	25.3	15.2	35.4
	α-CH_3	0.02	28.0	16.6	39.5
	CH_3	0.02	30.2	17.6	42.7
$[Zn(Cy)_2]$/PA	α-NH_2	0.01	116	110	123
	β-NH_2	0.01	114	108	121
	γ-NH_2	0.01	113	106	119
	α-CH_3	0.01	115	109	122
	CH_3	0.01	112	106	119

Table 2. Average values of the parameters for each chemical system: mean (SD).

Sample name	S_{stiff} (h^{-1})	t_{max} (h)	t_{ind} (h)	t_{inhib} (h)
$[Zn(Cy)_2]$/DDA	0.19 (0.01)	6.9 (0.4)	5.7 (0.3)	8.0 (0.5)
$[Zn(Cy)_2]$/OA	0.20 (0.01)	6.6 (0.4)	5.4 (0.3)	7.8 (0.5)
$[Zn(Cy)_2]$/HPA	0.02 (0.004)	21.8 (3.0)	13.9 (1.8)	30.0 (4.3)
$[Zn(Cy)_2]$/HA	0.02 (0)	28.7 (3.0)	16.9 (1.4)	40.6 (4.5)
$[Zn(Cy)_2]$/PA	0.01 (0)	114 (1.6)	107.8 (1.8)	120.8 (1.8)

Several important pieces of information can be extracted from Table 2. Firstly, we can see that as the length of the aliphatic chain increases, the gelation time decreases. More precisely, three groups appear. The first group contain the longest alkyl chain length, namely $[Zn(Cy)_2]$/DDA and $[Zn(Cy)_2]$/OA for which the gelation time is around 7h (t_{max}). As the chain length reaches C7 and C6, i.e. for $[Zn(Cy)_2]$/HPA and $[Zn(Cy)_2]$/HA a gelation time between 20 and 30 h is measured. Finally, for the shortest chain length C5, $[Zn(Cy)_2]$/PA system, a significant increase of the gelation time, over 100 hours, is observed.

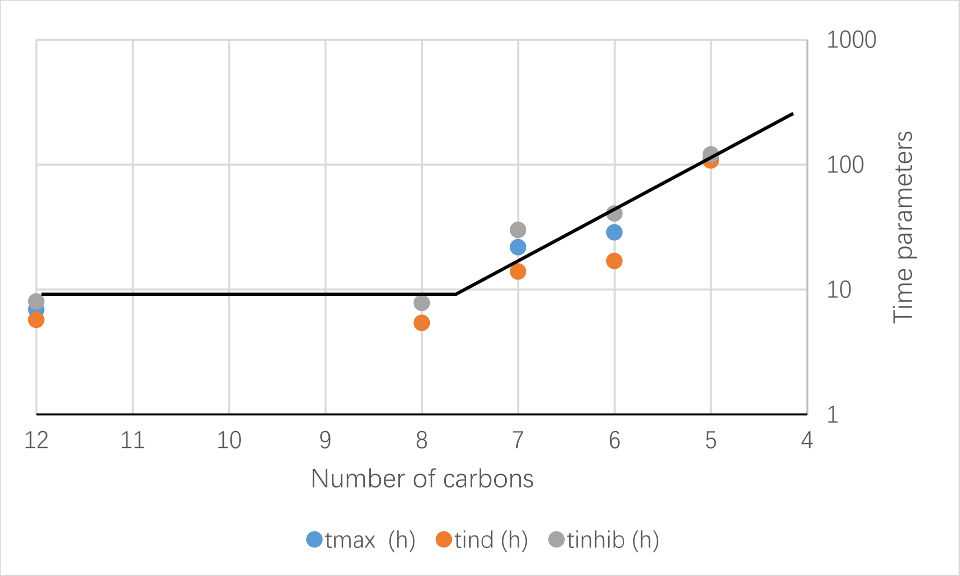

Figure 11. Evolution of the time parameters (in logarithm) versus the number of carbon of the amine.

As seen in Figure 11, when the number of carbons in the alkyl tail is lower than 8, a linear increase of the logarithm of the time parameters is observed versus the number of carbon. This suggests, for example, that with butylamine (C4) the gelification should theoretically start around 170h and around 400h for the propylamine (C3).

At the molecular level, the values of t_{max} differ from one carbon atom to another (see Table 1) but this variation is similar for the three characteristic time (t_{max}, t_{ind}, and t_{inhib}). In other words, the characteristic time at which the C atoms associated with a signal begin to decrease in mobility, are 50% frozen or completely rigid depends on the position of the atoms in the chain. For a given chain length, the value of S_{stiff} is similar whatever the position of the carbon atoms in the alkyl chain. In other words, all the carbon atoms in the alkyl chain have an instantaneous speed associated with t_{max} comparable. It means that as soon as the C atoms start to stiffen, they do so at the same rate. A more focused look at these results highlights that the order in which the different carbon atoms become rigid is however surprising. Interestingly, the rigidification starts always first on the center of the alkyl chain while it is a bit delayed for the carbons in alpha- and beta- position of the nitrogen and for the terminal methyl groups. These results suggest that stiffening of the system takes place first from the aliphatic chains before the inorganic Zn-amido backbone. This rigidification may be therefore due to intermolecular van der waals interactions between the alkyl chains of the amines. This remains unexpectedly true up to very short aliphatic chains and makes it possible to distinguish that the driving force of gelation of the system is first the van der waals interactions, before the oligomerization of the inorganic skeleton by the formation of coordination bonds between the Zn atoms and the nitrogen atoms of the amine group.

4.3 Conclusion

In this part, we were able, thanks to the coupling between macroscopic rheology measurements and molecular NMR measurements, to show that the gelation mechanism of the $[Zn(Cy)_2]$ organometallic precursor and a primary alkyl amine came firstly from the rigidification of the aliphatic chains of the amine, which takes precedence over the oligomerization of the inorganic backbone formed by the acid-base reaction, giving rise to Zn-amido type coordination bonds. This result highlights that the rheological properties of organometallic gels, precursors to the shaping of metal oxide nanomaterials, can be controlled by the length of the aliphatic chain of the amine. The longer the aliphatic chain, the faster the gelation. This is a simple way to tune the rheological properties of these promising systems.

References

[1] A. W. Ralston, W. M. Selby, W. O. Pool, R. H. Potts, “Boiling Points of Alkyl Primary Amines”, J. Ind. Eng. Chem , **1940**, *32*, 1093-1094.

[2] T. Mezger, “The rheology handbook”, Vincentz Network, **2020**.

[3] Z. Zhao, Y. Coppel, J. Fitremann, P. Fau, C. Roux, C. Lepetit, P. Lecante, J.-D. Marty, C. Mingotaud and M. L. Kahn, “Mixing Time between Organometallic Precursor and Ligand: A Key Parameter Controlling ZnO Nanoparticle Size and Shape and Processable Hybrid Materials”, *Chem. Mater.*, **2018**, *30*, 8959–8967.

[4] D. E. Warschawski, P. F. Devaux, “^{1}H–^{13}C polarization transfer in membranes: a tool for probing lipid dynamics and the effect of cholesterol”, J*. Magn. Reson.*, **2005**, *177*, 166-171.

[5] F. M. Mulder, W. Heinen, M. van Duin, J. Lugtenburg, H. J. M. de Groot, “Spin Diffusion with ^{13}C Selection and Detection for the Characterization of Morphology in Labeled Polymer Blends with MAS NMR” *J. Am. Chem. Soc.* **1998,** *120,* 12891-12894.

[6] L. Bentea, M. A. Watzky, R. G. Finke, “Sigmoidal nucleation and growth curves across nature fit by the Finke–Watzky model of slow continuous nucleation and autocatalytic growth: explicit formulas for the lag and growth time plus other key insights”, The Journal of Physical Chemistry C 2017 121 (9), 5302-5312.

Partie Expérimentale

I. Matériaux, réactifs et équipements

Tous les composés sensibles à l'oxygène et à l'eau ont été manipulés dans une boîte à gants MBraun sous argon. Le précurseur de zinc [Zn(C_6H_{11})$_2$] (noté [Zn(Cy)$_2$]) a été acheté chez Nanomeps (http://www.nanomeps.fr). Les amines primaires, à savoir la dodécylamine (DDA), l'octylamine (OA), l'heptylamine (HPA), l'hexylamine (HA), la pentylamine (PA), ont été achetées chez Aldrich, et les amines secondaire (N-Méthyldodécylamine, C_{12} NH(CH_3)) et tertiaire (N, N - Diméthyldodécylamine, C_{12}-N(CH_3)$_2$) ont été achetées chez Alfa Aesar. Stockées dans une boîte à gants ont été utilisés sans purification supplémentaire. Le THF a été prélevé dans un purificateur MBraun. La teneur en eau résiduelle du solvant a été systématiquement mesurée par titrage coulométrique de type Karl Fischer en utilisant un équipement Metrohm (moins de 10 ppm pour 0,8 ml de solvant). Tous les processus de mélange ont été réalisés dans une boîte à gants. Les étapes d'hydrolyse ont été effectuées à l'extérieur de cette boîte à gants et réalisées avec une ligne de vide standard sous une atmosphère d'argon.

Microscopie électronique à transmission

Les échantillons pour l'analyse MET ont été préparés par évaporation lente de gouttelettes de solutions colloïdales déposées sur des grilles de cuivre avec film de carbone. Les échantillons ont été soigneusement séchés pendant une nuit sous une pression de $5*10^{-5}$ mbar en utilisant une pompe turbo moléculaire BOC Edward. Les expériences de MET ont été réalisées avec un microscope électronique JEOL JEM1011 fonctionnant à 100 kV avec une résolution de 0,45 nm. Le logiciel Image J (https://imagej.nih.gov/ij/index.html) a été utilisé manuellement ou avec une macro afin d'extraire la largeur et la longueur des nano-objets dans les différentes micrographies. La macro est basée sur la macro PSA, disponible sur http://code.-google.com/p/psa-macro. Les nanoparticules qui se chevauchent sont automatiquement rejetées pour l'analyse statistique. Les histogrammes de distribution de la taille des nanoparticules ont été déterminés en utilisant des images MET. Pour chaque échantillon, la distribution de la taille des particules a été déterminée en mesurant un minimum de 200 particules. Les histogrammes ont été généralement analysés à l'aide de graphiques 2D. Ces graphiques sont un type de méthodologie qui permet une analyse statistique multivariée et l’extraction des corrélations entre les largeurs et les longueurs d'objets anisotropes.[1]

Résonance magnétique nucléaire

RMN à l'état liquide : des expériences de RMN ^{1}H 1D et 2D ont été effectuées sur un spectromètre Bruker Avance 600 NEO équipé d'une sonde à triple résonance à gradient Z inverse de 5 mm. Le solvant utilisé était le toluène-d^8. Toutes les mesures de diffusion ont été effectuées en utilisant la séquence d'impulsions d'écho stimulé avec des impulsions de gradient bipolaires. Les expériences de RMN 1D ^{17}O ont été réalisées avec des délais de récupération de 0.2 s. Les mesures de K_a ont été effectuées à partir d'un titrage RMN ^{1}H en suivant l'évolution du déplacement chimique des résonances de $[Zn(Cy)_2]$. La concentration de $[Zn(Cy)_2]$ a été maintenue constante en présence de concentrations croissantes d'amine (avec un rapport de concentration de 0 à environ 15 équivalents). Les K_a ont été extraits de l'ajustement de l'évolution des déplacements chimiques avec l'équation ci-dessous:[2]

$$\Delta\delta = \ \delta_{\Delta HG}\left(\frac{0.5\left\{\left([H]_0+[G]_0+{}^1\!/_{K_a}\right)-\sqrt{\left([H]_0+[G]_0+{}^1\!/_{K_a}\right)^2-4[H]_0[G]_0}\right\}}{[H]_0}\right)$$

où $[H]_0$ et $[G]_0$ sont la concentration totale de l'hôte ($[Zn(Cy)_2]$) et de l'invité (amine) et $\delta_{\Delta HG}$ est la différence de déplacement chimique entre l'hôte libre et le complexe hôte-invité (HG).

RMN à l'état solide : les expériences de RMN à l'état solide ont été enregistrées sur un spectromètre Bruker Avance III 400. Les échantillons ont été placés dans des rotors en zircone de 4 mm dans une boîte à gants. Les rotors ont été mis en rotation à 5 kHz à 293K. Les MAS ^{13}C avec polarisation croisée (CP) ont été enregistrés avec un délai de recyclage de 2 s et un temps de contact de 2 ms. Les MAS ^{13}C avec Insensitive Nuclei Enhanced by Polarization Transfer (INEPT) ont été enregistrés avec un délai de recyclage de 3 s. Les déplacements chimiques ^{1}H et ^{13}C sont analysés par rapport à la référence TMS et les déplacements chimiques ^{17}O par rapport à l'eau.

Diffraction des rayons X

Les mesures de XRD des rayons X sur poudre (PXRD) ont été réalisées à température ambiante sur un diffractomètre le miniflex 600 (rigaku) fonctionnant sous rayonnement Cu K_α, équipé d'un système de détection de compteurs de scintillation à grande surface. Les données ont été recueillies entre 15° et 90° (θ) avec un pas de 0,01 Å et un temps de comptage de 1 s par pas.

Mise en place expérimentale pour la mesure de rhéologie

Le module élastique (G′) et le module visqueux (G″) ont été mesurés avec un rhéomètre AR1000 équipé d'un four (TA Instrument). Un flux d'azote (0,2 bar) était assurée à l'intérieur du four pendant toute la durée de l'expérience. La mesure a été effectuée avec une géométrie à plaque de 25 mm (aluminium), et l'entrefer a été réglé à 500 µm. Un cylindre en plastique supplémentaire a été placé autour de la géométrie pour éviter le séchage de l'échantillon dû au flux de gaz. La température était de 20 °C. Les mesures ont été effectuées en suivant le même protocole que celui décrit pour le mélange $[Zn(Cy)_2]$/DDA.[3]

Pour l'octylamine: le mélange a été préparé dans une boîte à gants sous argon et stocké dans une seringue elle-même dans un flacon Schlenk sous argon. Après 4 h de repos dans la seringue, le mélange a été injecté entre les plaques du rhéomètre (380 µL sont injectés, l'espace entre les deux plaques pendant l'injection est réglé à 1500 µm, le four est juste légèrement ouvert pour éviter au maximum l'entrée d'air, le cylindre en plastique est soulevé pendant l'opération). Lorsque l'injection est terminée, l'écart est réglé à 500 µm, le cylindre est placé de manière à ne pas toucher la plaque mobile et le four est fermé. Les valeurs des modules G′ et G″ ont été mesurées en appliquant une contrainte sinusoïdale à l'échantillon, à une fréquence de 1 Hz, et la déformation sinusoïdale résultante a été enregistrée. En raison de la très grande variation de la viscosité au cours de l'expérience, la contrainte appliquée a dû être adaptée au cours de l'expérience. L'amplitude de la contrainte est multipliée par 10 lorsque la déformation descend en dessous de 0,06 %. L'amplitude de la contrainte a été modifiée de cette manière par petits pas afin d'éviter la rupture de la structure et la séparation de l'échantillon des plaques. Une amplitude de contrainte de 0,1 Pa a été appliquée de 0 à 6 h de mesure ; 1 Pa de 6 à 8,5h ; 10 Pa de 8,5 à 10,75h ; 100 Pa de 10,75 à 22h.

Pour l'hexylamine : les pas d'amplitude de contrainte sur 50h de mesure sont 0,1/0,5/1/2,5/5/10/25/50/75/100/250/500/750/1000/2500/5000/10000 Pa, avec commutation automatique lorsque la déformation est < 0,06%.

II. Préparation, synthèse et les résultats

Chapitre II

Préparation et synthèse

Toutes les synthèses ci-dessous ont été réalisées à température ambiante.

Etude de la taille des NPs de ZnO en fonction du temps d'hydrolyse. Dans une boîte à gants, 57,9 mg de [Zn(Cy)$_2$] ont été ajoutés dans un flacon en verre de 4 mL à 92,7 mg de DDA. Après mélange complet, le flacon a été retiré de la boîte à gants (le temps de résidence dans la boîte à gants est de 10 minutes) et exposé à l'air. Des analyses MET ont ensuite été réalisées à différents temps de réaction.

Influence du temps de gélification sur la taille des NPs de ZnO. 57.9 mg de [Zn(Cy)$_2$] ont été mélangés dans un flacon en verre de 4 mL à 92.7 mg de DDA. Après mélange complet, le mélange a été gardé dans la boîte à gants. Les échantillons ont été retirés de la boîte à gants à différents moments et exposés à l'air pendant 3 jours.

Etude de la taille des NPs de ZnO en fonction de la température. Dans la boîte à gants, dans un flacon de 4 mL, 57.9 mg de [Zn(Cy)$_2$] ont été ajoutés à 92.7 mg de DDA. Après mélange complet (le temps de résidence dans la boîte à gants est de 10 minutes), les fioles ont été retirées, maintenues à la température choisie (30 °C, 60 °C, 90 °C, 120 °C en bain d'huile) et exposées à l'air pendant 3 jours.

Etude de la taille des NPs de ZnO en fonction de la longueur des tubes. 57.9 mg de [Zn(Cy)$_2$] ont été ajoutés à 92.7 mg de DDA dans un flacon en verre de 4 mL avec des tubes PTFE de différentes longueurs (de 0 à 7 cm). Après mélange complet (le temps de résidence dans la boîte à gants est de 10 minutes), le flacon a été sorti de la boîte à gants et exposé à l'air libre pendant 1 semaine.

Etude de la taille des NPs de ZnO en fonction de la teneur en eau. 57,9 mg de [Zn(Cy)$_2$] ont été ajoutés dans un flacon en verre de 4 mL à 92,7 mg de DDA. Après un mélange complet (le temps de résidence dans la boîte à gants est de 10 minutes), le flacon a été placé dans un réacteur maison qui a permis la diffusion lente de l'eau dans l'échantillon. Différentes quantités d'eau dégazée ont été injectées dans le réacteur. Après 3 jours, des poudres luminescentes blanches ont été obtenues et analysées par

MET.

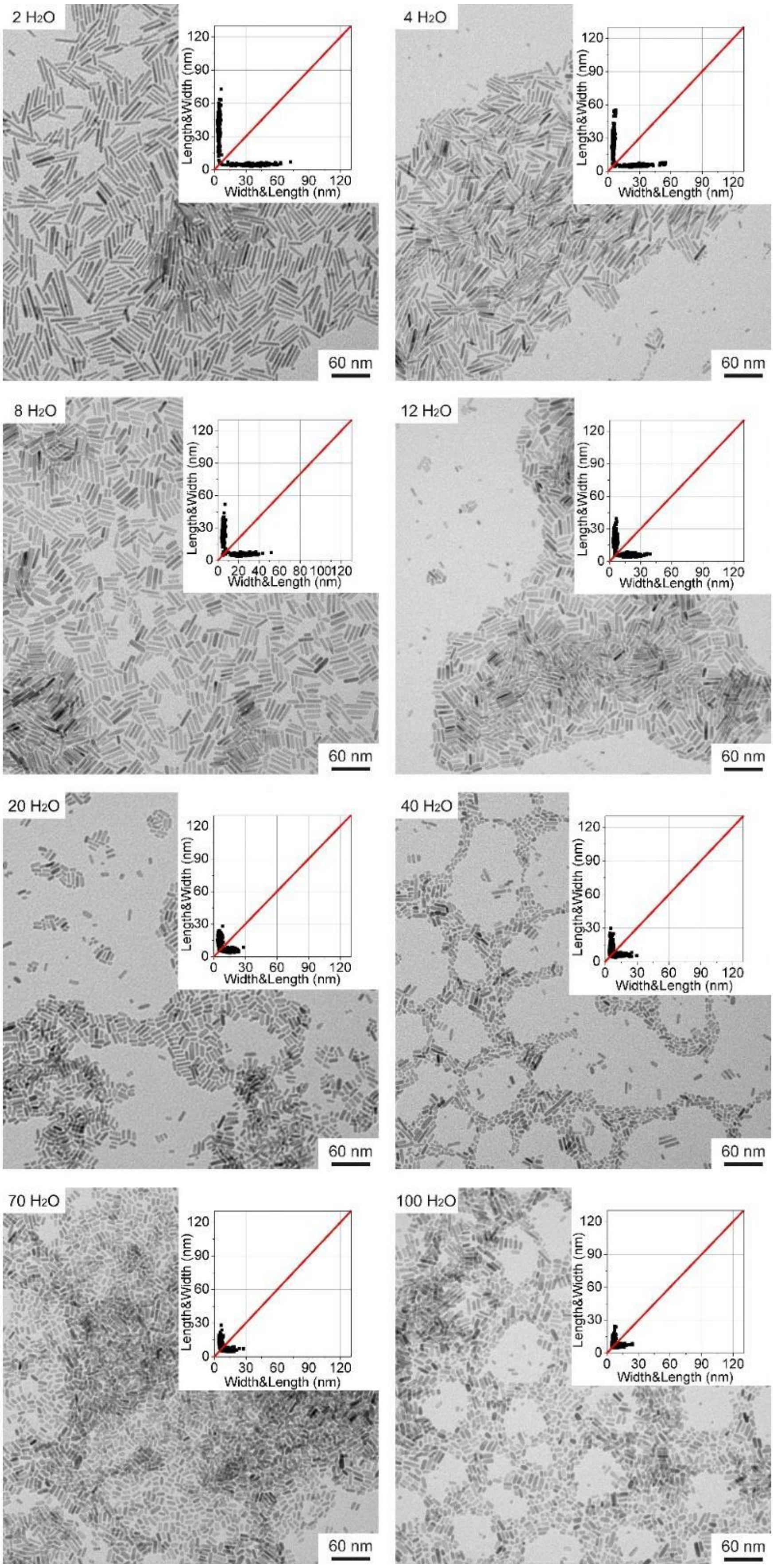
2 H2O
4 H2O
8 H2O
12 H2O
20 H2O
40 H2O
70 H2O
100 H2O
Length&Width (nm)
Width&Length (nm)
0
30
60
90
120
0
20
40
60
80
100
120
60 nm

Figure 1. TEM pictures and 2D size plots of ZnO NPs prepared in the presence of 2 eq. OA for different amount of water.

Table 1. Multivariate analysis of the 2D plots corresponding to the TEM images of the Figure 1 (ZnO NPs prepared in the presence of 2 eq. OA for different amount of water) through Rmixmod program[4]-[6] (the dispersion is given as twice the standard deviation obtained from calculations, and number of cluster was set to 1).

Equivalent of H_2O	Length (nm)	Width (nm)	Correlation
2	36.6 ± 10.8	4.5 ± 1.3	0.25
4	25.8 ± 15.5	5.0 ± 1.3	0.35
8	24.3 ± 12.9	5.3 ± 1.6	0.26
12	18.9 ± 9.7	5.6 ± 1.7	0.05
20	15.0 ± 6.7	5.8 ± 1.7	0.07
40	11.4 ± 9.1	5.7 ± 1.5	0.16
70	12.0 ± 5.5	6.0 ± 1.4	0.18
100	11.0 ± 5.8	6.3 ± 1.6	0.46

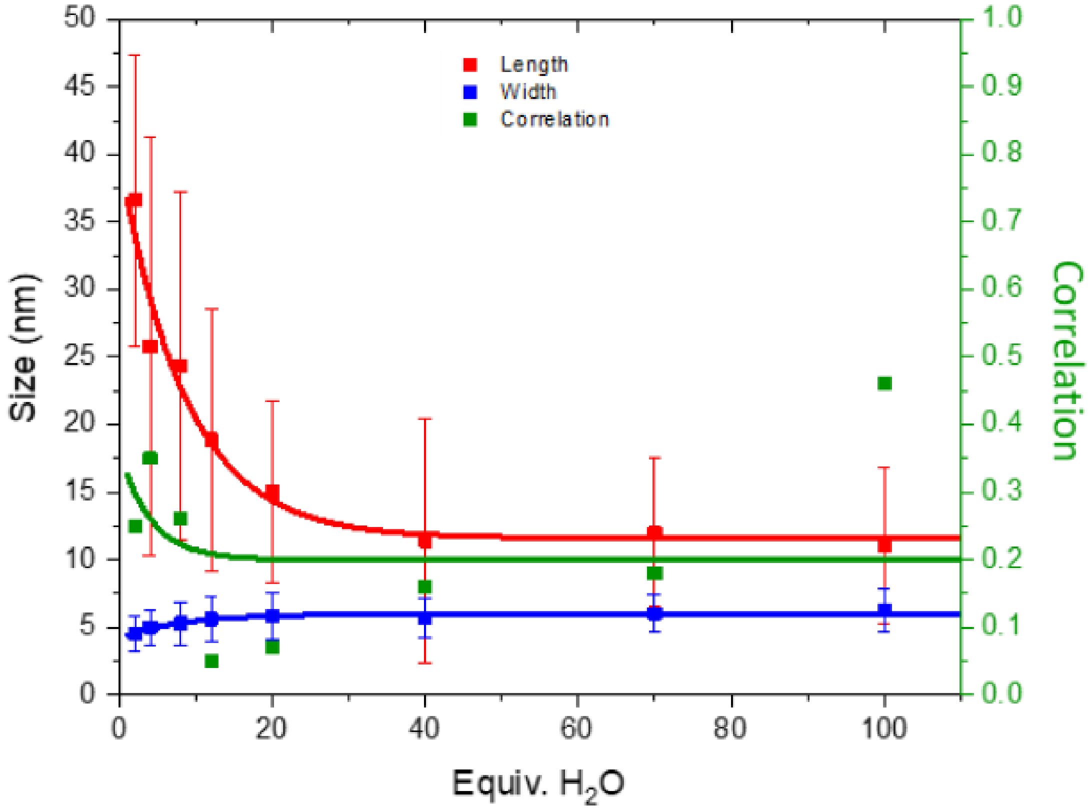

Figure 2: Mean width (red), mean length (blue) and corresponding correlation (green) issued from a multivariate analysis (with a single Gaussian) of data corresponding to

ZnO NPs versus equivalent of water. The lines are just guides for the eyes. See also Figure 1 and Table 1.

Table 2: Multivariate analysis of the 2D plots corresponding to the TEM images of Figure 1 (ZnO NPs prepared in the presence of 2 eq. OA for different amount of water) through a modified Rmixmod program.[7]

Water amount (equivalents)	Number of N1	Number of N2	Population of N1 (%)	Population of N2 (%)
2	2	298	0.7	99.3
4	9	293	3.0	97.0
8	10	291	3.3	96.7
12	45	255	15.0	85.0
20	125	175	41.7	58.3
40	198	102	66.0	34.0
70	248	52	82.7	17.3
100	266	34	88.7	11.3

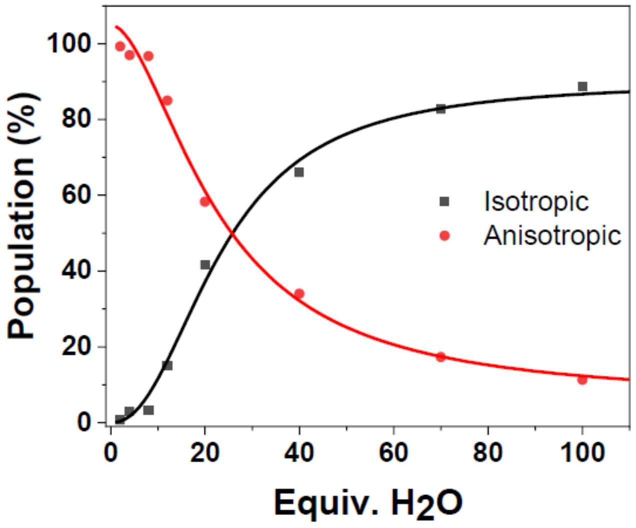

Figure 3. Percent of N1 and N2 depending on amount of water. See also the Figure 1 and Table 1.

Chapitre III

Préparation et Synthèse:

Préparation des colloïdes de $[Zn(Cy)_2]/C_{12}-NH_2$, $[Zn(Cy)_2]/2C_{12}-NH(CH_3)$, $[Zn(Cy)_2]/2\ C_{12}-N(CH_3)_2$, dans du toluène-d^8 pour la mesure RMN à l'état liquide : dans la boîte à gants, en mélangeant 1 équivalent de $[Zn(Cy)_2]$ (57,9 mg, 0,25 mmol) avec 2 équivalents de $C_{12}-NH_2$ (92,68 mg, 0,5 mmol) dans un flacon de 4 mL, on obtient un liquide transparent après une agitation douce de quelques minutes. Pour la mesure RMN à l'état liquide, environ 0,2 mL de ce liquide transparent et 0,5 mL de toluène-d^8

ont été ajoutés dans un tube RMN.

Colloïdes de [Zn(Cy)$_2$]/2C$_{12}$-NH(CH$_3$) ([Zn(Cy)$_2$]: 57,9 mg, 0,25 mmol; C$_{12}$-NH(CH$_3$): 99,69 mg, 0,5 mmol), [Zn(Cy)$_2$] / 2C$_{12}$-N(CH$_3$)$_2$ ([Zn(Cy)$_2$]: 57. 9 mg, 0,25 mmol; C$_{12}$-N(CH$_3$)$_2$: 106,7 mg, 0,5 mmol) dans du toluène-d^8 ont été préparés de la même manière que les colloïdes de [Zn(Cy)$_2$]/C$_{12}$-NH$_2$.

Préparation de ZnO/C$_{12}$-NH(CH$_3$)/air: dans la boîte à gants, C$_{12}$-NH(CH$_3$) (49.85 mg, 0.25 mmol) a été ajouté à [Zn(Cy)$_2$] (57.9 mg, 0.25 mmol) dans une fiole de 4 mL. Après une légère agitation de quelques minutes, un liquide transparent est obtenu. Il a ensuite été transféré hors de la boîte à gants pour subir une hydrolyse au contact de l'air pendant 4 jours.

Préparation de ZnO/2C$_{12}$-NH(CH$_3$)/air: Le procédé est le même que dans le cas de la préparation de ZnO/C$_{12}$-NH(CH$_3$)/air à l'exception de l'équivalent d'amine (99.69 mg, 0.5 mmol).

Préparation de ZnO/10C$_{12}$-NH(CH$_3$)/air: Le procédé est le même que dans le cas de la préparation de ZnO/2C$_{12}$-NH(CH$_3$)/air, à l'exception de l'équivalent d'amine (498,45 mg, 2,5 mmol).

Préparation de ZnO/2C$_{12}$-N(CH$_3$)$_2$/air: Le procédé est le même que dans le cas de la préparation de ZnO/2 C$_{12}$-N(CH$_3$)$_2$/air, à l'exception de l'équivalent d'amine (106,7 mg, 0,5 mmol).

Préparation de ZnO/10C$_{12}$-N(CH$_3$)$_2$/air: Le procédé est le même que dans le cas de la préparation de ZnO/2C$_{12}$-N(CH$_3$)$_2$/air à l'exception de l'équivalent d'amine (706,15 mg, 2,5 mmol).

Table 1. Multivariate analysis of the 2D plots corresponding to the TEM images of the Figure 1 (ZnO NPs versus the nature of the amines) through Rmixmod program[4]-[6] (the dispersion is given as twice the standard deviation obtained from calculations).

Nature of the amine	Morphology	Proportion (%)	Length (nm)	Width (nm)	Correlation
C$_{12}$-NH$_2$	Nanorods	74	16 ± 7	5.0 ± 0.7	0.02
	Isotropic	26	6.6 ± 1.9	6.6 ± 1.9	1.00
C$_{12}$-NH(CH$_3$)	Isotropic	100	7.3 ± 1.1	7.3 ± 1.1	0.58
C$_{12}$-N(CH$_3$)$_2$	Aggregates	100	-	-	-

Résultats et analyses de PXRD:

La phase cristallographique du ZnO obtenu est wurtzite, i. e. hexagonale. Ces résultats ont été obtenus par diffraction des rayons X sur poudre. Les diffractogrammes présentent le même motif dans le domaine de 15° à 90° θ, ce qui correspond à la phase hexagonale de la zincite (groupe d'espace P_{63mc}) quelle que soit l'amine (Voir Figure 1). Lorsque la forme des nanoparticules correspond à des nanorods, les diffractogrammes présentent une largeur à mi-hauteur (full width at half maximum, FWHM) étroite de la ligne de diffraction 002 par rapport aux pics de diffraction 100 et 101. En revanche, les nanoparticules isotropes ne présentent pas d'étroitesse particulière de la ligne de diffraction 002 et des largeurs à mi-hauteur similaires sont observées pour les pics de diffraction 002, 100 et 101. La petite largeur à mi-hauteur de la ligne de diffraction 002 observée pour les nanorods est en accord avec l'existence d'un axe privilégié de croissance - l'axe c de la phase zincite pour les nanorods de ZnO. L'estimation de la taille des cristallites à l'aide de l'équation de Debye-Sherrer donne des valeurs en accord avec l'analyse de la taille par MET (Voir Table 2), en accord avec nos résultats précédemment publiés affirmant que les nano-objets obtenus suite à cette approche organométallique sont bien monocristallins.

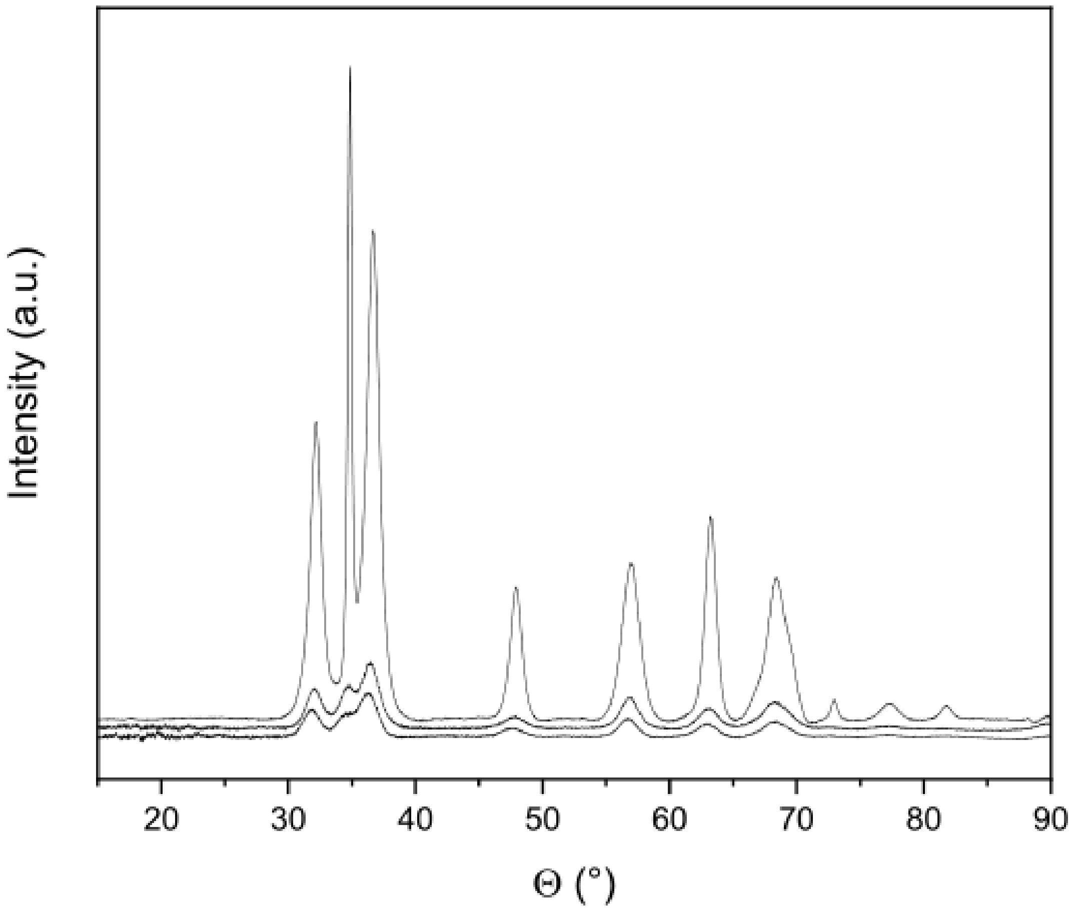

Figure 1: X-ray diffraction pattern recorded at room temperature for ZnO nanoparticles synthesized with C_{12}-NH_2 (top), C_{12}-$NH(CH_3)$ (medium), and C_{12}-$N(CH_3)_2$ (bottom).

Table 2. Estimation of the crystallite size using Debye-Sherrer equation. Full width at half maximum, FWHM, of ZnO nanoparticles synthesized with C_{12}-NH_2, C_{12}-$NH(CH_3)$, and C_{12}-$N(CH_3)_2$ are reported for *100*, *002*, and *101* peaks.

Sample	100 FWHM	002 FWHM	101 FWHM
ZnO@ C_{12}-NH_2	5	40	5
ZnO@C_{12}-$NH(CH_3)$	6	5	5
ZnO@C_{12}-$N(CH_3)_2$	6	6	5

Relevant QTAIM and ELF analysis:

Table 3**.** Relevant QTAIM descriptors (in a.u. except for E_{int} in kcal.mol^{-1}) related to Zn-C and Zn-N bonds in [ZnCy$_2$(C$_6$H$_{13}$NH$_x$Me$_{2-x}$)] complexes (x = 0 - 2). PBE-D3/DGDZVP level of calculation. Bond critical point number. See above for definition and assignment of QTAIM descriptors.

QTAIM molecular graph	BCP	Bond	*V/G*	*-H/ρ*	DI	E_{int}
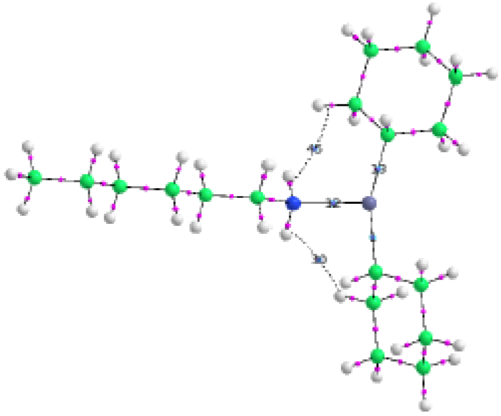	**12**	**Zn-N**	**1.01**	**0.01**	**0.28**	**14.7**
	1	Zn-C	1.49	0.42	0.74	42.0
	13	Zn-C	1.49	0.42	0.75	41.5
	30	H-bond	0.70	-0.22	0.01	0.9
	45	H-bond	0.70	-0.25	0.01	1.3
[ZnCy$_2$(C$_6$H$_{13}$NH$_2$)]						

QTAIM molecular graph	BCP	Bond	*V/G*	*-H/ρ*	DI	E_{int}
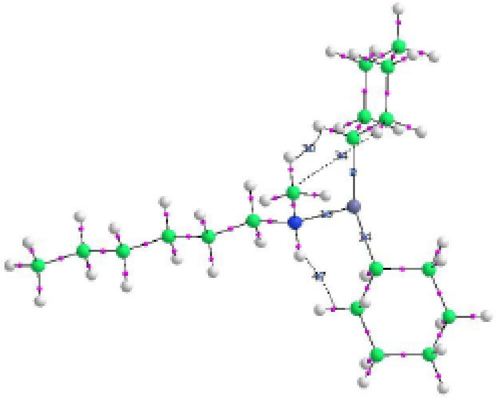	**13**	**Zn-N**	**1.01**	**0.01**	**0.27**	**13.8**
	2	Zn-C	1.49	0.42	0.74	42.1
	14	Zn-C	1.49	0.42	0.74	41.4
	30	H-bond	0.66	-0.25	0.01	0.8
	47	H-bond	0.74	-0.21	0.01	1.5
	34	H-bond	0.63	-0.25	0.01	0.5
[ZnCy$_2$(C$_6$H$_{13}$NHMe)]						

QTAIM molecular graph	BCP	Bond	V/G	$-H/\rho$	DI	E_{int}
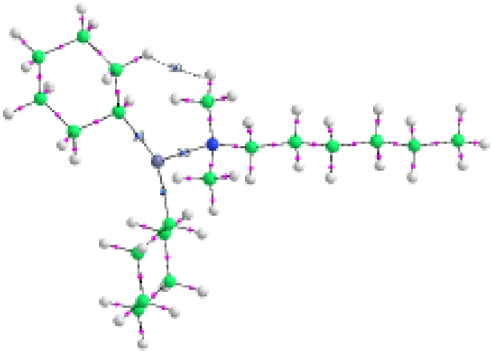	**13**	**Zn-N**	**1.00**	**0.00**	**0.26**	**12.0**
	2	Zn-C	1.48	0.41	0.72	40.9
	11	Zn-C	1.48	0.41	0.75	40.8
	50	H-bond	0.70	-0.22	0.02	1.10
$[ZnCy_2(C_6H_{13}NMe_2)]$						

QTAIM molecular graph	BCP	Bond	V/G	$-H/\rho$	DI	E_{int}
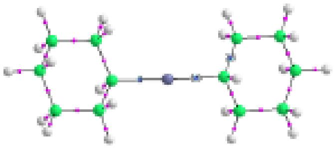	3	Zn-C	1.54	0.44	0.80	43.8
	19	Zn-C	1.54	0.44	0.80	43.8
	28	C-C	4.16	0.79	1.01	73.9
$[ZnCy_2]$						

Table 4. Relevant ELF descriptors of the Zn-C and Zn-N bonds in $[ZnCy_2(C_6H_{13}NH_xMe_{2-x})]$ complexes (x = 0 - 2). Descriptors are averaged over both equivalent Zn-C bonds.

	$ZnCy_2$	$[ZnCy_2(C_6H_{13}NH_2)]$	$[ZnCy_2(C_6H_{13}NHMe)]$	$[ZnCy_2(C_6H_{13}NMe_2)]$
V(N)	-	2.17	2.16	2.18
% Zn[a]	-	0.06 (2.8%)	0.06 (2.8%)	0.05 (2.3%)
cov(V(N),C(Zn))	-	-0.08	-0.07	-0.07
V(Zn,C)	2.16	2.12	2.12	2.12
% Zn[b]	0.69 (32%)	0.59 (28%)	0.59 (28%)	0.56 (26%)
Cov(V(Zn,C),C(Zn))	-0.46	-0.36	-0.36	-0.37

a: Atomic contribution of Zn to V(N). b: Atomic contribution of Zn to V(Zn, C)

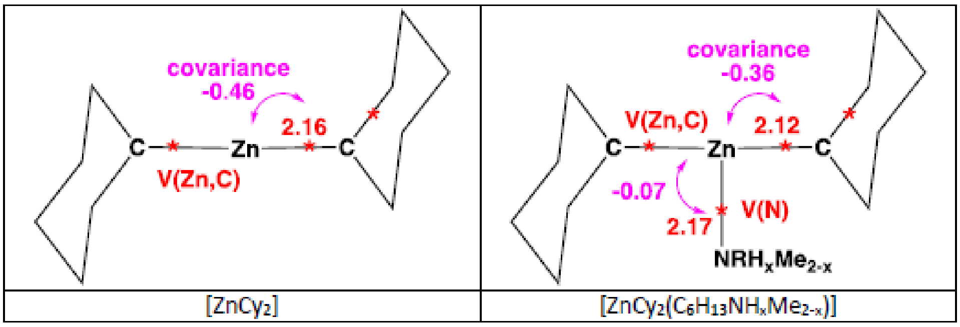

$[ZnCy_2]$ | $[ZnCy_2(C_6H_{13}NH_xMe_{2-x})]$

Figure 2. ELF valence attractors and covariances calculated at the PBE-D3/DGDZVP level.

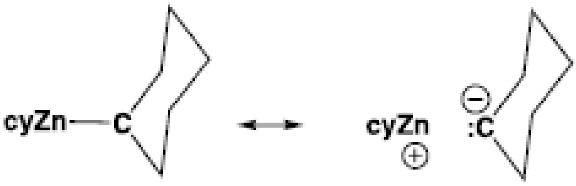

Figure 3. Most representative mesomeric forms of $[Zn(Cy)_2]$ from reference 3.

Table 5. Largest values of Fukui indices $f_{ELF}{}^-$ and $f_{ELF}{}^+$ condensed on ELF valence basins of $[ZnCy_2(C_6H_{13}NH_xMe_{2-x})]$ complexes (x = 0 - 2). PBE-D3/DGDZVP level of calculation.

f_{ELF}^-	$ZnCy_2$	$[ZnCy_2(C_6H_{13}NH_2)]$	$[ZnCy_2(C_6H_{13}NHMe)]$	$[ZnCy_2(C_6H_{13}NMe_2)]$
V(Zn,C)	0.21	0.23	0.23	0.23
V(Zn,C)	0.21	0.21	0.21	0.21
f_{ELF}^+	$ZnCy_2$	$[ZnCy_2(C_6H_{13}NH_2)]$	$[ZnCy_2(C_6H_{13}NHMe)]$	$[ZnCy_2(C_6H_{13}NMe_2)]$
V(Zn,C)	0.22	0.08	0.13	0.17
V(Zn,C)	0.22	0.08	0.13	0.11

Table 6. Largest values of Fukui indices $f_{QTAIM}{}^-$ and $f_{QTAIM}{}^+$ condensed on QTAIM basins of $[ZnCy_2(C_6H_{13}NH_xMe_{2-x})]$ complexes (x = 0 - 2). PBE-D3/DGDZVP level of calculation.

f_{QTAIM}^-	$ZnCy_2$	$[ZnCy_2(C_6H_{13}NH_2)]$	$[ZnCy_2(C_6H_{13}NHMe)]$	$[ZnCy_2(C_6H_{13}NMe_2)]$
C^a	0.26	0.28	0.29	0.17
C^a	0.26	0.26	0.25	0.11
f_{QTAIM}^+	$ZnCy_2$	$[ZnCy_2(C_6H_{13}NH_2)]$	$[ZnCy_2(C_6H_{13}NHMe)]$	$[ZnCy_2(C_6H_{13}NMe_2)]$
Zn	0.33	0.24	0.14	0.25
N	-	-	0.14	-

a: QTAIM atomic basin of the carbon atom bound to Zn

Chapitre IV

Préparation de l'échantillon pour les mesures en RMN à l'état solide:
Dans une boîte à gants, 1 équivalent de [Zn(Cy)$_2$] (115,85 mg, 0,5 mmol) a été ajouté à 2 équivalents de DDA (185,35 mg, 1,0 mmol) dans un vial en verre de 4 mL. Une solution homogène claire a été obtenue après une légère agitation. Ensuite, un rotor de zircone de diamètre interne de 4 mm avec un insert en téflon et une vis ont été utilisés pour sceller le mélange transparent afin d’effectuer l'étude cinétique par caractérisation en RMN de l'état solide. Pour les autres amines, les préparations et les mesures par RMN à l'état solide sont les mêmes que dans le cas du DDA.

Préparation des échantillons pour l'étude des propriétés rhéologiques:
Dans une boîte à gants, 1 équivalent de [Zn(Cy)$_2$] (347.55 mg, 1.5 mmol) a été ajouté à 2 équivalents d'octylamine (387.72 mg, 3.0 mmol) dans un vial en verre de 4 mL. Une solution homogène claire a été obtenue après une légère agitation. Ce liquide transparent et clair est transféré dans une seringue de 1.0 ml et maintenu au repos dans la boîte à gants pendant 4 heures, puis il est injecté dans l’entrefer du rhéomètre pour commencer la mesure des propriétés rhéologiques. Pour l'hexylamine, les préparations et les mesures sont les mêmes que dans le cas du octylamine.

References

[1] Z. Zhao, Z. Zheng, C. Roux, C. Delmas, J. D. Marty, M. L. Kahn and C. Mingotaud, “Importance of the Correlation between Width and Length in the Shape Analysis of Nanorods: Use of a 2D Size Plot To Probe Such a Correlation”, *Chem. Eur. J.*, **2016**, *22*, 12424-12429.

[2] P. Thordarson, “Determining association constants from titration experiments in supramolecular chemistry”, *Chem. Soc. Rev.*, **2011**, *40*, 1305–1323.

[3] Z. Zhao, Y. Coppel, J. Fitremann, P. Fau, C. Roux, C. Lepetit, P. Lecante, J.-D. Marty, C. Mingotaud, M. L. Kahn, “Mixing Time between Organometallic Precursor and Ligand: A Key Parameter Controlling ZnO Nanoparticle Size and Shape and Processable Hybrid Materials”, *Chem. Mater.*, **2018**, *30*, 8959-8967.

[4] C. Biernacki, G. Celeux, G. Govaert, F. Langrognet, “MIXMOD: a software for model-based classification with continuous and categorical data”, **2008**.

[5] R. Lebret, S. Iovleff, F. Langrognet, C. Biernacki, G. Celeux, G. Govaert, “Rmixmod: The R package of the model-based unsupervised, supervised, and semi-supervised classification Mixmod library”, Journal of Statistical Software, **2015**, *67*, 1-29.

[6] R. Lebret, S. Iovleff, F. Langrognet, M. R. Lebret, L. Rcpp, “Package ‘Rmixmod’ ”, **2015**.

[7] Modified mixmod software:

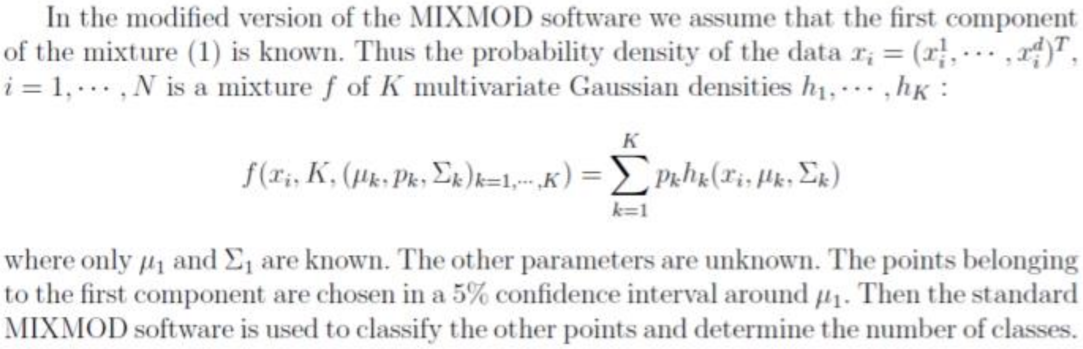

In the modified version of the MIXMOD software we assume that the first component of the mixture (1) is known. Thus the probability density of the data $x_i = (x_i^1, \cdots, x_i^d)^T$, $i = 1, \cdots, N$ is a mixture f of K multivariate Gaussian densities $h_1, \cdots, h_K$:

$$f(x_i, K, (\mu_k, p_k, \Sigma_k)_{k=1,\cdots,K}) = \sum_{k=1}^{K} p_k h_k(x_i, \mu_k, \Sigma_k)$$

where only μ_1 and Σ_1 are known. The other parameters are unknown. The points belonging to the first component are chosen in a 5% confidence interval around μ_1. Then the standard MIXMOD software is used to classify the other points and determine the number of classes.

[8] M. L. Kahn, M. Monge, V. Colliere, F. Senocq, A. Maisonnat, B. Chaudret, “Size- and shape‐control of crystalline zinc oxide nanoparticles: a new organometallic synthetic method”, *Adv. Funct. Mater.,* **2005**, *15*, 458-468.

Résumé de thèse

Aujourd'hui, les nanosciences sont définies comme l'étude des structures (moléculaires) et dispositifs dont au moins une des dimensions caractéristiques se situe 1 - 100 nm. Ces nanomatériaux agissant comme de pont entre les matériaux massifs et les structures atomiques et démontrent que de nombreuses modifications dans les propriétés physiques, chimiques ou biologiques en raison de la taille réduite. Les nanomatériaux composés d'oxydes métalliques sont un tel type de matériaux intéressants. Leurs caractéristiques sont très intéressantes pour le développement d'applications électroniques, optiques, de capteurs et autres.

Pour certains des oxydes métalliques, un manque d'oxygène crée des vacances agissant comme donneur d'électrons et induisant des propriétés de semi-conducteurs de type n. ZnO est un exemple typique. Il est caractérisé par une large bande interdite d'environ 3.4 eV, d'une grande exciton l'énergie de 60 meV, d'une grande mobilité électronique et d'une luminescence dans le visible et le proche ultraviolet. Ces caractéristiques électroniques en font un bon candidat pour le développement de sources d'émission lumineuse et de détecteurs. Il a été ainsi montré que ZnO pouvait, selon les conditions de préparations, émettre dans l'ultraviolet, le violet, le vert, le jaune et même le rouge. Ces propriétés optiques de ZnO dependent fortement de la morphologie des matériaux.

Dans le travail précédent, une méthode mature de synthèse des nanomatériaux ZnO a été développée - la méthode organométallique. Les nano ZnO bien définis avec différentes tailles, formes et morphologies (isotrope, anisotrope) peuvent être obtenus en changeant différents paramètres (milieu de réaction, types de ligands ou de surfactants, température, temps d'mélange, etc.). Cependant, lorsque des amines primaires sont utilisées comme ligands, le mécanisme de la croissance anisotrope n'est toujours pas clair. Les influences des amines secondaires et tertiaires sur nano ZnO obtenus ne sont pas encore dévoilées. Ainsi, la thèse s'attache tout d'abord à étudier les deux points ci-dessus.

Premièrement, nous utilisons la méthode d'analyse de tracé 2D et d'analyse statistique pour extraire les informations sur la taille des particules à partir des images TEM. Les données traitées suggèrent que le mécanisme de croissance anisotrope est le processus d'attachement orienté, et finalement entravé par un processus de gélification induit par l'interaction du Zn précurseur avec les aminés. Deuxièmement, nous adoptons une amine de même longueur de chaîne mais de structure différente comme tensioactif (amine primaire, secondaire et tertiaire) pour synthétiser les NCs de ZnO. Les analyses RMN et DFT ont démontré que la différence de morphologie entre les NCs de ZnO viens d'une forte différence dans leur dynamique à la surface des NCs en croissance. L'interaction des liaisons H multiples à la surface du ZnO pour les amines primaires, conduit à une mobilité réduite de ces amines par rapport aux amines secondaires, qui restent mobiles à la surface des NCs dans toutes les dimensions de l'espace.

Ce thèse aussi comprend le sujet du gel qui est trouvé pendant le synthèse du ZnO. Il a été démontré que la gélification était associée à la formation d'oligomères.

Cependant, pour comprendre la force motrice de la gélification et étudier la révolution des propriétés rhéologiques avec le temps, d'autres amines primaires avec une longueur de chaîne différente sont utilisées. Les résultats de RMN montrent que la force intermoléculaire (force de Van der Waals, réticulation) contribue à la vitesse de gélification et explique les différents temps de début de gélification. Plus la chaîne est longue, plus la gélification est rapide. La première est déterminée par la force de VdW, et la seconde est déterminée par la réticulation entre les oligomères formés. Les résultats de la mesure rhéologique ont montré que le gel était composé d'une phase organique tridimensionnelle.

Résumé de Chapitre I

Dans ce chapitre, introduisant les éléments nécessaires à la compréhension des travaux de recherche décrits dans les chapitres suivant, nous commençons par présenter brièvement le domaine des nanosciences, puis les avantages exceptionnels des nanomatériaux semi-conducteurs à base d'oxyde métallique et enfin nous présentons les propriétés du ZnO, matériaux sur lequel porte toutes les études décrites dans ce manuscrit. Après une présentation générale des deux structures cristallographiques de ZnO et les conditions spécifiques à l'obtention de l'une ou l'autre phase, nous présentons les propriétés physiques de ZnO avec en particulier ses propriétés optiques et les différentes façons de les modifier, par exemple, par dopage.

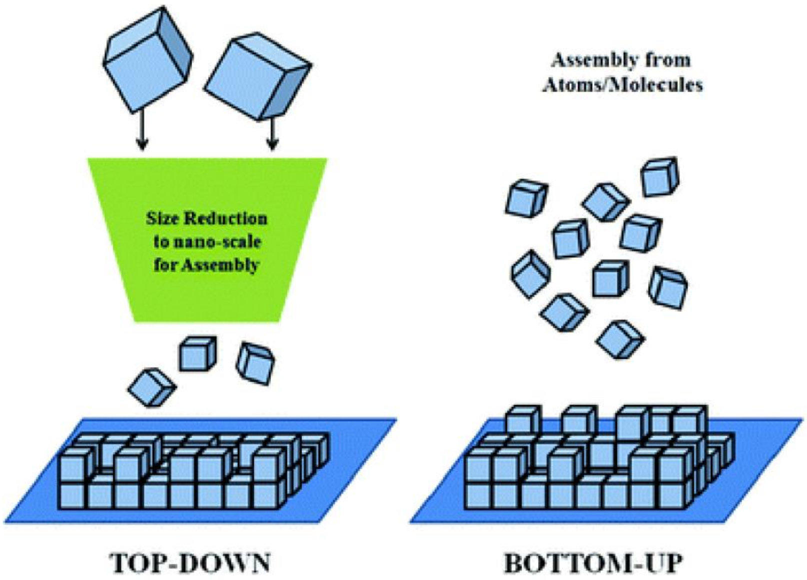

Figure 2.illustration des approche top-down et bottom-up.

En ce qui concerne la préparation des nanomatériaux, nous présentons quelques méthodes de synthèse les plus couramment reportées dans la bibliographie. Qu'il s'agisse d'approches bottom up ou top down. Nous décrivons ainsi différentes approches physique ou chimiques en présentant les avantages et inconvénients pour chacune d'entre elles. Nous nous concentrons finalement sur la méthode de synthèse qu'utilise notre groupe, à savoir la méthode organométallique. Cette méthode a été utilisée tout au long du travail de cette thèse. Elle consiste à tirer avantage du caractère exothermique de la réaction d'hydrolyse de précurseurs organométalliques pour donner à température ambiante et pression atmosphérique des nanoparticules d'oxydes métalliques cristallins de taille, forme et état de surface contrôlés. Les travaux antérieurs liés au ZnO sur lesquels se fondent ces travaux de thèse sont présentés. Ils découlent de la trajectoire scientifique que les équipes NOS et IDEas suivent depuis plus d'une quinzaine d'années.

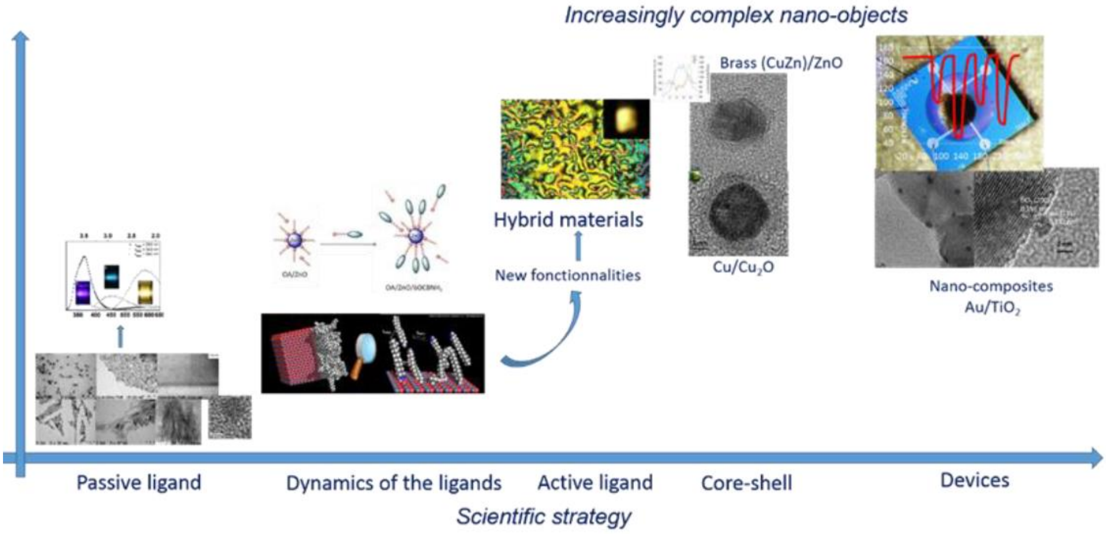

Figure 3 : stratégie scientifique des équipes NOS et IDEaS.

Un point spécifique portant sur la spectroscopie RMN est décrit dans ce chapitre introductif car cette technique est très utile pour la compréhension de l'effet des ligands introduits dans le milieu réactionnel et leur rôle dans le contrôle de la taille et de la forme des nanoparticules et aussi leur état de surface.

Nous enchainons ensuite avec une description des phénomènes de gélification. Quelques généralités sont présentées afin de permettre au lecteur de bien comprendre une partie des travaux décrits dans ce manuscrit. Les propriétés rhéologiques des gels sont également présentées car elles sont un élément important de nos travaux.

Tous ces éléments permettent de définir les objectifs de cette thèse.

Résumé de Chapitre II

Les mécanismes qui sous-tendent les voies de synthèse ou les propriétés des nanomatériaux présentent un intérêt particulier. De nombreux procédés chimiques ont été développés pour contrôler la taille, la polydispersité, la forme, la surface, la composition chimique volumique des nanoparticules (NPs), etc. Les nanoparticules (NPs) semi-conductrices métalliques, II-VI ou III-V sont aujourd'hui synthétisées avec une forme isotrope simple ou une structure cœur-coquille plus élaborée. Les cubes, les étoiles, les architectures bipyramidales, les nanofils, etc. sont également largement décrits. En général, la variation de la taille et de la forme dépend des conditions chimiques expérimentales et des mécanismes proposés. Cependant, un certain nombre de défis subsistent, notamment la mise en évidence et la compréhension de la relation entre les paramètres expérimentaux de la synthèse et la forme des NP, cette dernière déterminant les propriétés des NP.

La complexité inhérente à de tels systèmes exige d'avoir accès à des techniques analytiques efficaces pour les étudier et comprendre la corrélation (le cas échéant) entre les différents paramètres impliqués. Ce Graal pourrait être atteint grâce à l'analyse multivariée ou à l'apprentissage automatique, mais l'une des contraintes est le manque de données, qui est particulièrement problématique : les ensembles de données peuvent être soit denses (c'est-à-dire qu'ils couvrent une petite fraction de l'espace de configuration), soit épars (c'est-à-dire qu'ils couvrent une grande fraction de l'espace de configuration, mais avec de nombreuses données manquantes).

L'objectif de ce chapitre est de démontrer comment des outils analytiques simples basés sur l'analyse statistique peuvent nous aider à déchiffrer la croissance anisotrope des NPs et à mieux comprendre et contrôler les paramètres régissant cette croissance anisotrope. Les NPs de ZnO ont été prises comme premier système modèle et ont été préparées en suivant l’approche organométallique mise au point dans l’équipe. Comme nous l’avons décrit dans le chapitre introductif, cette approche consiste en l'hydrolyse du précurseur de zinc dicyclohexyle, [$ZnCy_2$]. En une seule étape et dans des conditions douces (c'est-à-dire à température ambiante et à pression atmosphérique), des nanoparticules de ZnO cristallines bien définies peuvent être synthétisées. Dans ce processus, le contrôle de la morphologie (c'est-à-dire soit des nanoparticules isotropes, soit des nanobatonnets) est réalisé en faisant varier les conditions expérimentales : les nanoparticules isotropes sont obtenues en présence de ligands alkylamines dans un solvant organique, tandis que les nanorods sont obtenus dans les mêmes conditions expérimentales mais en l'absence de solvant. Jusqu'à présent, les résultats expérimentaux suggèrent le rôle critique de différents paramètres tels que la composition du mélange réactionnel, la quantité d'eau, les paramètres cinétiques de la réaction, la température...

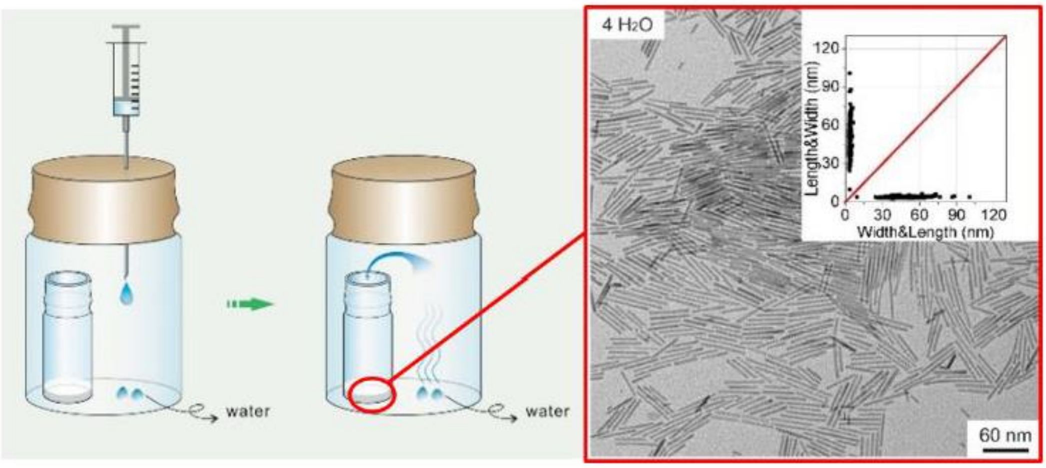

Afin d'obtenir des informations sur les paramètres importants pour la croissance de tels nanobatonnets et de mieux comprendre les processus de croissance, nous avons étudié la cinétique de formation des NPs de ZnO anisotropes dans différentes conditions en utilisant deux outils analytiques différents permettant l'analyse des images TEM : les diagrammes de taille 2D et l'analyse statistique multivariée. Le premier, le 2D size plot, permet d'extraire des informations sur la corrélation entre les largeurs et les longueurs des objets anisotropes. Pour cela, chaque particule est caractérisée par deux tailles, notées D1 et D2, mesurées sur des axes perpendiculaires. Ces deux tailles correspondent généralement à la longueur et à la largeur des nano-objets. Pour chaque particule et sur un même graphique, on trace D1 en fonction de D2 et également D2 en fonction de D1. Les tracés 2D proposés permettent de visualiser qualitativement une telle corrélation. Néanmoins, l'analyse quantitative de ces données pourrait être entravée par la présence de différentes sous-populations qui pourraient nécessiter des procédures fastidieuses pour les séparer, surtout lorsque ces populations se chevauchent. Afin de les identifier numériquement et d'obtenir leurs propres paramètres statistiques tels que la longueur et la largeur moyennes, les écarts types correspondants et la corrélation entre la longueur et la largeur, une analyse multivariée complémentaire doit être effectuée. Lorsqu'un nombre limité de NPs peut être compté, une telle approche peut également conduire à une meilleure précision dans l'analyse statistique en aidant à écarter les sous-populations mineures qui ne sont pas représentatives des échantillons.

Dans le travail décrit dans ce chapitre, nous démontrons comment des outils analytiques simples basés sur l'analyse statistique peuvent nous aider à décrypter la croissance anisotrope des NPs et à mieux comprendre et contrôler les paramètres régissant cette croissance anisotrope. Une comparaison fine du protocole de synthèse du rôle du taux d'hydrolyse, du temps de mélange avant hydrolyse, de la longueur de la chaîne aliphatique du ligand et de la quantité d'eau a permis de mettre en évidence l'importance relative de ces paramètres expérimentaux sur la croissance anisotrope des NPs de ZnO. Toutes les données suggèrent que le mécanisme de croissance s'est produit par un processus d'attachement orienté qui est finalement entravé par le processus de gélification induit par l'interaction du précurseur de zinc ou des NPs de ZnO avec les ligands aminés. Ces résultats mettent en lumière l'importance relative des paramètres expérimentaux qui régissent la croissance des nano-objets et qui, en tant que tels, sont essentiels à identifier, étudier et contrôler pour faire progresser la conception des nanosciences.

Résumé de Chapter III

En plus de la taille nanométrique, la maîtrise de la morphologie des nano-objets est essentielle puisque leurs propriétés peuvent être drastiquement affectées à la fois par leur forme, leur cœur et leur structure de surface. L'utilisation de tensioactifs est courante pour les synthèses réalisées en solution. Même si leur rôle tout au long de la synthèse est supposé être globalement connu, les voies détaillées et les mécanismes précis contrôlant la morphologie des nanoparticules ne sont pas toujours bien compris et pleinement expliqués. Cette question d'actualité mérite donc une attention particulière pour améliorer les procédures de synthèse actuelles.

Au cours de la synthèse de nano-objets en solution, le tensioactif est généralement supposé jouer différents rôles, et peut principalement agir comme ligand pour les espèces moléculaires présentes en solution. Le précurseur métallique peut ainsi être modifié après son introduction dans le milieu réactionnel avant le processus de nucléation. Le tensioactif est également considéré comme un agent bloquant (ou agent stabilisateur de surface) pendant le processus de croissance des nanocristaux (NC). Dans ce dernier cas, les interactions existantes entre le groupe fonctionnel du tensioactif et la surface de l'objet en croissance sont souvent évoquées pour expliquer la taille, la forme et la structure cœur/surface finales obtenues du NC. Comme la plupart des tensioactifs peuvent agir comme des ligands pour les espèces moléculaires présentes dans le milieu réactionnel, mais aussi se coordonner aux surfaces des NC en croissance, cela complique la compréhension fine de leur rôle dans le système réel. Il est clair que pour une meilleure maîtrise de la croissance et de la structure des nano-objets, toutes les interactions avec les tensioactifs doivent être prises en compte tout au long du processus de formation des NC. Cependant, discerner à chaque étape du processus de formation des NC ce qui est important pour leur morphologie et leur structure et ce qui ne l'est pas, reste délicat, surtout en ce qui concerne les aspects dynamiques.

Dans ce contexte, l'utilisation d'amines à longues chaînes grasses comme surfactants, comme l'archétype de l'oléylamine, est très populaire pour obtenir un bon contrôle de la morphologie des NC. Le point d'ébullition élevé de l'oléylamine, supérieur à 360 °C, a permis de l'utiliser dans des procédés de réduction thermolytique, que ce soit dans une approche "heat up", ou par la technique dite "hot-injection ". L'hexadécylamine, la dodécylamine et l'octylamine sont également largement utilisées dans des conditions plus douces pour la formation de NC métalliques, de semi-conducteurs II-VI ou III-V. Les amines primaires semblent être efficaces pour contrôler la morphologie des NC mais les raisons de ce phénomène ne sont pas claires. Classiquement, l'influence de la longueur de la chaîne aliphatique de l'amine sur la morphologie des NC est considérée, mais le rôle de la structure générale de l'amine et en particulier le nombre de substituants autour de l'atome d'azote - c'est-à-dire amine primaire vs secondaire ou tertiaire - n'a pas été étudié en détail.

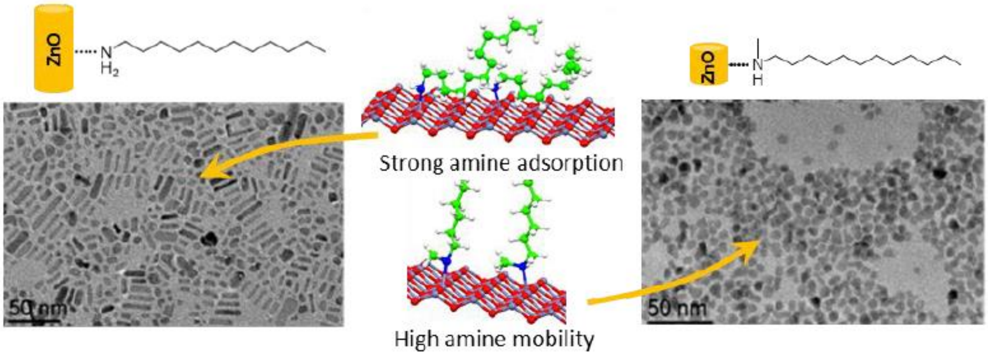

Dans ce chapitre, nous décrivons nos progrès dans la compréhension et le contrôle à l'échelle moléculaire de la construction de nano-objets fonctionnels. Le présent travail vise à élucider la complexité inhérente à la synthèse organométallique douce en solution de NC de ZnO. Nous nous sommes concentrés sur certains des tensioactifs les plus utilisés pour la croissance des nanoparticules, les alkylamines grasses. En gardant la même longueur de chaîne aliphatique et en variant la structure de l'amine (primaire, secondaire ou tertiaire), les analyses complémentaires RMN et DFT ont permis d'étudier l'interaction de ces tensioactifs avec le précurseur métallique des NC de ZnO tout au long du processus de synthèse. Quelle que soit la structure de l'amine, un adduit 1:1 est initialement formé. Cependant, alors que sa constante d'association est cohérente pour les amines primaires et secondaires apparentées, elle est inférieure d'un ordre de grandeur pour l'amine tertiaire correspondante. La différence entre les tensioactifs à base d'amine primaire et secondaire provient de la propension de l'amine primaire à former des oligomères zinc-amido, une réaction qui est entravée dans le cas de l'amine secondaire en raison d'un encombrement stérique plus important.

Cependant, la vitesse de réaction de cette oligomérisation s'est avérée beaucoup plus lente que la réaction d'hydrolyse générant les NC, et a une influence négligeable sur la structure des NC. Nous avons donc démontré que la différence de morphologie entre les NC de ZnO observée en fonction de la structure des amines provient d'une forte différence dans leur dynamique à la surface des NC en croissance. L'interaction des liaisons H multiples à la surface du ZnO pour les amines primaires, identifiée par ^{13}C MAS NMR, conduit à une mobilité réduite de ces amines par rapport aux amines secondaires, qui restent mobiles à la surface des NC dans toutes les dimensions de l'espace.

Notre approche pourrait clairement être étendue à un grand nombre de nanoparticules métalliques et semi-conductrices stabilisées en solution par des surfactants tels que des thiols, des acides carboxyliques, des phosphines, des carbènes, etc. Cela permettrait d'acquérir des connaissances fondamentales en vue d'une vision rationalisée de la synthèse douce et contrôlée des NC en solution. Plus important encore, nous avons montré ici que l'utilisation efficace et très répandue des amines primaires dans la synthèse de nanoparticules *via* des protocoles en solution est attribuable à des liaisons hydrogène, interactions faibles ayant une forte influence sur la surface de la nanoparticule en croissance et sur la morphologie et la structure finales du matériau hybride.

Résumé de Chapter IV

L'organisation des nano-objets à une plus grande échelle ou même la mise en forme du matériau final au niveau macroscopique est nécessaire pour obtenir des dispositifs fonctionnels. Ce défi a stimulé le développement de plusieurs méthodes de mise en forme conduisant à des films minces, des matériaux poreux ou organisés en 3D, qui sont souvent plus faciles à obtenir lorsqu'un gel aux propriétés rhéologiques contrôlées est utilisé. Ceci explique pourquoi la méthode "sol-gel" est si populaire. Cette méthode est basée sur l'utilisation de solutions aqueuses d'alcoxydes métalliques ou de sels métalliques dans lesquelles un processus d'hydrolyse et de condensation contrôlé est déclenché, conduisant à l'oxyde métallique. Pour certains métaux, l'équilibre d'hydrolyse n'est pas favorable. Dans ce cas, la méthode de Pechini (ou méthode des complexes polymérisables) a été développée. Elle est basée sur la polyesterification des complexes métal-citrate qui conduit à la formation d'un réseau covalent étendu. Les méthodes "sol-gel" et Pechini sont toutefois limitées aux systèmes aqueux. Des voies sol-gel non aqueuses ont ensuite été développées en utilisant des sels métalliques tels que des halogénures métalliques, des alcoxydes métalliques, des acétates métalliques ou des acétylacétonates métalliques et en procédant sans ajout externe d'eau. Ces réactions sont, en particulier pour les alcoxydes de métaux de transition, très rapides et difficiles à contrôler, donnant des gels amorphes. En conséquence, les aérogels ou xérogels finaux doivent être traités thermiquement pour induire la cristallisation de la structure d'oxyde métallique. En outre, le nombre de précurseurs moléculaires appropriés est encore limité. Heureusement, nous avons récemment décrit l'utilisation de précurseurs organométalliques tels que des alkyl zinc, en présence de ligands tels que les alkyl amines, comme une alternative permettant d’obtenir des gels. Cette voie organométallique a été appliquée à plusieurs éléments métalliques. A chaque fois, le mélange d'amines grasses avec des composés organométalliques induit la formation de structures oligomériques entre les centres métalliques. Une gélification du mélange se produit alors, et l'on est capable de transformer ce gel en fibres, en motifs et en pièces moulées. Ces résultats ont été obtenus en utilisant la dodécylamine (DDA). Pour aller plus loin dans cette approche, l'influence de la longueur de la chaine alkyle de l'amine, un paramètre bien connu et important pour les processus chimiques et de gélification, doit être étudiée pour obtenir une mise en forme facile.

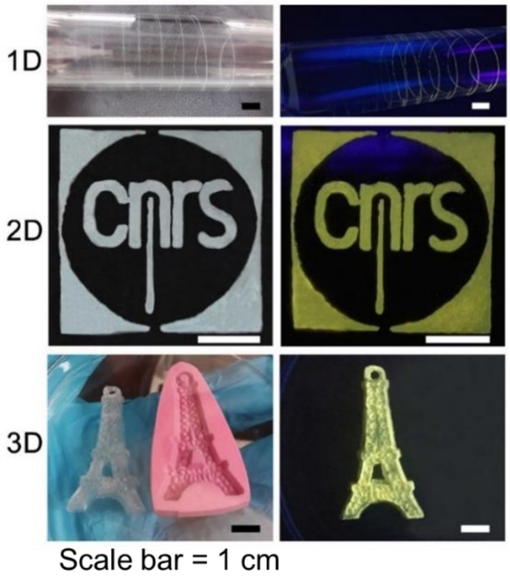

Dans ce chapitre, nous décrivons comment nous avons pu, grâce au couplage entre des mesures de rhéologie macroscopique et des mesures de RMN moléculaire, montrer que le mécanisme de gélification du précurseur organométallique [$ZnCy_2$] et d'une alkylamine primaire provenait d'abord de la rigidification des chaînes aliphatiques de l'amine, qui prime sur l'oligomérisation du squelette inorganique formé par la réaction acide-base, donnant lieu à des liaisons de coordination de type Zn-amido. Ce résultat met en évidence que les propriétés rhéologiques des gels organométalliques, précurseurs de la mise en forme de nanomatériaux d'oxydes métalliques, peuvent être contrôlées par la longueur de la chaîne aliphatique de l'amine. Plus la chaîne aliphatique est longue, plus la gélification est rapide. Il s'agit d'un moyen simple de régler les propriétés rhéologiques de ces systèmes prometteurs.

Perspectives

Les perspectives de ce travail de thèse peuvent être étendues à l'application des outils d'analyse (2D size plot et traitement statistique) dans le traitement des résultats expérimentaux qui sont obtenus lors de la synthèse de nano-objets, de la chimie des précurseurs, des gels, des matériaux hybrides, de la mise en forme des oxydes métalliques et de leurs propriétés de détection.

Il est clair qu'une croissance contrôlée devrait permettre de contrôler leur taille, leur distribution de taille, leur forme, leur structure cristalline, la distribution des défauts et même la structure de surface (terminaison atomique, polarisation de surface). Par conséquent, une compréhension approfondie du mécanisme de croissance est le point clé. Dans nos cas, les stratégies de diagramme de taille 2D et d'analyse statistique que nous présentons révèlent la fixation orientée du mécanisme de croissance anisotrope des nano-objets. D'une manière générale, cette approche méthodologique peut être utilisée pour tout type de système nanoparticulaire.

En ce qui concerne la chimie des précurseurs, l'étude de l'interaction des tensioactifs avec le précurseur métallique des NCs de ZnO tout au long du processus de synthèse et les interactions multiples de liaison H formées à la surface du ZnO montrent l'importance du choix des complexes organométalliques dans le contrôle de la morphologie finale des nano-objets. Cette approche pourrait également être étendue à un grand nombre de nanoparticules métalliques et semi-conductrices stabilisées en solution par des surfactants tels que des thiols, des acides carboxyliques, des phosphines, des carbènes, etc. Cela permettrait d'acquérir des connaissances fondamentales en vue d'une vision rationalisée de la synthèse douce et contrôlée des NCs en solution.

Les recherches sur la force motrice pour former des gels et leurs propriétés rhéologiques nous inspirent l'idée de changer les types de précurseurs métalliques ou la force motrice pour modifier leurs propriétés rhéologiques. Cela pourrait élargir le champ d'application de la mise en forme des matériaux et obtenir des matériaux d'oxyde métallique à porosité contrôlée. En outre, l'exploration d'oxydes complexes impliquant deux ou plusieurs types de cations est possible pour améliorer leur multifonctionnalité.